รหัสโครงการ SUT7-706-47-36-07

รายงานการวิจัย

การปรับปรุงเครื่องตกผลึกในระดับอุตสาหกรรม โดยใช้การจำลอง CFD

(Improvements to Industrial Crystallization Units through CFD Modeling)

ได้รับทุนอุดหนุนการวิจัยจาก

มหาวิทยาลัยเทคโนโลยีสุรนารี

ผลงานวิจัยเป็นความรับผิดชอบของหัวหน้าโครงการวิจัยแต่เพียงผู้เดียว

รหัสโครงการ SUT7-706-47-36-07

รายงานการวิจัย

การปรับปรุงเครื่องตกผลึกในระดับอุตสาหกรรม โดยใช้การจำลอง CFD

(Improvements to Industrial Crystallization Units through CFD Modeling)

คณะผู้วิจัย

หัวหน้าโครงการ

รองศาสตราจารย์ ดร.เอเดรียน ฟลัด

สาขาวิชาวิศวกรรมเคมี

สำนักวิชาวิศวกรรมศาสตร์

มหาวิทยาลัยเทคโนโลยีสุรนารี

ผู้ร่วมวิจัย

นายวิรพงษ์ วันทา

ได้รับทุนอุดหนุนการวิจัยจากมหาวิทยาลัยเทคโนโลยีสุรนารี ปีงบประมาณ พ.ศ. 2547

ผลงานวิจัยเป็นความรับผิดชอบของหัวหน้าโครงการวิจัยแต่เพียงผู้เดียว

กุมภาพันธ์ 2553

Acknowledgements

The research on the DTB crystallizer which has been presented in this report is based on the research of a student funded by this grant, Mr. Wirapong Wantha. Parts of the theory section of this work have been taken or altered from a section written by Mr. Wantha, and published in his M.E. Thesis.

บทคัดย่อ

การตกผลึกจัดเป็นกระบวนการที่มีความสำคัญมากในอุตสาหกรรมการผลิตสารเคมี พบว่าร้อยละ 80 ของการผลิตสารเคมีต้องผ่านขั้นตอนการตกผลึกอย่างน้อย 1 ครั้ง อย่างไรก็ตามความรู้และความเข้าใจในเชิงทฤษฎีของการตกผลึกในระดับอุตสาหกรรมยังมีน้อย และเครื่องตกผลึกเป็นเครื่องมือที่ออกแบบยากที่สุด

งานวิจัยนี้ได้ทำการจำลองตัวเลขและวิเคราะห์การไหลของของเหลวในระบบการตกผลึกในอุตสาหกรรม 2 ประเภท เพื่อที่จะแสดงให้เห็นว่าสามารถใช้เป็นเครื่องมือในการปรับปรุง ออกแบบและหาสภาวะการทำงานที่เหมาะสมของเครื่องตกผลึกได้ โดยหาความสัมพันธ์ระหว่างอัตราการไหลของของเหลว การถ่ายเทความร้อนและสภาวะต่างๆ ในการตกผลึก แบบจำลองอันแรกคือ เครื่องตกผลึกแบบ DTB (Draft tube baffle) ซึ่งเป็นเครื่องตกผลึกแบบต่อเนื่องที่ใช้กันอย่างแพร่หลายในอุตสาหกรรมขนาดใหญ่ ในการตกผลึกสารเคมีอนินทรีย์ ในระบบ DTB นั้น ใช้การระเหยของน้ำในการทำให้สารละลายมีความอิ่มตัวยิ่งยวด เพื่อให้เกิดการเติบโตของเม็ดผลึก ในระบบนี้พบว่าจะมีสาร 3 สถานะปนกันอยู่คือ ของเหลว ไอ และของแข็ง (ผลึก) ในสภาวะเช่นนี้ การใช้โปรแกรมสำเร็จรูปเชิงพาณิชย์ CFD (CFX 10.0) ในการวิเคราะห์ปัญหาจะทำได้ยากมาก เพราะมีมิติที่ซับซ้อน ในการวิจัยนี้จึงได้สมมุติให้สถานะของแข็ง (ผลึก) ประกอบด้วยอนุภาคเล็ก ๆ ที่เคลื่อนที่ไปกับของเหลวโดยไม่มีการตกตะกอน การจำลองทางตัวเลข พบว่า โปรแกรมสำเร็จรูปนี้สามารถคำนวณ ปัจจัยที่สำคัญในการตกผลึก ได้แก่ ความเร็วของใบกวน การถ่ายเทความร้อนของของเหลวและการระเหยของน้ำ ซึ่งผลของการคำนวณนี้จะช่วยในการปรับปรุงและการออกแบบเครื่องตกผลึกในอุตสาหกรรมขนาดใหญ่ได้เป็นอย่างดี

แบบจำลองที่สองคือ การตกผลึกแบบไม่ต่อเนื่อง แบบถาด (pan crystallizer) ซึ่งใช้ในการตกผลึกน้ำตาลทรายของโรงงานน้ำตาลทั้งหมด แต่งานวิจัยในส่วนนี้ไม่สามารถทำได้ทันเนื่องจากขาดทุนวิจัย สำหรับการต่อสัญญาการใช้โปรแกรมสำเร็จรูป CFD (CFX 10.0)

Abstract

Industrial crystallization units are one of the most important operations in the chemical process industries. It is estimated that over eighty percent of chemical products undergo crystallization at least once during their preparation. However crystallization is also one of the least understood of the industrial processes, and also one of the most difficult to design units for. The current research performed computation fluid dynamic (CFD) analysis for two types of industrial crystallizer to show that it can be used as a tool to improve the design and performance of such crystallizers by improving understanding of the interrelation of the fluid flow, heat transfer, and conditions under which the crystallization occur.

The first crystallizer modeled was a draft tube baffle (DTB) crystallizer which is commonly used in the large-scale crystallization of many inorganic chemical products. The DTB crystallizer uses evaporation of the solvent, in this case water, to produce the supersaturation required for the nucleation and growth of the crystal phase. This means that there are three phases in the crystallizer; the solution phase, water vapor produced from the evaporation, and crystals. This is a very difficult problem for CFD to model in a complex geometry. The solution has been simplified here by assuming that the crystal phase, consisting of very small particles, travels with the liquid phase with the exception of the settling zone used for fines removal. The simulations showed that the significant effects in the crystallizer, such as the effect the agitation speed has on the fines cut size (which is a major determinant of the product particle size), and the effect of the heating rate of the fluid flow and the evaporation rate, could be modeled using the CFD tool. This allows for CFD to improve in the design of the industrial crystallizer by allowing the designer to analyze key points of the design before a crystallizer is built. The second crystallizer to be modeled was a batch vacuum pan crystallizer, a crystallizer which is in use in almost all sugar production plants. A design based on an analysis of key fluid and particle properties, a common geometry of crystallizer and internal heat exchanger (calandria), and key operating parameters has been made. Unfortunately the amount of research funding allocated to the grant in its third year was not sufficient to purchase the CFD software used (CFX 10.0), and therefore the vacuum pan crystallizer simulations could not be completed.

Contents

Figures

Tables

Chapter I
Introduction

1.1 Background and Significance

Crystallization is a separation and purification process where there is a phase transition of one or more species from an amorphous solid, liquid or gaseous state to a crystalline state. In crystallization from solution a species crystallizes from a liquid mixture, which will occur only if the solute concentration exceeds its solubility. This type of solution is said to be supersaturated. Supersaturation can be obtained by many methods such as cooling, evaporation, vacuum, pressure, and reaction, or a combination of these processes. Evaporative crystallization is one of the most common processes used in industrial crystallizers. It is a process in which the mixture requires heating to achieve a supersaturated state.

Crystallization is used in the production of a wide range of materials from bulk commodity chemicals to specialty chemicals and pharmaceuticals. Continuous crystallizers are the most common used for production of industrial chemicals, due to their efficiency of operation, however batch crystallizers are also common and even used in some large scale processes such as the sugar industry. The common configurations of continuous crystallization units include the forced circulation (FC), draft-tube-baffle (DTB), and fluidized-suspension (FS) units. The evaporating or cooling modes can be achieved either adiabatically or isothermally by means of indirect heat input via a heat exchanger (Genck, 2004). In the MSMPR mode (also called circulating magma crystallizers), the liquid phase and the solid phase in the crystallizer are perfectly mixed, and the particle size distribution of the product crystals is the same as the distribution in the crystallizer (Randolph and Larson, 1988). Many industrial crystallizers are designed to modify the crystal size distribution (CSD) by the systems of fines destruction, clear liquid advance (deliberate removal of mother liquor) to change the slurry density and/or product classification.

The design and scale-up of industrial crystallizers is one of the most complex tasks in process engineering and there are many factors to consider, such as yield, selectivity, purity, and particle size distribution. The ease of the separation process increases with an increase in particle size so the prediction of the PSD is an important part of the crystallizer design. The particle size distribution is commonly modeled by population balance equations, as a function of process conditions, crystallizer layout, and type of

crystallization process. This equation is used to describe the crystal population distribution dynamics, and must be tied to the mass balance and energy balance for a full description of the system. It can be influenced through settling, attrition, agglomeration, and local flow conditions. These factors, which are important factors in the design of crystallizers, are based on parameters directly linked to the concept of mixing, such as power input per unit volume (impeller speed), suspension, shear, and heat transfer.

In practice, much of the retained mother liquid in the crystal product is separated by filtration or centrifuging, and the balance is removed by washing with fresh solvent (McCabe, Smith, and Harriott, 2001). The effectiveness of these purification steps depends on the size and uniformity of the crystals. It is clear that the important objectives in crystallization are good yield, high purity, and the appearance and size range of a crystalline product. If the crystals are used in other processes, suitable size and size uniformity are desirable for filtering, washing, reacting with other chemicals, transporting, and storing the crystals. If the crystals are destined for the market, individual crystals that are nonaggregated, uniform in size, and noncaking are necessary. For these reasons the PSD must be controlled tightly.

Uniformity of crystals (a narrow CSD) is an important factor in manufacturing processes. Poor CSD causes problems in manufacturing processes, such as in the filtration step, if the crystals are too small, causing clogging of filter media, increased pressure drop, and damage to the filter. Too large crystal size results in the crystals settling to the bottom of the tank and then agglomerating. A wide range of crystal sizes results in the costs to separate the crystals being increased. Wide CSD also causes marketing problems, such as when the crystal sizes are not in the desirable range, resulting in a low quality product, which reduces the sale price or requires additional post processing to separate and classify.

There are several factors that impact crystal size and uniformity of crystals and the following are the sample of these factors (Tangtonsakulwong, 2003):

1. Flow characteristic and mixing of solution in crystallizer.
2. Crystallization temperature.
3. Concentration of feed solution.
4. Saturation level of solution.

The flow characteristic, mixing, temperature, and density distributions in the crystallizer are important effects in determining the crystal size and uniformity of the

crystals. Good mixing supports the uniformity of the crystals, and hence it is important to study these effects in industrial crystallizers.

In this research work, a DTB crystallizer (or continuous operating vacuum crystallizer with a circulating device, draft tube, and settling space) with an external heat exchanger is used as a case-study for the flow characteristics of solids (crystal), liquid (mother liquor), and vapor in a continuous crystallizer. Research has also begun on a batch vacuum pan crystallizer in the sugar industry as an example of a industrial size batch crystallizer.

There are three methods to study engineering processes: these are experimental, analytical, and numerical methods. Experimental methods are typically high cost methods because of the need to construct a real crystallizer, so it is difficult to study the effects of some parameters that are difficult to change, and it is not possible to control some external conditions or some circumstances in the crystallizer. For analytical methods, the difficulties are based on construction of the mathematical equations and producing reasonable assumptions that result in a system of equations that has an analytical solution. The complexity of the geometry of industrial crystallizer makes analytical solutions impossible to achieve.

Numerical methods are computer aided calculation techniques to find problem solutions. Currently, they are conducted to analyze problems and design process equipments or processes in engineering work. In the fluid dynamics field, computers can analyze problems to find velocity, temperature, pressure, and other physical thermodynamics parameters, and this field is called computational fluid dynamics (CFD). Analysis of the different quantities in the process can be made by this method, which allows researchers to understand the flow phenomena, and to develop or alter the design in the computer model until a desirable solution is obtained before constructing a real system or even a scale-model system. This method reduces cost and time, there is no waste and no risk, it consume less energy and is safer, etc. when compared to the experimental method.

CFD uses a range of space and time discretization methods in order to enable a numerical solution to be calculated. The finite volume technique is the most common method to discretize the volume in commercial CFD code. Firstly the volume being investigated is discretized into small tetrahedral elements with nodes at each corner of the element. The information relating to the simulation is stored in the nodes of the elements, and equations of flow can then be applied to each finite volume in the simulation. The last

pieces of information that are required by the software are the boundary conditions for each of the boundaries of the total volume (flow rate at the inlet, conditions at outlet, etc,...), the physical properties of the fluid(s) and particles in the system, and the physical model that are required for the system.

Due to the advantages of the CFD technique, this work is conducted using the commercial CFD software "ANSYS CFX-10.0" to perform the 3D (three dimensional) simulation with the finite volume method using an unstructured mesh to study the two-phase (vapor-liquid) flow and heat transfer behavior of turbulent steady in the DTB crystallizer with external heat exchanger, and to commence modeling for an industrial scale batch vacuum pan for sucrose crystallization.

1.2 Objectives

The objectives of this study are the following:

(1) In the DTB crystallizer, the aim is to

- Study the two phase (vapor and liquid) flow characteristics in the DTB crystallizer. The solid (crystal) flow in these crystallizers typically follows the liquid flow, except at very low fluid flow velocities, because of the small size of the crystals (typically in the range of 0.1 mm length or smaller).

- Study the effect of the product crystal suspension flow rate and fines removal flow rate to the flow characteristics and the classification of product crystals.

- Study the effect of the momentum source (this is the representation of the impeller speed) to the flow characteristics and the classification of product crystals.

- To study the effect of the heat and mass transfer via the evaporation of liquid to the flow characteristics and the classification of product crystals.

(2) In the vacuum pan crystallizer the plan is to determine the fluid mixing characteristics in the vacuum pan in order to determine whether modifications can improve the consistency of the temperature and supersaturation throughout the crystallizer. (In vacuum pan crystallizers it is common due to mixing and heat transfer limitations to have large variations in temperature in the crystallizer, which causes large variations in supersaturation also.

1.3 Scope and Assumptions of Work

1.3.1 Overall scope and assumptions

- The work is divided into three parts; modeling the DTB crystallizer using isothermal simulation, modeling the DTB crystallizer using non-isothermal simulation, and modeling of the vacuum pan crystallizer.

- The flow in the crystallizer was modeled by the two phase (vapor and liquid) flow with the solids considered to follow the liquid flow.

- In the DTB crystallizer a water solution with 26.66 % NaCl is the liquid phase in the crystallizer, and water-vapor is the vapor phase. The physical properties of these materials are constant. The solubility of NaCl remains almost constant with temperature. In the vacuum pan crystallizer the liquid is assumed to be a sucrose solution with a 2 % relative supersaturation at the average temperature of the pan. The steam coils in the crystallizer produce pure water vapor from the solution.

- In the DTB crystallizer the impeller was modeled as an axial momentum source term (Pericleous and Patel, 1987) that has been added at the base of the draft tube, at the position and size of the true impeller. This model can reduce the computation time and model complexity compared to modeling a real impeller. The radial momentum source is not necessary because it does not create a significance difference to the fluid flow profile in baffled vessels (Tangtonsakulwong, 2003). Vacuum pan crystallizers usually do not contain impellers, and mixing is achieved mainly though the lift created by the rising water vapor through the pan.

- Steady state flow is assumed throughout because the industrial crystallizer is mostly operated as a continuous process, with the mass flow rate of the inflow stream equal to the outflow stream. Even though the vacuum pan is batch, it should be modeled over a short time period during which a quasi steady-state is assumed. The complexity of a non-steady-state model in such a complex system is beyond the scope of the research due to computational and time limitations.

- Turbulent flow is assumed throughout the DTB crystallizer because the mixing process in such crystallizers containing relatively dilute aqueous solutions produces turbulent flow. Past experience with CFD of sucrose solutions (Tangtonsakulwong, 2003) has shown that laminar flow modeling is usually adequate, although this should be confirmed by analysis of simulation results.

- The crystallizers were studied using the CFD modeling software ANSYS CFX-10.0. A 3D geometry was used to account for the strong 3D flow.

1.4 Outcomes of the research

The outcomes of this research are following:

- Better understanding of the flow phenomena in DTB crystallizers has been achieved, which leads to a better description of the cause of feed flow, fines removal flow, product crystals flow, momentum source (or impeller speed), and heat and mass transfer via the evaporation of liquid to the flow characteristics and product crystals size.

- The study aids in the design and upgrade of industrial crystallizers.

- The study improves CFD knowledge for the chemical process industries.

- The study has strengthened the use of CFD in the process industries in Thailand through development of researchers in the area.

Chapter II

Theory and Literature Review

The Theory and Literature Review section will focus on crystallization from solution, industrial crystallizers, the effect of hydrodynamics in crystallizers, CFD modeling for crystallizers and summations of the published literature.

2.1 Crystallization from Solution

Crystallization from solution is a process whereby a solute crystallizes from a liquid solution containing the solute within a solvent. Crystallization from solution occurs when the solute concentration in a solvent exceeds its solubility. Figure 2.1 shows the solubility of a general solution, where c_s is the saturation concentration and relative supersaturation is defined as

$$s = (c\text{-}c_s)/c_s \tag{2.1}$$

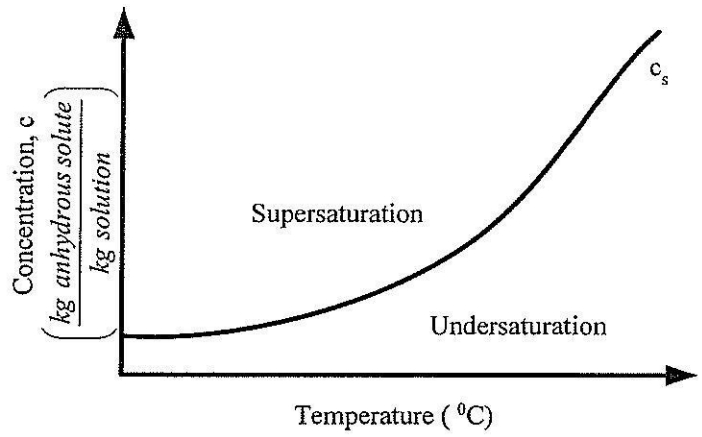

Fig. 2.1 Solubility of a general solution.

Crystallization at different supersaturations causes different crystal sizes and shapes. Therefore, a good CSD will occur by having the supersaturation uniform throughout the crystallizer; good mixing in the crystallizer supports this purpose.

Industrial crystallization from solution is carried out in a wide range of processing equipment, but we can draw a general schematic, as in Figure 2.2. The following terms are typically used to distinguish particular modes of operation:

2.1.1 Continuous, steady-state crystallizer

The mass flow rates of the inflow stream equal the outflow stream. There is (essentially) no time variation in any of the crystal or fluid properties in the unit. The unit will not operate at equilibrium conditions at any time.

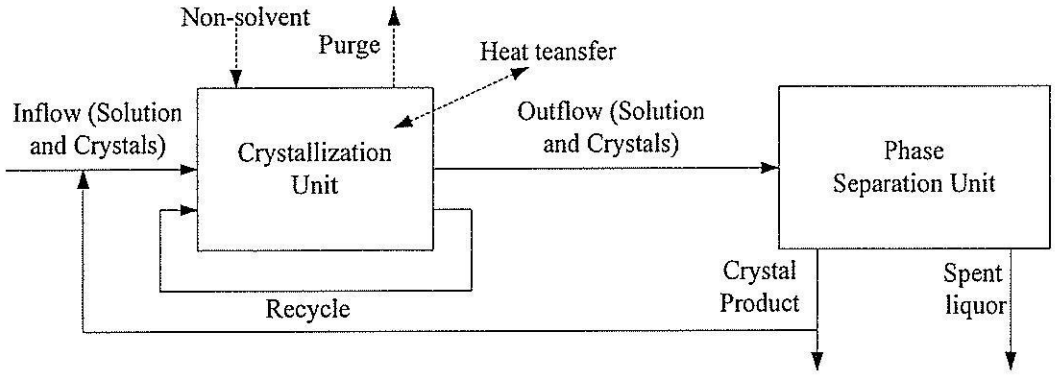

Fig. 2.2 General schematic of a crystallization process. (Flood, 2003).

2.1.2 Batch crystallizer

There are no inflow and outflow streams (batch mode) or one of the inflow or flow streams (semi-batch mode) is not present in these types of crystallizers. The fluid and physical properties in the vessel will vary with time (unsteady-state) during the batch. The contents of the vessel may be allowed enough time to reach a state very close to the equilibrium condition, or the batch may be completed before this time. This crystallizer is not common for large scale operations since they usually require larger operating and equipment cost. The main advantages of this crystallizer are that they can produce a narrow range of product crystal sizes, can sometimes produce slightly more pure products and are very flexible for plants that produce small quantities of a wide range of products.

2.1.3 Seeded crystallizer

In seeded crystallizers, solute crystals are added to the feed of the crystallizer to initiate crystallization. The purposes of this operation are to be done to remove the requirement to operate at driving forces high enough to produce nuclei (since crystals already exist in the liquor the nucleation step is not required), or to promote the formation of the low numbers of nuclei at low driving forces. Seeding may be performed in both batch and continuous crystallizers.

2.1.4 Cooling crystallization

The process of cooling crystallization can be used when the solubility of solute greatly increases as the temperature increases; $NaNO_3$, NH_4CO_3, $NaClO_3$, KNO_3, etc. are example of this type of solubility (see Figures 2.3). The simplest type of this process is where the solution is evaporated at high temperature, where the solubility is high (the solution is undersaturated) before being fed to the crystallizer. This feed solution is cooled via either an external jacket or a cooler inside the crystallizer until the crystallizing species becomes supersaturated (while the amount of solute is constant), and thus crystal is produced.

2.1.5 Evaporative crystallization

The process of evaporative crystallization can be used when the solubility of the solute increases only slightly, remains almost constant, or even decreases with temperature; NaCl is an example of this solubility (see Figure 2.3). The concepts of this mode are that the undersaturated solution is fed into the crystallizer, and then this feed solution is heated to the boiling point of the solution so that the solvent evaporates. The boiling point of the solution is usually a function of pressure so boiling tends to take place at the surface of the liquid, which can lead to a high level of supersaturation. On the other hand, in crystallizers where there are heat transfer tubes in the bulk solution and weak mixing (i.e. sugar crystallization) the hottest is near the tubes, and boiling occur there despite the pressure differential.

2.1.6 Vacuum crystallization

In vacuum crystallization, the solution is evaporated and cooled simul-taneously by decreasing the temperature and pressure. The vacuum is often created above the liquid level and maintained by steam jet compressors. When the evapo-ration is occurring, the solution loses the energy required to evaporate the solvent (heat of evaporation) causing the solution to cool and become supersaturated (in addition to the supersaturation caused by solvent loss), and thus partially crystallize.

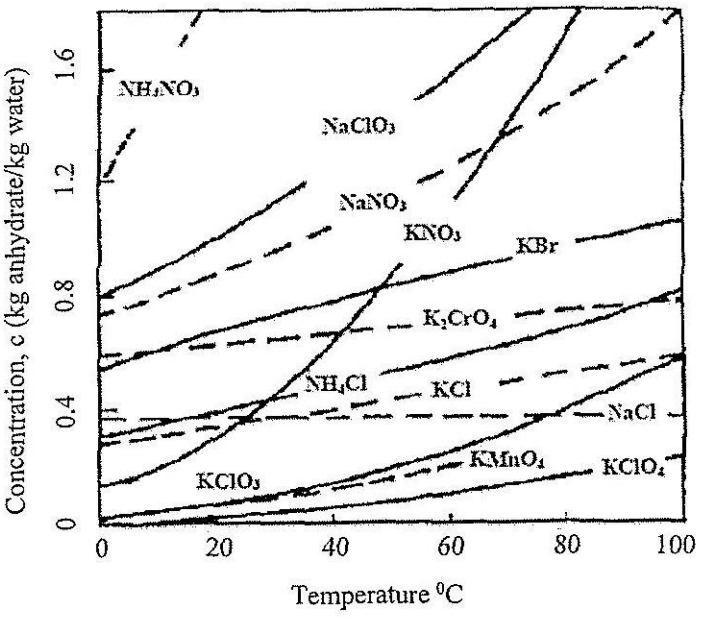

Fig. 2.3 Solubility curves for several anhydrates. (Mersmann, 2001).

2.1.7 Non-solvent drowning-out crystallization

If the supersaturation required for the crystallization is achieved through the addition of a solvent designed to reduce the solubility of the solute, the process is known as a non-solvent (or anti-solvent) crystallization. The addition of other solutes (other crystallizable species; species not considered as solvents) designed to reduce solubility is known as drowning-out crystallization. Drowning-out crystallization may offer the advantage over other processes of reducing energy consumption; as the enthalpy of evaporation of drowning-out agents is usually considerably smaller than that for solvent. This process can be combined with other processes that enable energy to be saved.

2.1.8 Reaction crystallization (or precipitation crystallization)

Reaction crystallization is where supersaturation is achieved by adding individual reagents to the crystallization vessel. The reaction product forms at a concentration higher than its solubility.

2.2 Industrial Crystallizers

2.2.1 Industrial crystallization apparatus

In industrial crystallization from solution, where crystals are generated out of a solution in a crystallizer, the suspension must be mixed, and deposition onto the equipment

must be avoided. This leads to the entire suspension, including coarse crystals needing to be circulated by the circulating device (stirrer or axial/radial pump). In the former case, relatively strong attrition occurs, especially of large crystals. Figure 2.4 shows typical industrial crystallizers. The fluidized-bed (FB) crystallizer differs from other crystallizers by the fact that a suspension flow containing only small crystals (e.g. under 100 μm) is conducted by the circulation device (pump). The advantage of the FC and the FB over the STR is that the ratio of the heat exchanger surface to the crystallizer volume can be maintained when scaling up the crystallizers due to the external heat exchanger.

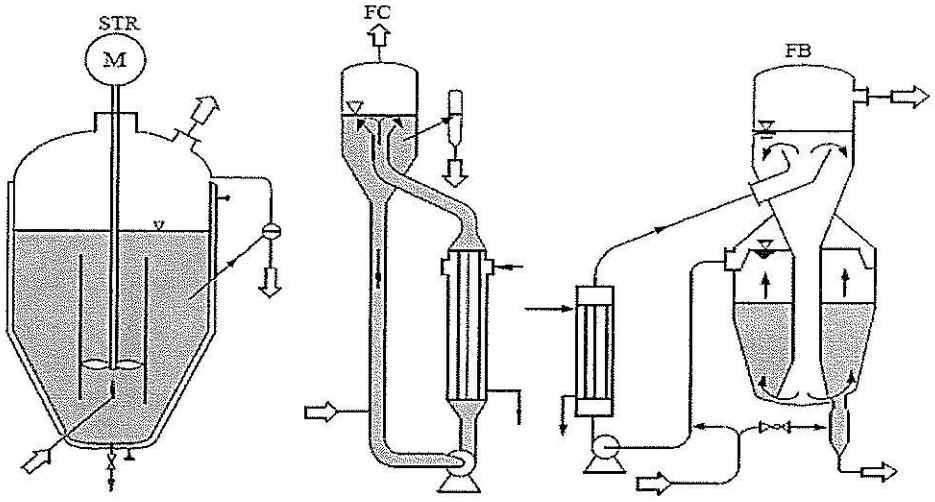

Fig. 2.4 Typical industrial crystallizers. (Mersmann, 2001).

The FB crystallizer is illustrated in Figure 2.5(a) and 2.5(b); this type of crystallizer is a classifying crystallizer to attain spatial separation of supersaturation- and growth by external circulation of the solution. The growth zone is designed in such a way that a fluidized bed is created by the upward flow. The crystals remain at certain level, depending on their size.

Figure 2.5(a) shows a cooling crystallizer with an external heat exchanger. A small flow of warm, concentrated inlet solution is added directly to the much larger circulating flow upstream of the heat exchanger. The supersaturated solution in the heat exchanger enters the crystallization chamber at bottom of the crystallizer and suspends the crystals. Despite the minimal temperature difference allowed (usually under 2 K) between the circulated solution and solvent, high heat flux densities can be obtained. The solid is

separated by enlarging the flow cross-section. The growing crystals sink to lower levels by their rate of sedimentation until they finally reach the product outlet.

Figure 2.5(b) shows an evaporative crystallizer with an external boiler, it looks like the previous type but has a different method of reaching supersaturation (evaporation rather than cooling). The evaporation unit and crystallizer are joined directly to each other. The crystallization vessel is connected to the heat exchanger by the circulation pump and the fresh solution is fed into the circulation flow.

Figure 2.5(c) shows a vacuum crystallizer with separate crystallization and evaporation chambers. This does not have a heat exchanger, and is the crystallization vessel is an open vessel under atmospheric pressure. The difference in pressure to the vacuum part is compensated by the hydrostatic pressure of the liquid. Crystallization occurs due to the evaporation of solvent and also the cooling effect caused by the evaportation.

Figure 2.5(d) shows a vacuum crystallizer with upward flow in the tube and agitator baffles. This crystallizer type produces a coarse crystal product. The circulating device is built into the lower part of the draft tube. Fresh solution is fed directly into the tube. The crystals enter the vicinity of the vaporizing surface, where supersaturation is largest. Fines can be removed by an overflow in the ring chamber. The coarse part of a narrow crystal size distribution is separated by a screening tube at the lower end of the crystallizer.

Figure 2.5(e) shows a two suspension circulation flow in fluidized-bed crystallizer, which has two concentric tubes, a bottom tube with a circulating device and external ejection tube and continuous gap around the crystallizer. A fine product exists primarily in the inner circulation loop, which has a fast upward flow in the inner tube and a high supersaturation value at the evaporation surface. In the external chamber, a classifying fluidized bed is formed and coarse crystals exist; fine crystals are carried away and drawn into the inner circulation via the ejector gap. The overflow above the classifying zone influences the crystal contents. Fresh solution is fed directly into the tube. The product is withdrawn from the classifying zone.

Figure 2.5(f) shows a multistage crystallizer in a horizontal position without moving parts. It is suitable for vacuum-cooling crystallization. The evaporation chambers are separated from each other by several partitions. Fresh solution is fed in at the first stage and is cooled continuously from stage to stage. The product is withdrawn from the last

stage, which has the lowest pressure. Steam jets maintain the various low pressures. In many cases, the liquid is brought into motion in the individual stage by bubbling gas (air) through the stage.

The final crystallizer is shown in Figure 2.5(g). In this crystallizer an air flow cools the solution and causes the solvent to evaporate. The solid crystals drop to the floor of the prilling tower, from where they are mechanically transported to a cooling drum.

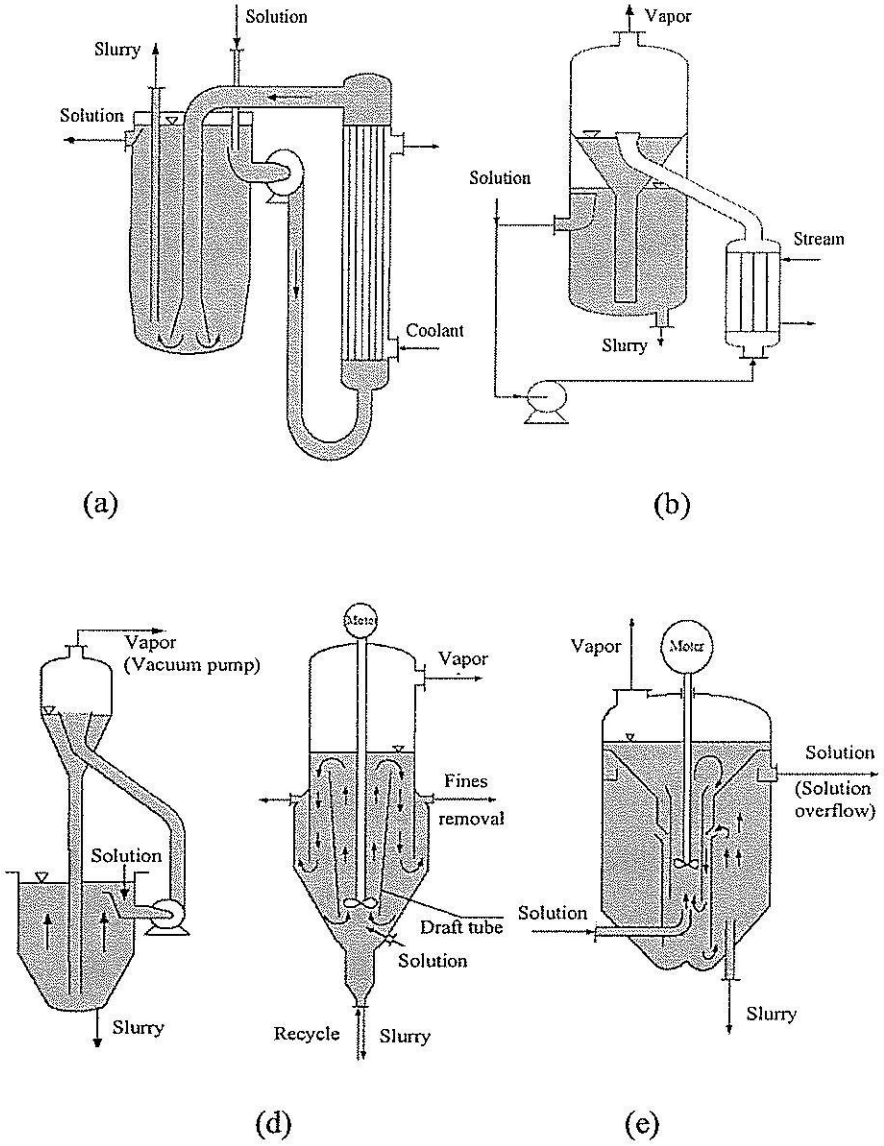

Fig. 2.5 Industrial crystallization apparatus. (a) cooling crystallizer; (b) evaporative crystallizer; (c) vacuum crystallizer; (d) continuously operated vacuum crystallizer with a circulating device; (e) vacuum crystallizer with a circulating device in a tube; (*continued*)

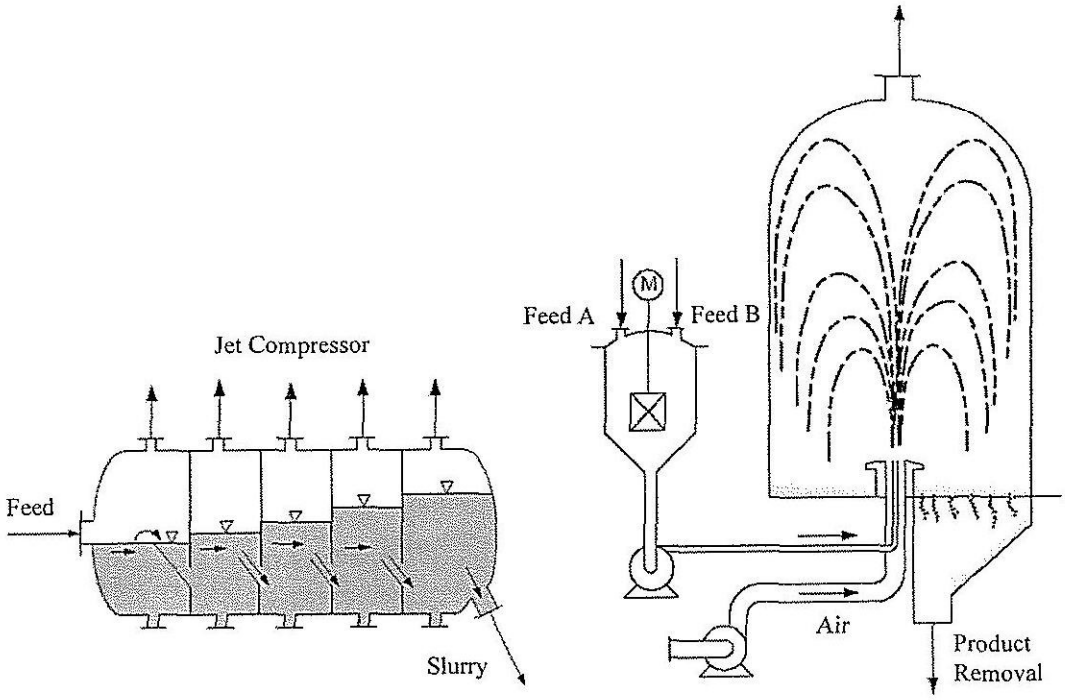

Fig. 2.5 (*continued*) (f) horizontal five-stage vacuum crystallizer; (g) prilling tower for production of calcium nitrate. (Mersmann, 2001).

2.2.2 Draft tube baffle (DTB) crystallizer

The DTB crystallizer is shown in Figure 2.6 (which is similar to Figure 2.5 (d)). This is a vacuum crystallizer with upward flow in the tube and agitator baffles, which consists of a body which has growing crystals and circulation from the lower portion to the boiling surface. The mechanical circulation has a significant impact on the level of nucleation in the crystallizer. For this reason, low speed impellers in the draft tube are sometimes incorporated into the body to reduce the shear force seen by the circulating pump. Surrounding the suspended magma of growing crystals is an annular settling zone; in this zone a stream of mother liquor can be removed and fine crystals follow this stream. The fine crystals separate from the growing suspension of crystals by the gravitational settling in the annular baffle zone.

In the case of evaporative-DTB crystallizers, fine crystals in the mother liquor leaving the baffle zone are sent to a settler and heat exchanger. The fines are destroyed by heating, mixed with dilute feed, or water, and the warm or heated mother liquor is returned to the suction of the propeller circulator. Incoming feed is also mixed at the eye of the

propeller. In this evaporative crystallizer, the temperature rise in the circulated magma caused by the mixing of the feed or heated mother liquor is in the order of 1 °C.

The amount of temperature change as the slurry is pumped through the boiling surface limits the amount of supersaturation created per pass to about 1 °C and thereby limits the nucleation rate to very low values. The boiling action is concentrated mostly in the center of the vessel and is well distributed across the surface by vertical inlet. The active volume of a DTB (including areas inside and outside the draft tube and excluding areas behind the baffle), which typically contains a solids loading equal to 25-50 % of the apparent settled volume. The decreasing crystal-lization buildup on the wall of the crystallizer and extending the operating cycle can be achieved by lowering the temperature drop at the boiling surface, and creating a uniform distribution of boiling created by the circulation pattern.

In the fines removal process, the residence time for the fines is less than the residence time for the product. The baffles can be segmented to one or more settling sections and are utilized to separate fine crystalline material from coarse crystals. Changing either the flow rate in the active baffle area or the amount of baffle area is used to control the CSD in the body of the crystallizer via the vertical velocity of the slurry in the baffle area, and the maximum crystal size that will be removed and dissolved.

Increasing the solids content of the slurry within the crystallizer body is sometime done by withdrawing a stream of mother liquor from the baffle zone, which increases the thickness of the slurry in the body. High slurry densities tend to reduce the efficiency of baffle performance. To improve performance, one may add a lamella plate in the main body to direct the flow vertically at the baffle entrance, or install alternating donut baffles in the settling zone behind the regular baffles. These donuts dissipate large liquid eddies that can trap and carry out undesirable larger crystals.

All techniques used in this crystallizer are employed to produce a larger product crystal size with a narrow size distribution. This type of crystallizer is used primarily in production of a variety of large-size crystalline material such as ammonium sulfate, potassium chloride and diammonium phosphate for the fertilizer industry.

An example of this crystallizer is shown in Figure 2.6. It is equipped with an external heat exchanger; generally, this type of crystallizer can be equipped with an internal heat exchanger, where the heat exchanger is directly attached to the draft tube. For the evaporation mode the saturated solution is directly fed to the crystallizer. Other

configurations of this crystallizer are shown in Figure 2.7, which the shape of the tank bottom of this configuration is rounded tank "corners" and a center peak under the agitator.

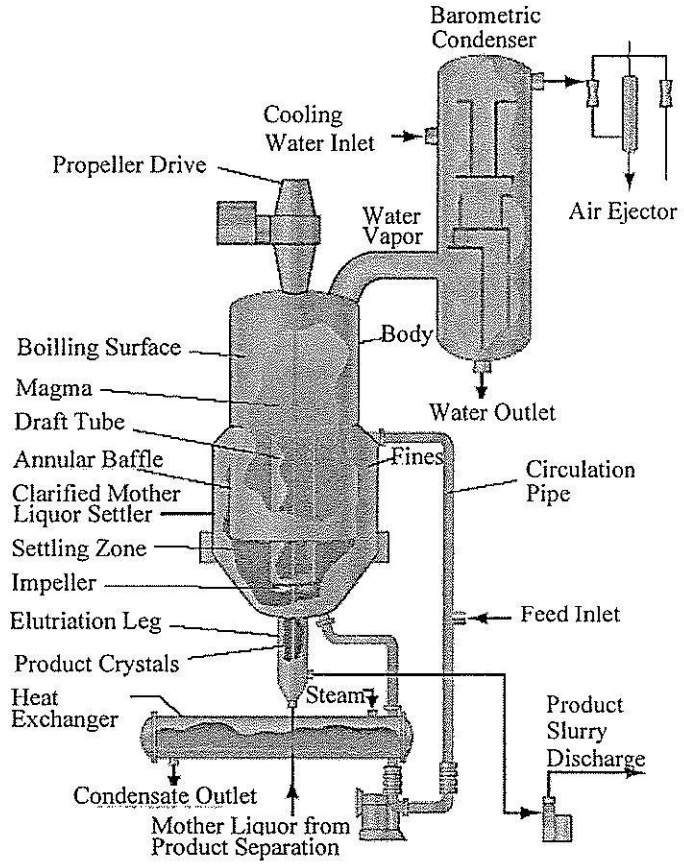

Fig. 2.6 Swenson DTB crystallizer. (Genck, 2004).

2.3 The effect of hydrodynamics in crystallizer

The role of hydrodynamics is one of the key aspects in the dynamic behavior of a crystallization process. On a macroscopic scale the hydrodynamics conditions control the crystal residence time and the circulation time in the crystallizer (which control the solid suspension in the crystallizer). On a microscopic scale, the smallest scale flow determines the crystal collisions (a source of secondary nucleation and agglomeration) and mass transfer for crystal growth. This research investigates the hydrodynamic conditions where fluid-particle flow and mixing are concerned.

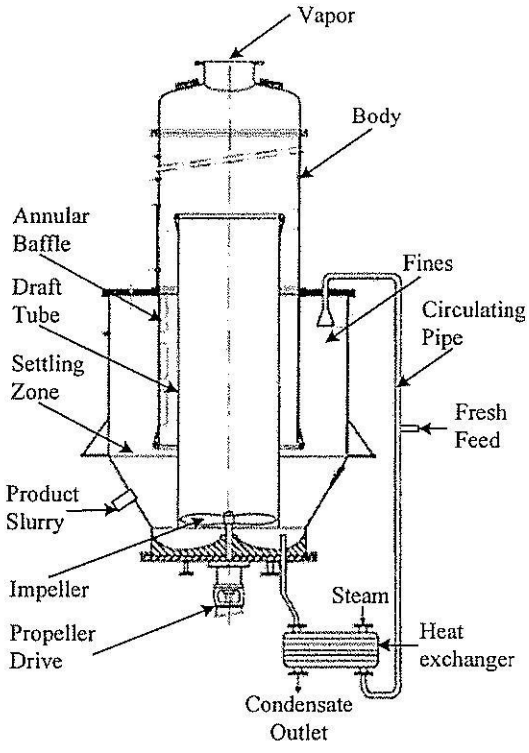

Fig. 2.7 DTB crystallizer. (Kramer *et al.*, 1996).

2.3.2 Introduction to mixing in the crystallization process

Crystallization is usually carried out in a suspension, so knowledge of mixing is important to study the crystallization process. Both mixing between fluid and particles, and particles and particles affect the crystallization process. The mixing effect is mainly considered on two scales of mixing. One is macromixing, i.e. residence time distribution, which defines retention time of the elementary volumes, and the other is micromixing, which describes communication between elementary volumes (Sha and Palosaari, 2000).

Successful operations depend on identifying the mixing parameters for the most critical aspects of the process and then evaluating whether those parameters will be satisfactory for the other aspects. The crystallizers normally employed in the fine chemical and pharmaceutical industries are multipurpose vessels with various impellers, baffles, and draft tube configurations. The pitched blade turbine is an axial flow impeller and can create good circulation at relatively low shear. These attributes help reduce secondary nucleation and crystal breakage while achieving good suspension and circulation. The flat-blade turbine is less applicable because of high shear and less overall circulation. Baffles are required to prevent poor mixing due to swirling as well as entrainment of vapor that can

provide nucleation sites. A draft tube is usually installed centrally within the vessel. An axial flow impeller located inside the draft tube is used to provide an efficient top-to-bottom circulation pattern, which is important for flow controlled process (Paul, Atiemo-Obeng, and Kresta, 2004).

A pitched blade turbine (see Figure 2.8) is the most commonly used agitator in DTB crystallizers. It is an axial flow impeller and consists of a hub with an even number of blades bolted and tack-welded on it. It is heavier than a propeller of the same diameter. The blades can be angle between 10 and 90° from the horizontal, but the most common blade angle is 45°. The flow discharge from a pitched blade impeller has components of both axial and radial flow velocity in low to medium viscosity liquids and is considered to be a mixed-flow impeller with 50% axial flow and 50% radial flow.

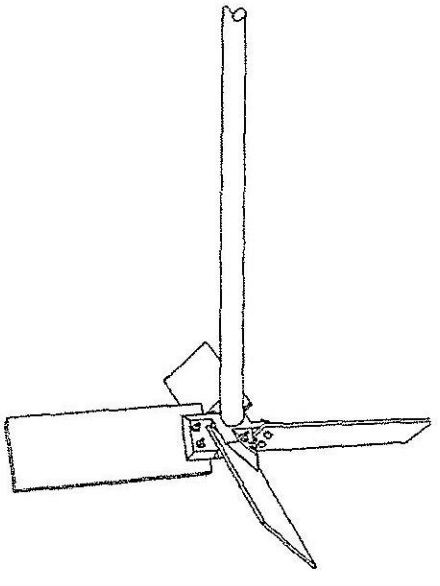

Fig. 2.8 Pitched blade turbine. (Perry and Green, 1997).

The location and design of inlets and outlets are based on the process, type of feed, and sensitivity of the process result to the rate of feed dispersion. For slow batch processes, the feed inlet can be from the top. It should be pointed at an active surface away from the tank wall and the impeller shaft. For processes requiring quick dispersion of feed, the inlet nozzle should be located in a highly turbulent region such as the suction or discharge of the impeller. The inlet nozzle should be sized to prevent backmixing of the tank contents into the inlet pipe, where lack of mixing may cause poor process results.

Air feeds can affect the power required for the impeller to operate the mixing tank reactor, with different inlet air velocity conditions resulting in different amounts of impeller power (when air is located under the impeller) as discussed by Kleinstreuer (2003). This research shows that less power is required by the impeller to mix the two phases when more air is injected into the mixing tank. This discussion can be related to other mixing processes, such as liquid feeds, but the feed must be located under the impeller.

The outlet is generally located on the side near the tank bottom or in the bottom head if the vessel needs to be drained completely. When solids are present, this bottom outlet can get plugged and can cause poor contacting of liquid and solids unless fitted with a flush-bottomed valve. A small impeller, installed very close to the tank bottom, also helps to eliminate this problem and provides mixing at low liquid levels. In continuously operated agitated tanks, the outlet must be located far from the inlet to minimize short-circuiting of the feed.

2.3.3 Particle settling

Particles heavier than the suspending fluid may be removed from a gas or liquid in a large settling box or tank, in which the fluid velocity is low and the particles have ample time to settle out (McCabe *et al.*, 2001). A device that separates the solids into two fractions is called a *classifier* and most classifiers in chemical processes separate particles on the basis of size. The annular settling zone of the DTB crystallizer shown in Figures 2.6 and 2.7 are examples. If the upward velocity of the liquid is smaller than the terminal settling velocity of acceptable large crystals, the large crystals are separated (settled); this device carries unwanted fine crystals back to the crystallizing zone for the further growth, or alternatively is used to destroy fine crystals by removing them and dissolving them.

A dense solid particle placed in a quiescent fluid will accelerate to a steady state settling velocity (free or terminal settling velocity). This velocity occurs when the drag force balances the buoyancy and gravitational force of the fluid on the particle.

Correlations for the terminal settling velocity have been derived for spherical particles. In newtoniam fluid, the terminal settling velocity, U_t, is calculated by expression (McCabe *et al.*, 2001).

$$U_t = \sqrt{\frac{4g(\rho_p - \rho)d_p}{3C_D\rho}} \qquad (2.2)$$

where g is the gravitational constant (9.81 m/s^2), ρ is the liquid density, ρ_p is the particle density, d_p is the particle diameter, and C_D is the drag coefficient. The corresponding ranges for Re_p and the correlating expression for C_D are shown in Table 2.1 for the three hydrodynamic regimes.

When the expressions for C_D are substituted in equation (2.2), the resulting expressions for free settling velocity, U_t are:

For the Stokes' law (laminar, $Re_p < 0.2$) regime:

$$U_t = \frac{g d_p^2 (\rho_p - \rho)}{18\mu} \tag{2.3}$$

For the Newtons' law (turbulent) regime, $Re_p > 500$:

$$U_t = 1.75\sqrt{\frac{g d_p (\rho_p - \rho)}{\rho}} \tag{2.4}$$

Table 2.1 Hydrodynamic regimes for settling particles.

Regime	Reynolds Number	C_D Expression
Stokes' law (laminar)[1]	$Re_p < 0.2$	$C_D = 24/Re_p$
Intermediate law[2]	$0.2 < Re_p < 500$	$C_D = 18.5/Re_p^{3/5}$
Newton's law (turbulent)[1]	$500 < Re_p < 3.5 \times 10^5$	$C_D = 0.44$

Sources: [1]Yang (2003); [2]Paul *et. al.* (2004)

The above expression of settling velocity is based on the hydrodynamics of a single particle. If other particles are present in the system the settling velocity is lower due to a mechanism called *hindered settling*. Hindered settling occurs because of (1) the interactions with surrounding particles, (2) interactions with the upward flow of fluid created by the downward settling of particles, and (3) increases in the apparent suspension

viscosity and density (Paul *et al*,. 2004). An empirical correlation for hindered settling in monodispersed (single particle size) suspensions is reported by Maude (1958) as

$$U_{ts} = U_t(1-\chi)^n \tag{2.5}$$

where U_{ts} is the hindered settling velocity, χ the volume fraction of solids in the suspension, and n is a function of the particle Reynolds number as follows: $n = 4.65$ for $\mathrm{Re}_p < 0.2$, $n = 4.375\mathrm{Re}_p^{-0.0875}$ for $0.2 < \mathrm{Re}_p < 500$, and $n = 2.33$ for $\mathrm{Re}_p > 500$.

2.3.6 Previous fluid dynamic studies relating to crystallizers

A literature survey on fluid dynamics studies on crystallizers and similar processing equipment has been given in the Thesis of the student on this project, Wirapong Wantha (Wantha, 2008). This review is omitted here for conciseness.

2.4 CFD Modeling for Crystallizers

2.4.1 Introduction to CFD

Computational Fluid Dynamics (CFD) is a computer-based tool for simulating the behavior of systems involving fluid flow, heat transfer, and other related physical processes. It works by solving the equations of fluid flow (in a special form) and the equation for heat transfer over a region of interest, with specified (known) conditions on the boundary of that region.

CFD is used to predict a system's performance in various areas, which can potentially be used to improve the efficiency of existing systems as well as the design of new systems. It can help to shorten product and process development cycles, optimize processes to improve energy efficiency and environmental performance, and solve problems as they arise in plant operations. There are applications of CFD in chemical processes, in particular where predicting the characteristics of fluid flow and temperature gradients are important: these include mixers, reactors, fluidized packed beds, crystallizers and dissolving vessels.

The process of performing a single CFD simulation is split into four components as shown in Figure 2.9.

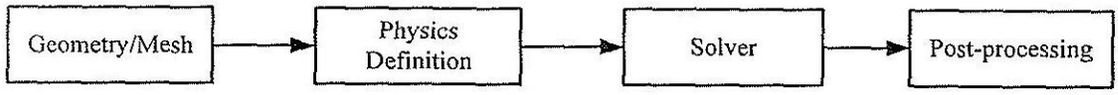

Fig. 2.9 CFD modeling procedures.

Geometry/Mesh: This process is the first pre-processing stage. The objective is to produce a mesh for input to the physics pre-processor. Before a mesh can be produced, a closed geometric solid is required.

Physics definition: This interactive process is the second pre-processing stage and is used to create the input required by the solver. The physical models which are to be included in the simulation are selected. Fluid properties and boundary conditions are specified in the physics definition.

The solver: The component which solves the CFD problem is called the solver. It produces the required results in a non-interactive/batch process. The CFD problem is solved as follows:

1. The partial differential equations are integrated over all the control volumes in the region of interest. This is equivalent to applying a basic conservation law (e.g. for mass or momentum) to each control volume.
2. These integral equations are converted to a system of alge-braic equations by generating a set of approximations for the terms in the integral equations.
3. The algebraic equations are solved iteratively.

The solver produces a results file which is then passed to the post-processor.

The post-processor: The post-processor is the component used to analyze, visualize and present the results interactively. Post-processing includes anything from obtaining point values to complex animated sequences.

2.5 Conclusions

Previous research has clearly shown that CFD can be used to design and upgrade industrial mixing systems and industrial crystallizers. From previous studies it can also be seen that there is only very limited research on CFD modeling of two phase (vapor-liquid) flows in industrial crystallizers. Therefore, this work will model the vapor-liquid flows in common industrial crystallizers using the CFD modeling software ANSYS CFX-10.0.

Chapter III

Mathematical Models Used in the Study

In the crystallizers studied there are three phases: liquid (mother liquor); gas (water vapor); and solid (crystal). However, for convenience such crystallizers can be analyzed as a two phase flow (liquid and vapor) system, which is an acceptable approach considering the particles are mostly sufficiently small to be considered to follow the liquid flow, and that the particle suspension is reasonably dilute so that the impact of solids on the flow field is negligible. If a more exact description of particle flow-lines is required it is possible to do this using the two-phase simulation results and using a Lagrangian model for the particles. The DTB crystallizer was studied using the CFD modeling software ANSYS CFX-10.0. 3D (three dimensional) geometry was used to account for the strong 3D flow.

The aim of this chapter is to show the mathematical models describing the physical phenomena that occur during the fluid flows in this system. Not all equations presented here are written in the form used by the ANSYS CFX program: see ANSYS CFX-10.0 Manual, ANSYS Canada Ltd. (2005).

3.1 Introduction

Multiphase flow refers to systems where more than one fluid is present. In this work the Eulerian-Eulerian multiphase model was used to simulate the vapor-liquid flow in the DTB crystallizer.

The Eulerian-Eulerian multiphase model is designed for two or more immiscible fluids (fluids that can not be uniformly mixed with another fluid, and are separated by a distinct interface) and two or more interpenetrating fluids (fluids that can be uniformly mixed or blended with another fluid). The different phases are simulated by treating them as interpenetrating continua. Phase volume fractions are introduced because it is clear that the volume occupied by a phase cannot be occupied by any other phase. The share of the flow domain each phase occupies is given by the phase volume fraction. The volume fractions of the phases are predicted based on the condition that the sum of the volume fractions for all phases is equal to 1 at all times, and in all control volumes. Conservation equations for each phase are derived to obtain a set of equations that have a similar structure for all phases. Within the Eulerian-Eulerian model in CFX, the interphase transfer

terms can be modeled using the particle model, the mixture model or the free surface flow model.

Because the liquid and vapor above the mother liquor in this system are separated by a distinct interface, the free surface flow model should be used to model vapor-liquid two phase flow (gas bubble in the bulk liquid). The free surface flow model is a multiple flow simulation, and separates into homogeneous and inhomogeneous flow models.

The homogeneous flow model is a limiting case of multiphase flow where all fluids share the same velocity fields and other relevant field such as temperature, turbulence, etc. The pressure field is shared by all fluids.

The inhomogeneous flow model can be used to allow the two phases to separate. This will be required if entrainment of one phase within another occurs and it is desired to allow the phases to separate again. In this model, separate velocity fields and other relevant fields exist for each fluid. The pressure field is shared by all fluids. The fluids interact via an interphase transfer term.

In this work, an inhomogeneous model was considered. In this model, liquid is a continuous phase and vapor is a dispersed phase or dispersed fluid, which is a fluid which is present in discrete regions which are not connected.

There are two parts of study for the DTB crystallizer in this work: these are the modeling the DTB crystallizer with inhomogeneous free surface flow (free surface model) using isothermal simulation and the modeling the DTB crystallizer with inhomogeneous two-phase flow (particle model) using non-isothermal simulation (this part contains no model of the area above the liquid free surface, and the liquid free surface is considered to be flat and frictionless). For the vacuum pan crystallizer a non-isothermal simulation is necessary since there is considerable variation in temperature throughout a typical vacuum pan crystallizer.

3.2 Mathematical Models

In this section, the governing equations of fluid flow and heat transfer, and the turbulence model are described. The governing equations of fluid flow and the turbulence model were used in the isothermal simulation part and all sets of governing equations were used in the non-isothermal simulations. The material is in many places taken from the CFX-10 manual, with additions or changes where necessary.

3.2.1 The continuity equation

The continuity equation is a mass balance for a phase and is shown in concise form below

$$\frac{\partial(r_\alpha \rho_\alpha)}{\partial t} + (\nabla \bullet r_\alpha \rho_\alpha \mathbf{U}_\alpha) = \mathrm{S}_{MS,\alpha} + \sum_{\beta=1}^{N_p} \Gamma_{\alpha\beta} \tag{3.1}$$

In this equation

- $S_{Ms\alpha}$ are mass sources if such need to be created for the simulation.
- $\Gamma_{\alpha\beta}$ is the mass flow rate per unit volume from phase α to phase β. This term only occurs if interface mass transfer occurs.

In the crystallizer the system is at steady state, with no mass source and no phase change, so that equation (3.1) becomes

$$(\nabla \bullet r_\alpha \rho_\alpha \mathbf{U}_\alpha) = 0 \tag{3.2}$$

where r_α, ρ_α, $\mathbf{U}$, are the volume fraction, phase density, and Cartesian velocity component respectively, of phase α. The equation of continuity of each phase can be written for each phase as equations 3.3 and 3.4.

For the vapor phase (the dispersed phase):

$$(\nabla \bullet r_d \rho_d \mathbf{U}_d) = 0 \tag{3.3}$$

For the liquid phase (the continuous phase):

$$(\nabla \bullet r_c \rho_c \mathbf{U}_c) = 0 \tag{3.4}$$

3.2.2 The momentum equation

The momentum equation takes the form of equation 3.5.

$$\frac{\partial}{\partial t}(r_\alpha \rho_\alpha \mathbf{U}_\alpha) + \nabla \bullet (r_\alpha \rho_\alpha \mathbf{U}_\alpha \mathbf{U}_\alpha) = -r_\alpha \nabla p_\alpha + r_\alpha \rho_\alpha \mathbf{g} + \nabla \bullet r_\alpha \mu_\alpha \left(\nabla \mathbf{U}_\alpha + (\nabla \mathbf{U}_\alpha)^T\right) + \sum_{\beta=1}^{N_p} (\Gamma^+_{\alpha\beta} \mathbf{U}_\beta - \Gamma^+_{\beta\alpha} \mathbf{U}_\alpha) + \mathbf{S}_{M,\alpha} + \mathbf{M}_\alpha \quad (3.5)$$

where

- $\mathbf{S}_{M\alpha}$ are momentum source terms.
- $\mathbf{M}_\alpha$ are terms that represent interfacial forces acting on phase α due to the presence of other phases.
- $\Gamma^+_{\alpha\beta} \mathbf{U}_\beta - \Gamma^+_{\beta\alpha} \mathbf{U}_\alpha$ represent momentum transfer due to interphase mass transfer.

In the isothermal crystallizer the system is at steady state, and there is no phase change, so that equation (3.5) becomes

$$\nabla \bullet (r_\alpha \rho_\alpha \mathbf{U}_\alpha \mathbf{U}_\alpha) = -r_\alpha \nabla p_\alpha + r_\alpha \rho_\alpha \mathbf{g} + \nabla \bullet r_\alpha \mu_\alpha \left(\nabla \mathbf{U}_\alpha + (\nabla \mathbf{U}_\alpha)^T\right) + \mathbf{S}_{M,\alpha} + \mathbf{M}_\alpha \quad (3.6)$$

The momentum equation of each phase can be written as shown below:
For the vapor phase:

$$\nabla \bullet (r_d \rho_d \mathbf{U}_d \mathbf{U}_d) = -r_d \nabla p_d + r_d \rho_d \mathbf{g} + \nabla \bullet r_d \mu_d \left(\nabla \mathbf{U}_d + (\nabla \mathbf{U}_d)^T\right) + \mathbf{S}_{M,d} + \mathbf{M}_d \quad (3.7)$$

For the liquid phase:

$$\nabla \bullet (r_c \rho_c \mathbf{U}_c \mathbf{U}_c) = -r_c \nabla p_c + r_c \rho_c \mathbf{g} + \nabla \bullet r_c \mu_c \left(\nabla \mathbf{U}_c + (\nabla \mathbf{U}_c)^T\right) + \mathbf{S}_{M,c} + \mathbf{M}_c \quad (3.8)$$

3.2.3 The volume conservation equation

The volume conservation equation is a constraint that the sum of all the phase volume fractions is equal to one:

$$\sum_{\alpha=1}^{N_p=2} r_\alpha = 1 \quad (3.9)$$

where N_p is the number of phases, so that in this work

$$r_d + r_c = 1 \tag{3.10}$$

3.2.4 The pressure constraint

Both phases present in the system have the same pressure field, so that:

$$p_d = p_c \tag{3.11}$$

3.2.5 Momentum sources

Sources are additional terms which may be added to balance equations to model particular physical or chemical processes which are not included in the general CFD code. In this work, in the DTB modeling, there is a volume defined by a subdomain which represents the impeller. This contains a momentum source in the vertical (y-) direction only.

In the ANSYS CFX program, the user must specify a momentum source value per unit volume of the subdomain, and in a specified direction. A source can be specified for the y-direction as follows:

$$\mathbf{S}_{M,y} = S_{spec,y}\mathbf{j} \tag{3.12}$$

where the $S_{spec,y}$ is the specified momentum component, as shown below:

$$S_{spec,y} = \frac{F_{net,y}}{V} = \frac{P_{net,y}}{U_{net,y}V} \tag{3.13}$$

where P is the power. This momentum source has dimensions of $ML^{-2}T^{-2}$ (e.g. $kg/m^2/s^2$). Considering Figure 3.1, the relationship between force and fluid velocity can be written as:

$$F_{net,y} = \rho A U^2 \tag{3.14}$$

where V and A respectively represent the volume of subdomain and cross-sectional area normal to the flow. The momentum source of each phase can be specified as written below

For the vapor phase:

$$\mathbf{S}_{M,d} = \mathbf{S}_{M,dy} = S_{specy,d}\mathbf{j} \tag{3.15}$$

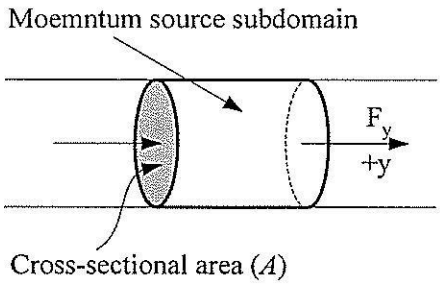

Fig. 3.1 Momentum source subdomain.

For the liquid phase:

$$\mathbf{S}_{M,c} = \mathbf{S}_{M,cy} = S_{specy,c}\mathbf{j} \tag{3.16}$$

3.2.6 The interphase momentum transfer model

Interphase momentum transfer, $\mathbf{M}_\alpha$, occurs due to interfacial forces acting on phases resulting from interaction with other phases. The total force on phase α due to interaction with another phase is given by:

$$\mathbf{M}_\alpha = \sum_{\beta \neq \alpha} \mathbf{M}_{\alpha\beta} \tag{3.17}$$

Interfacial forces between two phases are equal and opposite, so that the net interfacial force sums to zero:

$$\left(\mathbf{M}_{\alpha\beta} = -\mathbf{M}_{\beta\alpha}\right) \Rightarrow \sum_{\alpha} \mathbf{M}_\alpha = 0 \tag{3.18}$$

The interfacial force acting between two phases may result from several independent mechanisms as shown in equation (3.19):

$$\mathbf{M}_{\alpha\beta} = \mathbf{M}_{\alpha\beta}^{D} + \mathbf{M}_{\alpha\beta}^{L} + \mathbf{M}_{\alpha\beta}^{LUB} + \mathbf{M}_{\alpha\beta}^{VM} + \mathbf{M}_{\alpha\beta}^{TD} + \mathbf{M}_{S} + \ldots \tag{3.19}$$

The forces in the equation above represent the interphase drag force, lift force, wall lubrication force, virtual mass force, turbulence dispersion force, and solid pressure force. In this work, the tank diameter (or draft tube diameter in the case of the DTB crystallizer) is not comparable to the diameter of the bubble (which is a small diameter) so the lift force can be neglected. The flow is the mostly axial flow (parallel with the wall) so the wall lubrication force can be neglected. The system is modeled as steady state so the virtual mass force can be neglected. Since there are only small amounts of solids in the system the solid dispersion force can be neglected. This indicates that the interphase drag and turbulence dispersion force only need to be considered in this work. Equation (3.19) becomes

$$\mathbf{M}_{\alpha\beta} = \mathbf{M}_{\alpha\beta}^{D} + \mathbf{M}_{\alpha\beta}^{TD} \tag{3.20}$$

In the particle drag model, the calculation of the interphase drag performed by finding the drag exerted on a body immersed in a moving fluid. The drag force arises from two mechanisms; the first is the skin friction due to the viscous surface shear stress, and the second is the form drag due to the pressure distribution around the body (Maqableh, Simmons, Hibberd, Power, and Young, 2003). The total drag force is expressed in terms of a dimensionless drag coefficient:

$$C_D = \frac{D}{\frac{1}{2}\rho_\alpha (U_\alpha - U_\beta)^2 A} \tag{3.21}$$

D is the magnitude of the drag force, $(U_\alpha - U_\beta)$ is the difference between the speed of the two phases, and A is area of the body projected in the flow direction. The drag exerted by a single item of dispersed phase onto the continuous phase is given by equation (3.22):

$$\mathbf{D}_P = \frac{1}{2} C_D \rho_c A_d |\mathbf{U}_d - \mathbf{U}_c| (\mathbf{U}_d - \mathbf{U}_c) \tag{3.22}$$

It is assumed that the bubbles in the crystallizer are spherical. For spherical bubbles, the area of a single bubble projected in the flow direction, and the volume of a single bubble, are given by: $A_p = \frac{\pi d^2}{4}$ and $V_p = \frac{\pi d^3}{6}$ where d is the mean diameter. The number of bubbles per unit volume, n_p, is given by:

$$n_p = \frac{r_d}{V_p} = \frac{6 r_d}{\pi d^3} \tag{3.23}$$

The total drag exerted by the dispersed phase on the continuous phase per unit volume is:

$$\mathbf{M}_{cd}^D = n_p \mathbf{D}_p = \mathbf{D}_{cd} = \frac{3}{4} \frac{C_D}{d} r_d \rho_c |\mathbf{U}_d - \mathbf{U}_c| (\mathbf{U}_d - \mathbf{U}_c) \tag{3.24}$$

or interface drag term ($c_{cd}^{(d)}$), the total drag is given by:

$$\mathbf{M}_{cd}^D = \mathbf{D}_{cd} = c_{cd}^{(d)} (\mathbf{U}_d - \mathbf{U}_c) \tag{3.25}$$

The interface drag term $c_{cd}^{(d)}$ is thus defined as:

$$c_{cd}^{(d)} = \frac{3}{4} \frac{C_D}{d} r_d \rho_c |\mathbf{U}_d - \mathbf{U}_c| \tag{3.26}$$

Empirical correlations are available for the drag coefficient, C_D, which generally decreases monotonically with increasing Reynolds number (Maqableh *et al.*, 2003).

At sufficiently small particle Reynolds numbers (the viscous regime), fluid particles behave in the same manner as solid spherical particles. Hence the drag coefficient is well approximated by the Schiller and Naumann (1933) correlation shown in equation (3.27):

$$C_D = \frac{24}{\mathrm{Re}}\left(1 + 0.15\,\mathrm{Re}^{0.687}\right) \tag{3.27}$$

At larger particle Reynolds numbers, the so-called inertial or distorted particle regime, the effect of surface tension becomes significant. At moderate Re, fluid particles become approximately ellipsoidal in shape, and at very high Re, spherical cap shaped. One of the correlations used in this regime is that of Ishii and Zuber (1979):

$$C_D(ellipse) = \frac{2}{3}E_0^{1/2} \tag{3.28}$$

ANSYS CFX automatically takes into account the spherical particle and spherical cap limits by setting the drag coefficients as following:

$$C_D = \max\left[C_D(sphere), C_D(dist)\right] \tag{3.29}$$

where

$$C_D(dist) = \min\left[C_D(ellipse), C_D(cap)\right] \tag{3.30}$$

$$C_D(sphere) = \max\left[\frac{24}{\mathrm{Re}}\left(1 + 0.15\,\mathrm{Re}^{0.687}\right), 0.44\right] \tag{3.31}$$

$$C_D(cap) = \frac{8}{3} \tag{3.32}$$

Note that $C_D(cap)$ is the drag coefficient in the spherical cap regime. $\mathrm{Re}_{cd} = \dfrac{\rho_c |U_d - U_c| d}{\mu_c}$. E_0 is the *Eotvos number*, which measures the ratio between gravitational and surface tension forces:

$$E_0 = \frac{g\Delta\rho d_p^2}{\sigma} \tag{3.33}$$

where σ is the surface tension coefficient.

For the turbulent dispersion force, $\mathbf{M}_{cd}^{TD}$ is given by the function of Lopez de Bertodano (1991), as shown below:

$$\mathbf{M}_{cd}^{TD} = -\mathbf{M}_{cd}^{TD} = -C_{TD}\rho_c k_c \nabla r_c \tag{3.34}$$

C_{TD} values of 0.1-0.5 were used in this work, since the bubble diameter is in the order of a few millimeters.

3.2.7 Turbulence modeling

Turbulence models seek to solve a modified set of transport equations by the introduction of averaged and fluctuating components of the velocity. A velocity vector $\mathbf{U}$ may be divided into an average component, $\overline{\mathbf{U}}$, and a time varying component, $\mathbf{u}$.

$$\mathbf{U} = \overline{\mathbf{U}} + \mathbf{u} \tag{3.35}$$

The averaged component is given by a time average of the velocity:

$$\overline{\mathbf{U}} = \frac{1}{\Delta t}\int_{t}^{t+\Delta t} \mathbf{U} dt \tag{3.36}$$

where dt is a time scale that is large relative to the turbulent fluctuations, but small relative to the time scale to which the equations are solved. Substituting the time averaged quantities into the original transport equations (equations 3.3, 3.4, 3.7, and 3.8) results in the Reynolds-averaged equations given below. Note that the continuity equations (equations 3.3 and 3.4) do not need to be altered.

The momentum equation for vapor phase is:

$$\nabla \bullet (r_d \rho_d \mathbf{U}_d \mathbf{U}_d) = -r_d \nabla p_d + r_d \rho_d \mathbf{g} + \nabla \bullet r_d \left[\left(\mu_d \left(\nabla \mathbf{U}_d + (\nabla \mathbf{U}_d)^T \right) \right) - \rho_d \overline{\mathbf{u}_d \mathbf{u}_d} \right] + \mathbf{S}_{M,d} + \mathbf{M}_d \tag{3.37}$$

The momentum equation for liquid phase is:

$$\nabla \bullet (r_c \rho_c \mathbf{U}_c \mathbf{U}_c) = -r_c \nabla p_c + r_c \rho_c \mathbf{g} + \nabla \bullet r_c \left[\left(\mu_c \left(\nabla \mathbf{U}_c + (\nabla \mathbf{U}_c)^T \right) \right) - \rho_c \overline{\mathbf{u}_c \mathbf{u}_c} \right] + \mathbf{S}_{M,c} + \mathbf{M}_c \quad (3.38)$$

where $-\rho_d \overline{\mathbf{u}_d \mathbf{u}_d}$ and $-\rho_c \overline{\mathbf{u}_c \mathbf{u}_c}$ are the Reynolds stresses for vapor and liquid phase, respectively.

In inhomogeneous multiphase flow, bulk turbulence equations are solved which are the same as the single phase equations; this means that a single turbulence field is solved using a single turbulence model. In this work, the turbulence was treated using the $k-\varepsilon$ model where both phases share the same values for k and ε (Micale and Montante, 1999). In this model, the Reynolds stresses is given (Chung, 2002)

$$-\rho \overline{\mathbf{u}\mathbf{u}} = -\frac{2}{3} \rho k \delta + \mu_t \left(\nabla \mathbf{U} + (\nabla \mathbf{U})^T \right) \quad (3.39)$$

where μ_t is the eddy viscosity or turbulent viscosity. Equations (3.37) and (3.38) become

$$\nabla \bullet (r_d \rho_d \mathbf{U}_d \mathbf{U}_d) = -r_d \nabla p'_d + r_d \rho_d \mathbf{g} + \nabla \bullet r_d \mu_{eff,d} \left(\nabla \mathbf{U}_d + (\nabla \mathbf{U}_d)^T \right) + \mathbf{S}_{M,d} + \mathbf{M}_d \quad (3.40)$$

and

$$\nabla \bullet (r_c \rho_c \mathbf{U}_c \mathbf{U}_c) = -r_c \nabla p'_c + r_c \rho_c \mathbf{g} + \nabla \bullet r_c \mu_{eff,c} \left(\nabla \mathbf{U}_c + (\nabla \mathbf{U}_c)^T \right) + \mathbf{S}_{M,c} + \mathbf{M}_c \quad (3.41)$$

μ_{eff} is the effective viscosity accounting for turbulence, and is given by

$$\mu_{eff,c} = \mu_c + \mu_t = \mu_c + \mu_{tc} + \mu_{tb} \quad (3.42)$$

The turbulent viscosity of liquid phase is based on the $k-\varepsilon$ model and formulated as follows:

$$\mu_{tc} = C_\mu \rho_c \frac{k^2}{\varepsilon} \quad (3.43)$$

where $C_\mu = 0.09$. The term μ_{tb} is particle induced eddy viscosity. Several models have been proposed for this viscosity. In this work the model proposed by Sato and Sekoguchi (1975) was used:

$$\mu_{tb} = C_{\mu b}\rho_c r_d d|U_d - U_c| \tag{3.44}$$

with $C_{\mu b}$ a model constant which equals 0.6 (Deen, Solberg, and Hjertager, 2002). The effective vapor viscosity can be estimated from the effective liquid viscosity

$$\mu_{eff,d} = \frac{\rho_d}{\rho_c}\mu_{eff,c} \tag{3.45}$$

as was proposed by Jakobsen, Sannaes, Grevskott, and Svendsen (1997). The term p' is the modified pressure given by

$$p'_d = p_d + \frac{2}{3}\rho_d k \text{ and } p'_c = p_c + \frac{2}{3}\rho_c k \tag{3.46}$$

The values of k and ε come directly from the differential transport equation for the turbulent kinetic energy and turbulent dissipation rate, as shown below:

The transport equation of the turbulent kinetic energy, k is:

$$\frac{\partial(\rho k)}{\partial t} + \nabla\bullet(\rho\mathbf{U}k) = \nabla\bullet\left[\left(\mu + \frac{\mu_t}{\sigma_k}\right)\nabla k\right] + P_k - \rho\varepsilon \tag{3.47}$$

where $\sigma_k = 1.0$, $\rho = r_d\rho_d + r_c\rho_c$, $\mu = r_d\mu_d + r_c\mu_c$, $\mathbf{U} = (r_d\rho_d U_d + r_c\rho_c U_c)/\rho$, k is the turbulent kinetic energy, is defined as the variance of the fluctuation in velocity, and has dimensions of L^2T^{-2} (e.g. m^2/s^2). ε is the turbulent eddy dissipation (the rate at which the velocity fluctuations dissipate) and has dimensions of L^2T^{-3} (e.g. m^2/s^3). The term P_k is the turbulence production due to viscous and buoyancy forces, which is modeled using:

$$P_k = \mu_t \nabla \mathbf{U} \bullet \left(\nabla \mathbf{U} + (\nabla \mathbf{U})^T\right) + P_{kb} \tag{3.48}$$

When a full buoyancy model is used, the buoyancy production term P_{kb} is given by:

$$P_{kb} = -\frac{\mu_t}{\rho \mathrm{Pr}_t} \mathbf{g} \bullet \nabla \rho \tag{3.49}$$

where Pr_t is the Turbulent Prandtl number, defined as: $c_p \mu / \lambda_t$. μ, c_p and λ_t represent the viscosity, constant pressure specific heat capacity, and thermal conductivity for the liquid phase.

The transport equation of the dissipation rate of the turbulence kinetic energy, ε is:

$$\frac{\partial(\rho\varepsilon)}{\partial t} + \nabla \bullet (\rho \mathbf{U} \varepsilon) = \nabla \bullet \left[\left(\mu + \frac{\mu_t}{\sigma_\varepsilon}\right) \nabla \varepsilon\right] + \frac{\varepsilon}{k}\left(C_{\varepsilon 1} P_k - C_{\varepsilon 2} \rho \varepsilon\right) \tag{3.50}$$

where $\sigma_\varepsilon = 1.3$, $C_{\varepsilon 1} = 1.44$, and $C_{\varepsilon 2} = 1.92$.

In the ANSYS CFX program, the production term is also included in the ε equation if P_{kb} is positive:

$$P_{\varepsilon b} = C_3 \bullet \max(0, P_{kb}) \tag{3.51}$$

If the directional option in the program is used, then $P_{\varepsilon b}$ is modified by a factor accounting for the angle α between the velocity and the gravity vector:

$$P_{\varepsilon b} = C_3 \bullet \max(0, P_{kb}) \bullet \sin\alpha \tag{3.52}$$

The model constants assumed by default are $\mathrm{Sc}_t = 1$, and $C_3 = 1$.

Particular models are required for flow near a zero-slip wall, because here there are strong gradients in the variables. The near-wall region can be subdivided into two layers.

In the region very close to the wall, the layer is called the "laminar (viscous) sublayer", where the molecular viscosity plays a dominant role in momentum and heat transfer. Further away from the wall, in the "logarithmic layer", turbulence dominates the mixing process. Moreover, between the viscous sublayer and logarithmic layer, there is the "buffer layer", where the effect of molecular viscosity and turbulence are of near equal importance. Figure 3.2 shows these subdivisions of near-wall region.

A logarithmic profile is a reasonable assumption for the velocity distribution near the wall. The assumption provides a method to compute the fluid shear stress as a function of the velocity at a given distance from the wall. This is known as a "wall function".

In this work the scalable wall function is used to model the flow near the wall; this function was developed by ANSYS CFX.

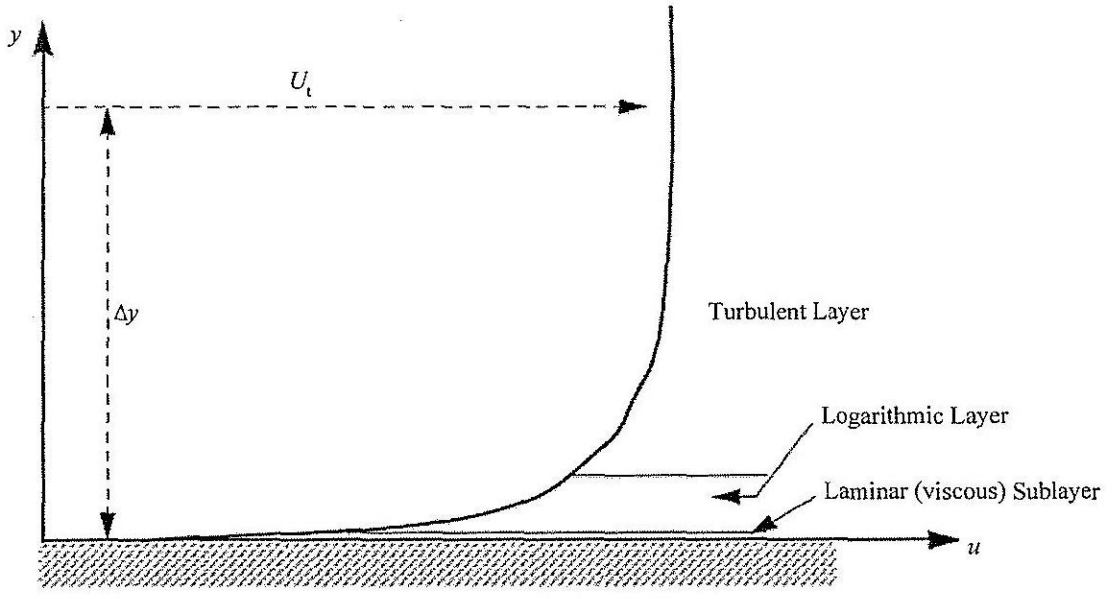

Fig. 3.2 Flow regions for turbulent flow near a wall (ANSYS Canada Ltd., 2005).

The logarithmic relation for the near wall velocity is given by:

$$u^+ = C_\mu^{1/4} k^{1/2} \tag{3.53}$$

The friction velocity is given by:

$$u_\tau = \frac{U_t}{\frac{1}{\kappa}\ln(y^+) + C} \tag{3.54}$$

The absolute value of the wall shear stress is then obtained from:

$$\tau_{\omega} = \rho u^{+} u_{\tau} \tag{3.55}$$

U_t is the known velocity tangent to the wall at a distance of Δy, $\kappa = 0.41$ (the von Karman constant), $C = 5.2$, and $y^{+} = (\rho u^{+} \Delta y)/\mu$. y^{+} is the dimensionless distance from the wall. The minimum y^{+} is 11.06.

3.2.8 Energy equation

The energy equation is used in non-isothermal simulations. The full form of the energy equation is given below

$$\begin{aligned} &\frac{\partial}{\partial t}(r_\alpha \rho_\alpha h_{tot,\alpha}) - r_\alpha \frac{\partial p}{\partial t} + \nabla \bullet \left(r_\alpha \rho_\alpha \mathbf{U}_\alpha h_{tot,\alpha} - r_\alpha \lambda_\alpha \nabla T_\alpha\right) \\ &-\nabla \bullet \left(r_\alpha \mu_\alpha \left[\nabla \mathbf{U}_\alpha + (\nabla \mathbf{U}_\alpha)^T\right] \mathbf{U}_\alpha\right) = \sum_{\beta=1}^{N_p} \left(\Gamma^{+}_{\alpha\beta} h_{tot,\beta} - \Gamma^{+}_{\beta\alpha} h_{tot,\alpha}\right) \\ &\qquad + \rho_\alpha r_\alpha (\mathbf{U}_\alpha \bullet \mathbf{g}) + S_{E,\alpha} + Q_\alpha \end{aligned} \tag{3.56}$$

For a system at steady state, Eq. (3.56) becomes

$$\begin{aligned} &\nabla \bullet \left(r_\alpha \rho_\alpha \mathbf{U}_\alpha h_{tot,\alpha} - r_\alpha \lambda_\alpha \nabla T_\alpha\right) - \nabla \bullet \left(r_\alpha \mu_\alpha \left[\nabla \mathbf{U}_\alpha + (\nabla \mathbf{U}_\alpha)^T\right] \mathbf{U}_\alpha\right) \\ &\qquad = \sum_{\beta=1}^{N_p} \left(\Gamma^{+}_{\alpha\beta} h_{tot,\beta} - \Gamma^{+}_{\beta\alpha} h_{tot,\alpha}\right) + \rho_\alpha r_\alpha (\mathbf{U}_\alpha \bullet \mathbf{g}) + S_{E,\alpha} + Q_\alpha \end{aligned} \tag{3.57}$$

where

- $H_{tot,\alpha}$, T_α, λ_α are the total static enthalpy, the temperature, and the thermal conductivity of the phase α.
- S_E is an external heat source.
- Q_α is the amount of interphase heat transfer into the phase α across the interface with phase β.
- $(\Gamma^{+}_{\alpha\beta} h_{tot,\beta} - \Gamma^{+}_{\beta\alpha} h_{tot,\alpha})$ represents convected heat transfer via interphase mass transfer.

The energy equation of each phase can be written as below

For the vapor phase:

$$\nabla \bullet \left(r_d \rho_d \mathbf{U}_d h_{tot,d} - r_d \lambda_d \nabla T_d\right) - \nabla \bullet \left(r_d \mu_d \left[\nabla \mathbf{U}_d + (\nabla \mathbf{U}_d)^T\right] \mathbf{U}_d\right) = \left(\Gamma_{dc}^{+} h_{tot,c} - \Gamma_{cd}^{+} h_{tot,d}\right) + \rho_d r_d (\mathbf{U}_d \bullet \mathbf{g}) + S_{E,d} + Q_d \tag{3.58}$$

For the liquid phase:

$$\nabla \bullet \left(r_c \rho_c \mathbf{U}_c h_{tot,c} - r_c \lambda_c \nabla T_c\right) - \nabla \bullet \left(r_c \mu_c \left[\nabla \mathbf{U}_c + (\nabla \mathbf{U}_c)^T\right] \mathbf{U}_c\right) = \left(\Gamma_{cd}^{+} h_{tot,d} - \Gamma_{dc}^{+} h_{tot,c}\right) + \rho_c r_c (\mathbf{U}_c \bullet \mathbf{g}) + S_{E,c} + Q_c \tag{3.59}$$

3.2.9 The inhomogeneous interphase heat transfer model

Interphase heat transfer occurs due to non-equilibrium (w.r.t. heat transfer) across phase interfaces. The total heat transferred per unit volume to a phase α due to the interaction with another phase (β) is denoted Q_α, and is given by:

$$Q_\alpha = \sum_{\beta \neq \alpha} Q_{\alpha\beta} \tag{3.60}$$

where

$$Q_{\alpha\beta} = -Q_{\beta\alpha} \Rightarrow \sum_{\alpha} Q_\alpha = 0 \tag{3.61}$$

In this work, the Two Resistance model for interphase heat transfer was used with the thermal phase change model. The two-resistance model considers separate heat transfer processes for both sides of the phase interface, by defining two heat transfer coefficients on each phase interface.

Defining the sensible heat flux to the vapor phase from the interface as:

$$q_d = h_d (T_s - T_d) \tag{3.62}$$

and the sensible heat flux to the liquid phase from the interface as:

$$q_c = h_c (T_s - T_c) \tag{3.63}$$

where h_d and h_c are the vapor phase and liquid phase heat transfer coefficients respectively. T_s is the interface temperature, and is assumed to be equal for both phases. The surface temperature is equal to the saturation temperature, $T_s = T_{sat}$. The Nusselt number is defined as $Nu_\alpha = \frac{h_\alpha d_{\alpha\beta}}{\lambda_\alpha}$ and is different for the two fluids. In this work the Hughmark (1967) correlation is used to find the heat transfer coefficient of a continuous phase and thus the Nusselt number is defined as:

$$Nu_c = \begin{cases} 2 + 0.6\,\mathrm{Re}_d^{0.5}\,\mathrm{Pr}_c^{0.33} & 0 \le \mathrm{Re}_d < 776.06 \quad 0 \le \mathrm{Pr}_c < 250 \\ 2 + 0.27\,\mathrm{Re}_d^{0.62}\,\mathrm{Pr}_c^{0.33} & 776.06 \le \mathrm{Re}_d \quad 0 \le \mathrm{Pr}_c < 250 \end{cases} \tag{3.64}$$

The Prandtl number is defined by $\mathrm{Pr}_c = \frac{\mu_c C_{Pc}}{\lambda_c}$. In the disperse phase the Zero Resistance model, which is equivalent to an infinite fluid specific heat transfer coefficient, $h_c \to \infty$, was used. The effect of this is to force the interfacial temperature (from the overall heat balance $q_\alpha + q_\beta = 0$, so we get $T_s = \frac{h_c T_c + h_d T_d}{h_c + h_d}$) to be the same as the dispersed phase temperature, $T_s = T_c$, so that the equation (3.68) becomes

$$q_d = h_d (T_c - T_d) \tag{3.65}$$

and equation (3.69) becomes

$$q_c = 0 \tag{3.66}$$

More detail of the theory used in this section is in the 'thermal phase change model' section of the CFX-10.0 Manual.

3.2.10 The interphase mass transfer model

Interphase mass transfer occurs when a chemical species is carried from one phase into another phase. Γ_α is the mass source per unit volume into phase α due to interphase mass transfer. This is given as

$$\Gamma_{\alpha} = \sum_{\beta=1}^{N_p=2} \Gamma_{\alpha\beta} \tag{3.67}$$

$\Gamma_{\alpha\beta}$ is the mass flow rate per unit volume from phase β to phase α. Therefore

$$\Gamma_{\alpha\beta} = -\Gamma_{\beta\alpha} \Rightarrow \sum_{\alpha=}^{N_p=2} \Gamma_{\alpha} = 0 \tag{3.68}$$

It is convenient to express $\Gamma_{\alpha\beta}$ in the direction of mass transfer as follows:

$$\Gamma_{\alpha\beta} = \Gamma^{+}_{\alpha\beta} - \Gamma^{+}_{\beta\alpha} \tag{3.69}$$

The term $\Gamma^{+}_{\alpha\beta} > 0$ represents a positive flow rate per unit volume from phase β to phase α.

In mass transfer across a phase interface, the mass sources are defined relative to the density between the phases.

$$\Gamma_{\alpha\beta} = \dot{m}_{\alpha\beta} A_{\alpha\beta} \tag{3.70}$$

where $\dot{m}_{\alpha\beta}$ is the mass flow rate per unit volume interfacial area from phase β to phase α, and $A_{\alpha\beta}$ is the interfacial area per unit volume between the phases. It is assumed that the disperse phase is a spherical bubble, $A_{\alpha\beta} = \dfrac{6r_{\beta}}{d_{\beta}}$.

The default form of the secondary source terms for a transported variable ϕ_{α} is:

$$S_{m\alpha} = \sum_{\beta=1}^{N_p=2} \left(\Gamma^{+}_{\alpha\beta} \phi_{\beta} - \Gamma^{+}_{\beta\alpha} \phi_{\alpha} \right) \tag{3.71}$$

This represents the mass transfer from phase β into phase α which carries the bulk conserved quantity ϕ_{β} into phase α. This is an upwind formulation, as the upwind value is carried out from the outgoing phase, and into the incoming phase. This default formulation is modified in certain circumstances, in order to take account of discontinuities in the

transported variable at the phase interface, for this work, velocity and enthalpy are considered.

3.2.11 The thermal phase change model

The thermal phase change model models the rate of phase change due to interphase heat transfer in the interior of the flow. In this work, the saturation temperature is constant and the vapor phase temperature should remain fixed at the saturation conditions. Therefore the vapor phase is assumed isothermal, with a reference temperature set equal to the vapor saturation temperature.

In the case of mass transfer, the interphase mass transfer is determined from the total heat balance, as follows:

The total heat flux to liquid phase from the interface is

$$Q_c = q_c + \dot{m}_{cd} H_{cs} \tag{3.72}$$

The total heat flux to vapor phase from the interface is

$$Q_d = q_d - \dot{m}_{cd} H_{ds} \tag{3.73}$$

Substitution of equation (3.72) into (3.78), gives

$$Q_c = \dot{m}_{cd} H_{cs} \tag{3.74}$$

where H_{cs} and H_{ds} represent interfacial values of the enthalpy of the liquid and vapor respectively, which are carried into and out of the phases due to phase change.

The total heat balance $Q_c + Q_d = 0$ now determines the interphase mass flux:

$$\dot{m}_{cd} = \frac{q_d}{H_{ds} - H_{cs}} \tag{3.75}$$

The discontinuity in static enthalpy due to the latent heat between the two phases must be taken into account by the secondary heat flux term, which is achieved using a modification

of the upwind formulation (equation 3.76). In this formulation, the bulk fluid enthalpy is carried out of the outgoing phase, as in the default upwind formulation. However, the saturation enthalpy is carried into the incoming phase. Thus:

$$\begin{aligned} \dot{m}_{cd} > 0 &\Rightarrow H_{cs} = H_{csat},\ H_{ds} = H_d \\ \dot{m}_{cd} < 0 &\Rightarrow H_{cs} = H_c,\ H_{ds} = H_{dsat} \end{aligned} \tag{3.76}$$

This leads to a formulation which is stable both physically and numerically. It implies that the denominator (equation 3.81) is non-zero, being either greater than or equal to the latent heat transfer:

$$L = H_{dsat} - H_{csat} \tag{3.77}$$

3.2.12 Turbulence modeling in non-isothermal simulations

The momentum equations are considered the same way as for the isothermal simulation. So that the equations

$$\begin{aligned} \nabla \bullet (r_d \rho_d \mathbf{U}_d \mathbf{U}_d) = -r_d \nabla p'_d + r_d \rho_d \mathbf{g} + \nabla \bullet r_d \mu_{eff,d} \left(\nabla \mathbf{U}_d + (\nabla \mathbf{U}_d)^T\right) \\ + \left(\Gamma^+_{dc} \mathbf{U}_c - \Gamma^+_{cd} \mathbf{U}_d\right) + \mathbf{S}_{M,d} + \mathbf{M}_d \end{aligned} \tag{3.78}$$

and

$$\begin{aligned} \nabla \bullet (r_c \rho_c \mathbf{U}_c \mathbf{U}_c) = -r_c \nabla p'_c + r_c \rho_c \mathbf{g} + \nabla \bullet r_c \mu_{eff,c} \left(\nabla \mathbf{U}_c + (\nabla \mathbf{U}_c)^T\right) \\ + \left(\Gamma^+_{cd} \mathbf{U}_d - \Gamma^+_{dc} \mathbf{U}_c\right) + \mathbf{S}_{M,c} + \mathbf{M}_c \end{aligned} \tag{3.79}$$

for the vapor and liquid phase, respectively, are used. For the liquid phase, the $k-\varepsilon$ turbulent model was employed. Most equations in this model are the same as the isothermal part, except the velocity and other transport properties in the k and ε equations are the liquid property. For the vapor phase, the Dispersed Phase Zero Equation model was employed. In this model, $\mu_{td} = \frac{\rho_d}{\rho_c} \frac{\mu_{tc}}{\sigma}$ so that the effective vapor viscosity is

$$\mu_{eff,d} = \mu_d + \frac{\rho_d}{\rho_c}\frac{\mu_{tc}}{\sigma} \tag{3.80}$$

The parameter σ is a turbulent Prandtl number relating the dispersed phase kinetic eddy viscosity to the continuous phase kinetic eddy viscosity $(\sigma = \nu_{td}\nu_{tc})$. In this work the default value of 1.0 is used.

Convective transport due to turbulent velocity fluctuations will act to increase mixing compared to that caused by thermal fluctuations at the molecular level. At high Reynolds numbers, the mean free path of thermal fluctuations is smaller than the turbulent velocity fluctuations occur over a length scale, so that the turbulent fluxes are much larger than the molecular fluxes (this means that the term of $\nabla \bullet \left(r_\alpha \mu_\alpha \left(\nabla U_\alpha + (\nabla U_\alpha)^T\right) U_\alpha\right)$ in the energy equation for both phases are canceled). So that the Reynolds-averaged energy equations are:

For the vapor phase:

$$\nabla \bullet \left(r_d \rho_d \mathbf{U}_d h_{tot,d} - r_d \lambda_d \nabla T_d + \rho_d \overline{\mathbf{u}_d h_{tot,d}}\right) = \left(\Gamma^+_{dc} h_{tot,c} - \Gamma^+_{cd} h_{tot,d}\right) + \rho_d r_d (\mathbf{U}_d \bullet \mathbf{g}) + S_{E,d} + Q_d \tag{3.81}$$

For the liquid phase:

$$\nabla \bullet \left(r_c \rho_c \mathbf{U}_c h_{tot,c} - r_c \lambda_c \nabla T_c + \rho_c \overline{\mathbf{u}_c h_{tot,c}}\right) = \left(\Gamma^+_{cd} h_{tot,d} - \Gamma^+_{dc} h_{tot,c}\right) + \rho_c r_c (\mathbf{U}_c \bullet \mathbf{g}) + S_{E,c} + Q_c \tag{3.82}$$

where $-\rho_d \overline{\mathbf{u}_d h_{tot,d}}$ and $-\rho_c \overline{\mathbf{u}_c h_{tot,c}}$ are the Reynolds fluxes of enthalpy for vapor and liquid, respectively. The Reynolds fluxes of enthalpy is given by

$$-\rho \overline{\mathbf{u}h} = \Gamma_t \nabla h \tag{3.83}$$

where Γ_t is the eddy diffusivity and given by $\Gamma_t = \frac{\mu_t}{\mathrm{Pr}_t}$. So the Reynolds averaged energy equations become:

For the vapor phase:

$$\nabla \bullet \left(r_d \rho_d \mathbf{U}_d h_{tot,d} - r_d \lambda_d \nabla T_d + \frac{\mu_t}{\mathrm{Pr}_t} \nabla h_{tot,d} \right) = \left(\Gamma^+_{dc} h_{tot,c} - \Gamma^+_{cd} h_{tot,d} \right) + \rho_d r_d \left(\mathbf{U}_d \bullet \mathbf{g} \right) + S_{E,d} + Q_d \tag{3.84}$$

For the liquid phase:

$$\nabla \bullet \left(r_c \rho_c \mathbf{U}_c h_{tot,c} - r_c \lambda_c \nabla T_c + \frac{\mu_t}{\mathrm{Pr}_t} \nabla h_{tot,c} \right) = \left(\Gamma^+_{cd} h_{tot,d} - \Gamma^+_{dc} h_{tot,c} \right) + \rho_c r_c \left(\mathbf{U}_c \bullet \mathbf{g} \right) + S_{E,c} + Q_c \tag{3.85}$$

The eddy viscosity, μ_t, is related to k and ε, as described previously.

3.2.13 Heat sources

The heat exchanger is represented by a bulk heat source term. This source term, is defined as:

$$S_{E,\alpha} = \frac{\dot{Q}}{V} = \frac{heat\ quantity}{volume\ of\ source} \qquad \left[\frac{\mathrm{Watt}}{\mathrm{m}^3} \right] \tag{3.86}$$

3.3 Conclusions

The complete set of steady state governing equations of fluid flow and heat transfer for Newtonian two-phase flow (Eulerian-Elerian multiphase model) are given. In the isothermal part, the homogeneous $k-\varepsilon$ turbulence model was employed where both phases share the same values for k and ε. And in the non-isothermal part, the $k-\varepsilon$ turbulence model was employed in the liquid phase, and the Dispersed Phase Zero Equation model was employed in the vapor phase. The equations required clearly do not have analytical solutions for the geometry used here, but CFD uses a range of space and

time discretization method in order to enable a numerical solution to be calculated. In the work presented here, the commercial CFD software ANSYS CFX-10.0 with the finite volume method using an unstructured mesh was used to discretize the volume and find the solution of these equations.

Chapter IV

Apparatus and Methods

The aim of this chapter is to describe the apparatus used in this work, the study methods to approach each objective shown in chapter 1, and the simulation methods to obtain the results. The simulation methods will focus on the processes of the ANSYS CFX-10.0 simulation, which are split into five components: geometry creation (ANSYS Workbench 10.0), mesh creation (CFX-Mesh), physical definitions (CFX-Pre), solver (CFX-Solver), and post-processing (CFX-Post).

4.1 Apparatus

In this work, the following apparatus were used:

1. A Pentium IV 3.0GHz processor with 512 MB of RAM and a AMD Athlon$^{(tm)}$ XP 2500+ 1.84 GHz processor with 384 MB of RAM.

2. An operating system of Microsoft Windows XP Professional Version 2002 Service Pack 1.

3. The commercial software ANSYS CFX-10.0, ANSYS Workbench 10.0, Microsoft Office Professional Edition 2003, and Microsoft Visio Professional 2002.

4.2 Study Methods

To achieve each objective of this study, the methods to approach each objective are described below.

4.2.1 Isothermal Simulation of the DTB crystallizer

In this section, the vapor is assumed to form in an external heat exchanger before being fed into the crystallizer. The temperature rise in the crystallizer, which is caused by heat produced by the impeller and heat of crystallization, is not more than 2°C. Therefore, the crystallizer can be assumed to be an isothermal process without significant error. This indicates that the DTB crystallizer with an external heat exchanger can be adequately modeled by an isothermal process in order to reduce the computation time and model complexity.

4.2.1.1 Study into the general characteristics of flow fields and classification of crystals in a DTB crystallizer

It is necessary to understand the general characteristics of the flow fields in a DTB crystallizer before study into the effect of the different operating parameters. The case study number 5 in Table 4.1 is the general case that was selected to achieve this purpose.

4.2.1.2 Study into the effect of the momentum source strength on the flow characteristics and the classification of crystals

A momentum source is used to represent the impeller in order to reduce the computation time and model complexity. This is based on studies of Pericleous and Patel (1987) who showed that this is an effective way to model an impeller in CFD modeling of mixing vessels. Therefore, it is important to study the effect of the momentum source strength, which is equivalent to a study of the effect of impeller speed.

In this study, the flow characteristics and the classification of crystals obtained from different amounts of the momentum source were compared under the same solution inlet flow rate, fines removal flow rate, and product crystals flow rate. The momentum source values are 0, 1000, 4000, 7000, 10000, 15000, 25000, and 30000 $kg/m^2/s^2$, as indicated in case studies 1 to 7 in Table 4.1.

Table 4.1 Cases study for the isothermal simulation.

Case Study Number	Variable (unit)					
	Solution inlet[1]		Total Fines flow[2,3] (kg/s)	Vapor Out flow (kg/s)	Product Out[3] Flow (kg/s)	Momentum source ($kg/m^2/s^2$)
	Liquid Flow (kg/s)	Vapor Flow (kg/s)				
1	1.18602	0.0000649	1.00632	0.0000649	0.1797	0
2	1.18602	0.0000649	1.00632	0.0000649	0.1797	1,000
3	1.18602	0.0000649	1.00632	0.0000649	0.1797	4,000
4	1.18602	0.0000649	1.00632	0.0000649	0.1797	7,000
5	1.18602	0.0000649	1.00632	0.0000649	0.1797	10,000

[1]Solution inlet = Fines + Fresh feed solution.

[2]Fines Removal1 flow = Fines Removal2 flow = Total Fines flow ÷ 2

[3]Fines and Product streams are assumed to have the properties of liquids for convenience.

Table 4.1 (Continued)

Case Study Number	Variable (unit)					
	Solution inlet		Total Fines flow (kg/s)	Vapor Out flow (kg/s)	Product Out Flow (kg/s)	Momentum source ($kg/m^2/s^2$)
	Liquid Flow (kg/s)	Vapor Flow (kg/s)				
6	1.18602	0.0000649	1.00632	0.0000649	0.1797	15,000
7	1.18602	0.0000649	1.00632	0.0000649	0.1797	25,000
8	1.18602	0.0000649	1.00632	0.0000649	0.1797	30,000
9	0.64692	0.0000354	0.46722	0.0000354	0.1797	10,000
10	1.18602	0.0000649	1.00632	0.0000649	0.1797	10,000
11	1.72512	0.0000944	1.54542	0.0000944	0.1797	10,000
12	2.47986	0.0001357	2.30016	0.0001357	0.1797	10,000

Table 4.1 (Continued)

Case Study Number	Variable (unit)					
	Solution inlet		Total Fines flow (kg/s)	Vapor Out flow (kg/s)	Product Out Flow (kg/s)	Momentum source ($kg/m^2/s^2$)
	Liquid Flow (kg/s)	Vapor Flow (kg/s)				
13	3.77370	0.0002065	3.59400	0.0002065	0.1797	10,000
14	1.06622	0.0000583	1.00632	0.0000583	0.0599	10,000
15	1.12612	0.0000616	1.00632	0.0000616	0.1198	10,000
16	1.18602	0.0000649	1.00632	0.0000649	0.1797	10,000
17	1.26988	0.0000695	1.00632	0.0000695	0.26356	10,000
18	1.47354	0.0000806	1.00632	0.0000806	0.46722	10,000

4.2.1.3 Study into the effect of fines removal flow rate to the flow characteristics and the classification of crystals

The fine crystals in the mother liquor are separated out from the crystallizer in an annular zone outside the main body of the crystallizer (the settling zone). In this zone, fines removed from the annulus must flow upward to obtain crystal segregation based on differences in settling velocity. Normally a higher fines removal flow will result in a fines removal cut-size larger than for a lower fines removal flow, because higher flows create larger upflow velocities in the settling zone, and thus larger particle are drawn upwards and removed.

In this study, the flow characteristics and the classification of crystals obtained from different values of the fines removal flow rate were compared under the same solution inlet flow rate, amount of momentum source, and product crystal suspension flow rate. The fines removal flows were varied at 0.4672, 1.0063, 1.5454, 2.3002, and 3.594 kg/s, as shown in case studies 9 to 13 of Table 4.1.

4.2.1.4 Study into the effect of product crystals flow rate to the flow characteristics and the classification of crystals

In this study, the flow characteristics and the classification of crystals obtained from different values of the product crystals flow rate were compared under the same solution inlet flow rate, amount of momentum source, and product crystals flow rate. For a feed solution flow of approximately 1 kg/s, product crystals flows were varied at 0.0599, 0.1198, 0.1797, 0.26356, and 0.46722 kg/s, as shown case studies 14 to 18 of Table 4.1.

4.2.2 Non-isothermal simulation

In this section, the feed solution is heated by an external heat exchanger to a temperature about 1-2 degrees Celsius below the boiling point. The vapor is formed in the crystallizer, due to the temperature rising to the boiling point due to the impeller. For this reason, the area above the liquid surface was not modeled and the liquid surface is considered to be flat and frictionless in order to reduce the model complexity.

4.2.2.1 Study into the general characteristics of the flow fields and classification of product crystals in a DTB crystallizer by non-isothermal CFD simulation

It is necessary to understand the general characteristics of the flow fields in a DTB crystallizer using non-isothermal simulation, and compare the results to the isothermal simulation. This is because some crystallizers use an internal heat exchanger to produce

supersaturation, and therefore boiling takes place inside the crystallizer body. So the case study number 1 in Table 4.2 is the general case that was selected to describe of this purpose.

4.2.2.2 Study into the effect of the momentum source strength on the flow characteristics and classification of crystals

The flow characteristics and classification of product crystals obtained from crystallizers with varying momentum source strengths were compared under the same solution inlet flow rate, amount of heat source, fines removal flow rate, and product crystals flow rate.

The details in each case study of these studies are shown in Table 4.2.

Table 4.2 Case studies for non-isothermal simulation.

Case Study Number	Liquid Solution inlet (kg/s)	Product out flow (kg/s)	Momentum source ($kg/m^2/s^2$)	Heat source (W/m^3)
19	1.18602	0.1797	10,000	
20	1.18602	0.1797	15,000	
21	1.18602	0.1797	25,000	
22	1.18602	0.1797	30,000	

4.3 Simulation Methods

To obtain the results of each study listed in Tables 4.1 and 4.2, simulation by ANSYS CFX-10.0 was conducted to determine flow fields (and temperature profiles for non-isothermal runs) in the DTB crystallizer.

The processes of the ANSYS CFX-10.0 simulation are split into five components. These are geometry creation, mesh creation, physical definitions (physics of the problem, physical parameter constants, among other considerations), equation solver, and post-processing. Each component is described below:

4.3.1 Geometry

In this work the DTB crystallizer geometry was created by the program DesignModeler in ANSYS Workbench v.10.0.

The crystallizer used for numerical simulation in this work is a pilot scale 1050 l DTB crystallizer. The crystallizer dimensions and 3D geometry are given in Figure 4.1 and 4.2, respectively. The operating parameters and performance of this crystallizer are discussed in chapter 2 (section 2.2.2).

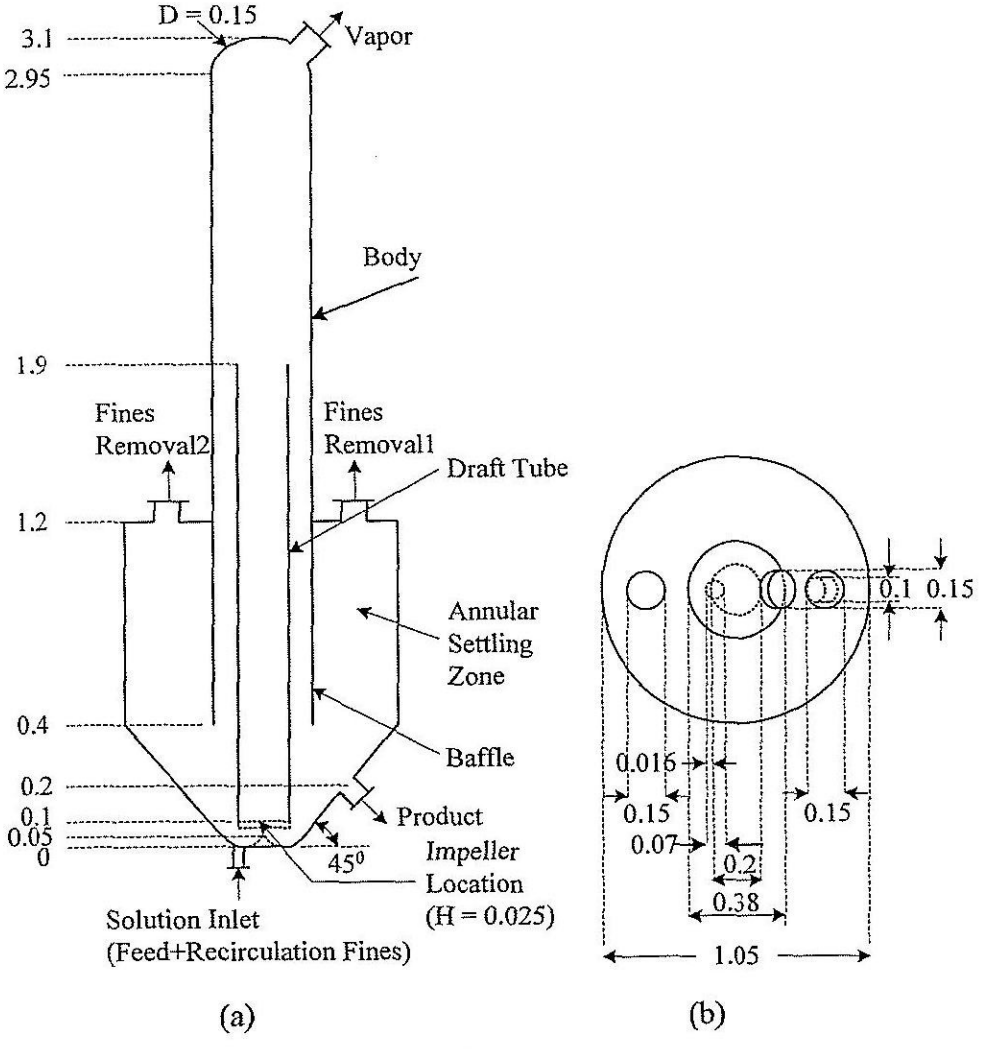

Fig. 4.1 DTB crystallizer geometry and dimensions. Dimensions are given in meters: (a) side view; (b) top view.

For convenience in the simulation, the wall of the solution inlet tube, product outlet tube, fines removal tube, vapor outlet tube, draft tube, baffle, and tank

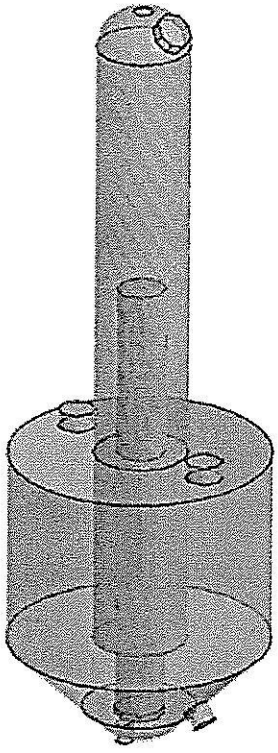

Fig. 4.2 Geometry of the evaporative-DTB crystallizer.

are described using a thin surface material. The impeller (in this crystallizer the impeller is considered to be a turbine of diameter : height 8:1, with a 45° pitched blade) is represented as a momentum source term in the vertical direction (upward flow) only. In the real impeller there are also radial components of the momentum addition, however they are effectively damped out by baffles placed in the normal direction to the tank walls. Since the radial components of the momentum addition are damped out in this design, we have not attempted to model them here to reduce the model complexity. A momentum source term has been added at the base of the draft tube, at the position and size of the true impeller (see Figure 4.1). The heat exchanger is represented as a bulk heat source and the location of this source is shown in Figure 4.1.

4.3.2 Mesh

In this work the mesh was created by the program CFX-Mesh in ANSYS Workbench v.10.0.

The first step in mesh creation is to create composite 2D regions to specify locations in CFX-Mesh and define boundary conditions in CFX-Pre. These regions

include the solution inlet, product outlet, fines removal, vapor outlet, draft tube, baffle, and tank walls (the remaining outside walls) (see Figure 4.3).

The final step before the physics definition is to create the mesh, which was created by the program CFX-Mesh in ANSYS Workbench v.10.0. ANSYS CFX-10.0 uses the finite volume solution technique with an unstructured mesh. Initially the program creates a 2-D mesh on the boundaries of the crystallizer geometry, and then this mesh is extrapolated into the body of the geometry. The volume of the crystallizer tank is broken into a set of discrete subdomains, computational cells, or control volumes using a grid, or mesh. The mesh can contain elements of many shapes and size. The points of intersection of the lines that make up the sides of the elements are referred to as nodes. In CFX-Mesh, 3-D elements are usually tetrahedral (with four sides), prisms (with five sides), pyramids (with five sides), and hexahedra (with six sides).

4.3.2.1 Mesh generation

Generally, the density of cells in a computational mesh needs to be fine enough to capture the flow detail, but not so fine that the overall number of cells in the domain is excessively large, since problems described by large numbers of cells require more time to solve (Paul *et al.*, 2004). Non-uniform meshes of any topology can be used to give higher mesh density in regions where it is needed and to allow for lower mesh densities in other regions.

In this work, the mesh near the solution inlet boundary, product outlet boundary, the region under the draft tube, the region around the draft tube, and the region around the upper edge of draft tube should be refined to have a reasonably fine mesh and allow the solution to capture the flow details (especially, the velocity, since it changes rapidly in these regions). An example of the fine mesh of the above boundaries and regions is shown in Figure 4.4.

After defining and setting the conditions of the mesh and the region where a fine mesh is required, the surface mesh will be generated prior to the volume mesh generation. However, it is often helpful to explicitly generate at least part of the surface mesh before volume meshing, to view it and ensure that the chosen scales and controls will have the desired effect.

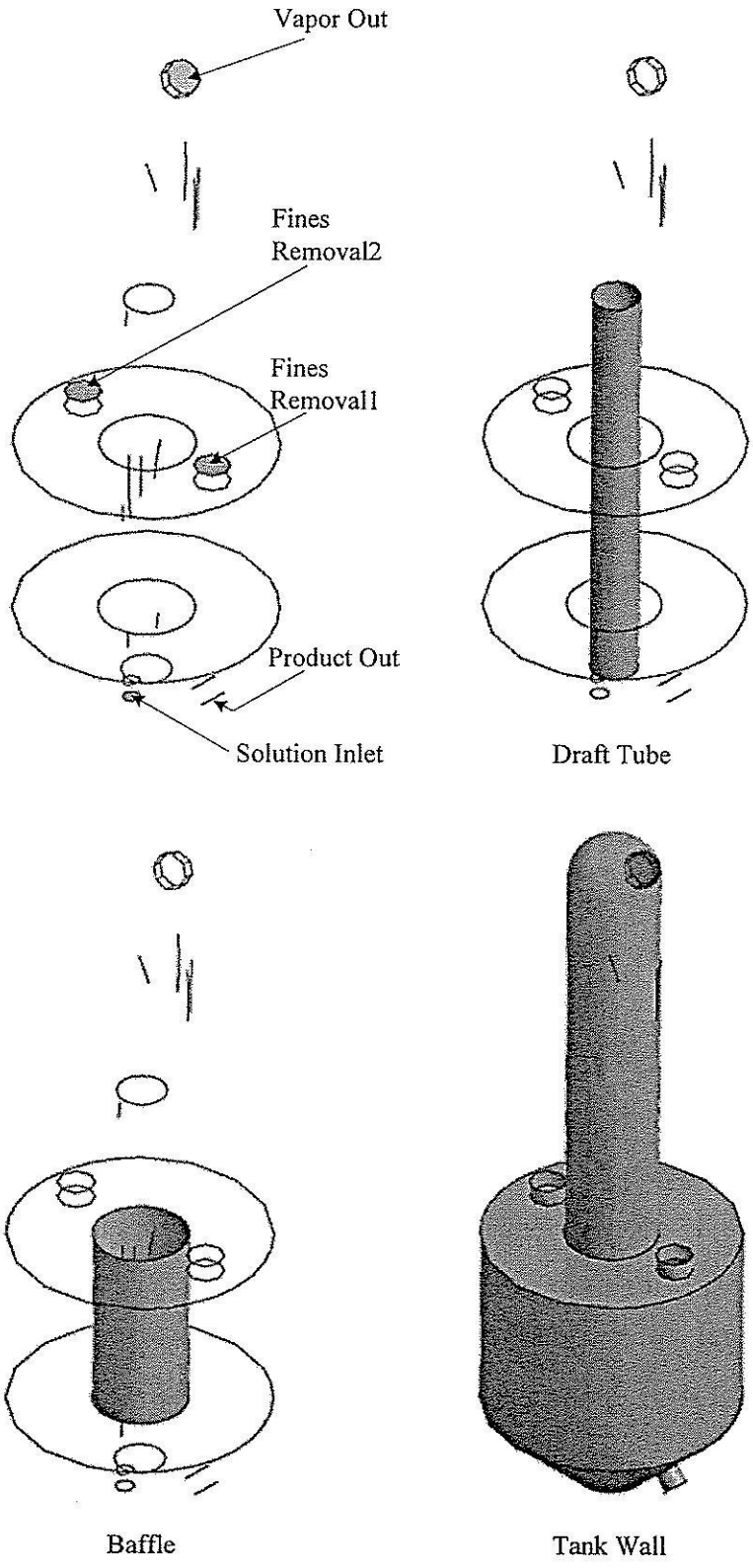

Fig. 4.3 Composite 2D regions.

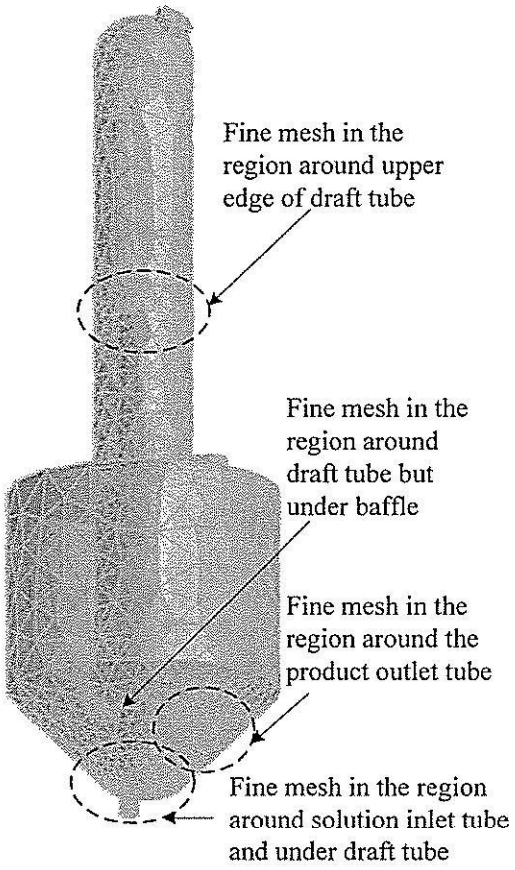

Fig. 4.4 Fine mesh in the specified region.

4.3.2.2 Procedures of the optimum mesh generation

The mesh generation is important to the numerical solutions. If the mesh is not suitable (particularly if the mesh spacing is too large), the numerical results diverge or produce incorrect results. The method which was used to find the optimum mesh is separated to four steps, as described below:

1st step: First the maximum spacing was set (this is the maximum element size which will be used when creating triangles on the faces of the body and tetrahedral element in the volume of the body); the initial setting is set automatically by the program to around 5% of the maximum extent of the model. Then the maximum edge length (this is set equal to the maximum spacing) and the minimum edge length were set. Finally, the mesh was created and then loaded into the CFX-Pre to specify the model conditions, fluid properties, flow conditions, initial conditions, and boundary conditions. Note that these conditions will be the same for all runs.

2nd step: the second step of the mesh creation is variable based mesh adaptation. This technique is used to increase the mesh density in the region of a liquid-vapor interface. CFX-Pre has a mesh adaptation mode where once or more during a run, the mesh is selectivity refined in areas which depend on the adaptation criteria specified. This means that as the solution is calculated, the mesh density can automatically be increased or decreased in locations where solution variables change rapidly, in order to resolve the features of the flow in these regions. In this work, the vapor volume fraction was selected as the adaptation variable, because it is an important variable that changes rapidly in the region of the liquid-vapor interface. The number of adaptation steps was set to 2, and the maximum iterations per step to 200: (if the maximum iterations is set to 300, this results in a total maximum number of iterations of 600 [200*2+300 = 700]). Note that this step uses the same parameters for all runs.

3rd step: Solve the problem using the CFX-Solver. Calculate and extract the liquid velocity (and other variables) at the measured positions from the results file (see Figure 4.5).

4th step: Decrease the maximum spacing, maximum edge length, and minimum edge length and then repeat the 2nd and 3rd steps. The liquid velocity of each run was compared; if the values are different, these parameter values must be adjusted continuously until the change in the values of the simulated variables is small or zero. Meshes that give no change in values of the simulated variables (mesh independent results) are the optimum meshes, but a mesh that has the maximum mesh scale to reduce the calculation times or the average calculation size should be selected for computational efficiency. All mesh scales in each run used to determine mesh independent results are summarized in Table 4.3. The liquid velocities of each run are compared in Figures 4.6 to 4.13.

Table 4.3 Mesh sizes of each run, which used to find the optimum mesh.

Run Number	Maximum Edge Length[1] (m)	Minimum Edge Length (m)	Number of Nodes		Number of Elements	
			Before mesh adaption	After mesh adaption	Before mesh adaption	After mesh adaption
1	0.17	0.0085	8,421	41,485	41,068	207,461
2	0.1	0.007	8,634	42,248	41,961	210,960
3	0.1	0.001	9,460	46,557	46,606	233,682
4	0.09	0.001	9,899	47,735	48,503	238,977
5	0.08	0.001	10,257	49,461	50,341	247,376
6	0.07	0.001	11,782	55,971	57,398	279,436
7	0.06	0.001	13,330	63,997	65,475	319,291

[1]Maximum edge length is set equal to the maximum spacing.

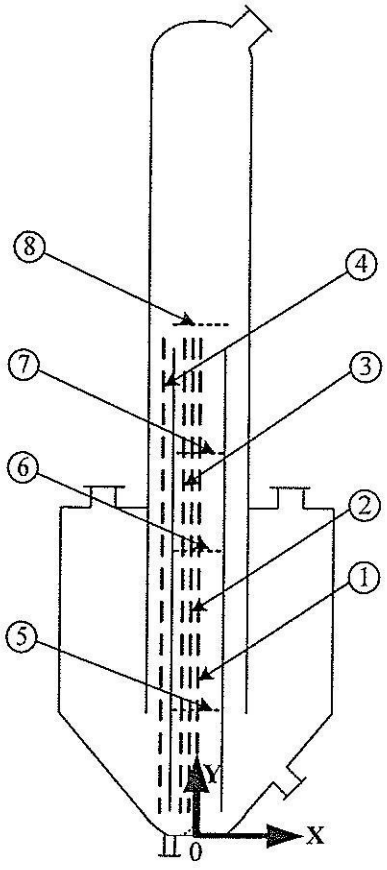

Line number	Beginning point	Final point
1	(0,0.1,0)	(0,2.0,0)
2	(-0.035,0.1,0)	(-0.035,2,0)
3	(-0.07,0.1,0)	(-0.07,2.0,0)
4	(-0.13,0.1,0)	(-0.13,2.0,0)
5	(-0.098,0.4,0)	(0.098,0.4,0)
6	(-0.098,1.0,0)	(0.098,1.0,0)
7	(-0.098,1.5,0)	(0.098,1.5,0)
8	(-0.1,2.05,0)	(0.1,2.05,0)

Fig. 4.5 Line positions used to measure the liquid velocity. The positions given are in the form are (x,y,z).

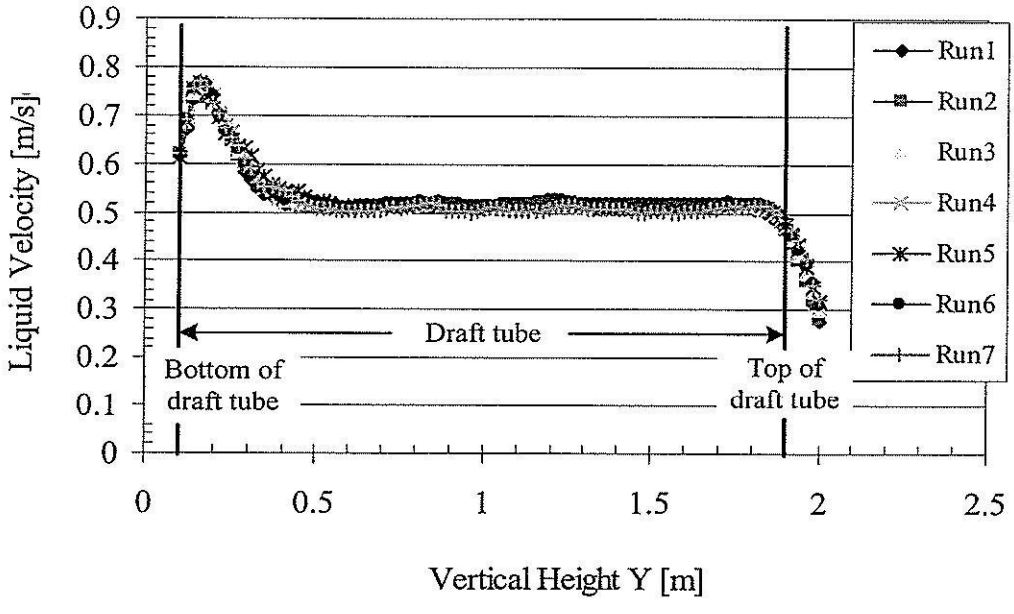

Fig. 4.6 Liquid velocity profile at line 1.

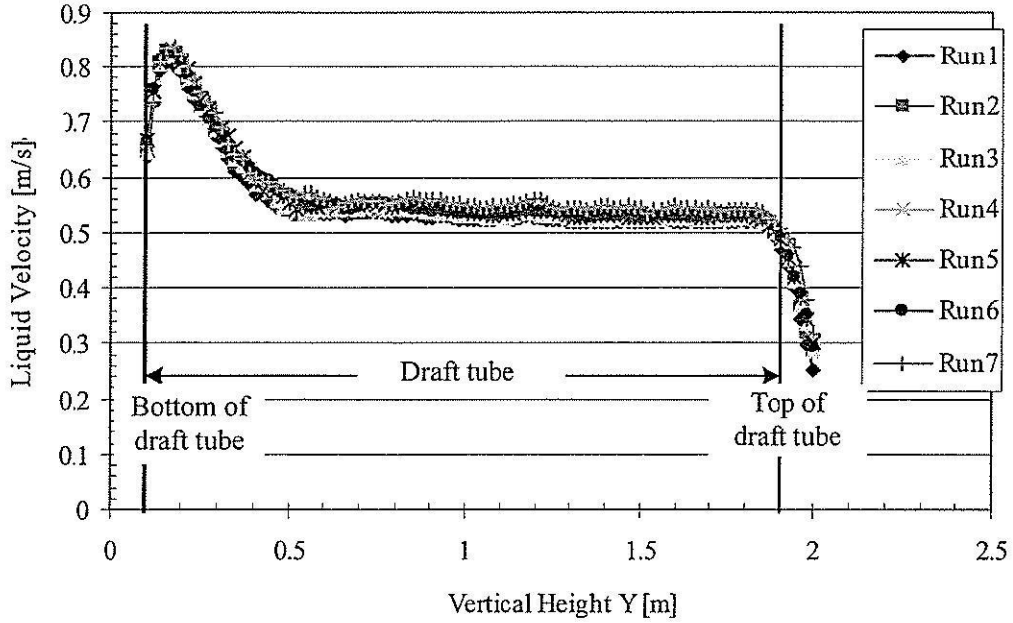

Fig. 4.7 Liquid velocity profile at line 2.

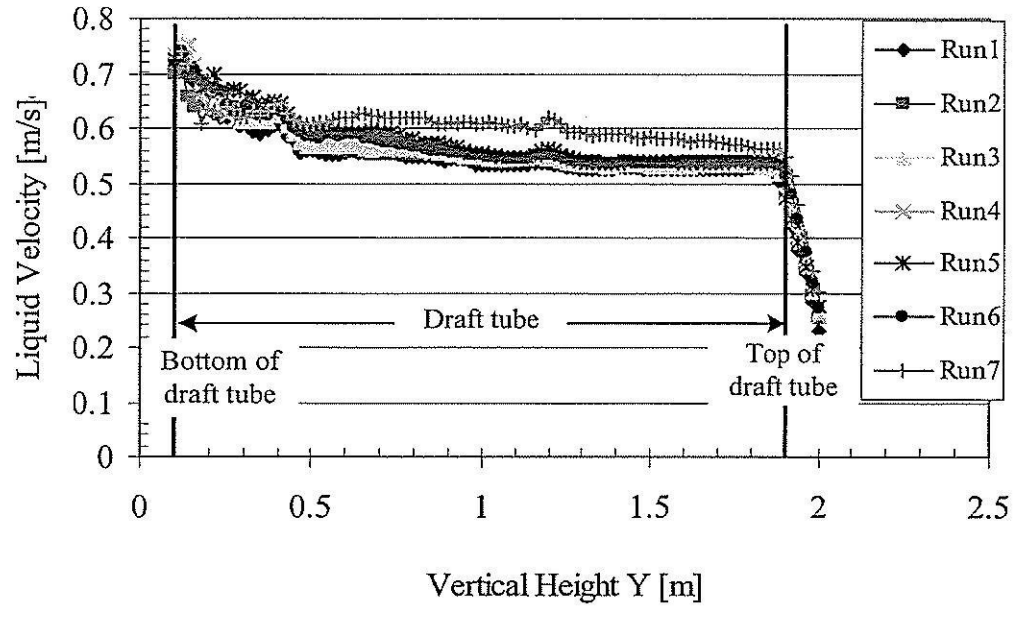

Fig. 4.8 Liquid velocity profile at line 3.

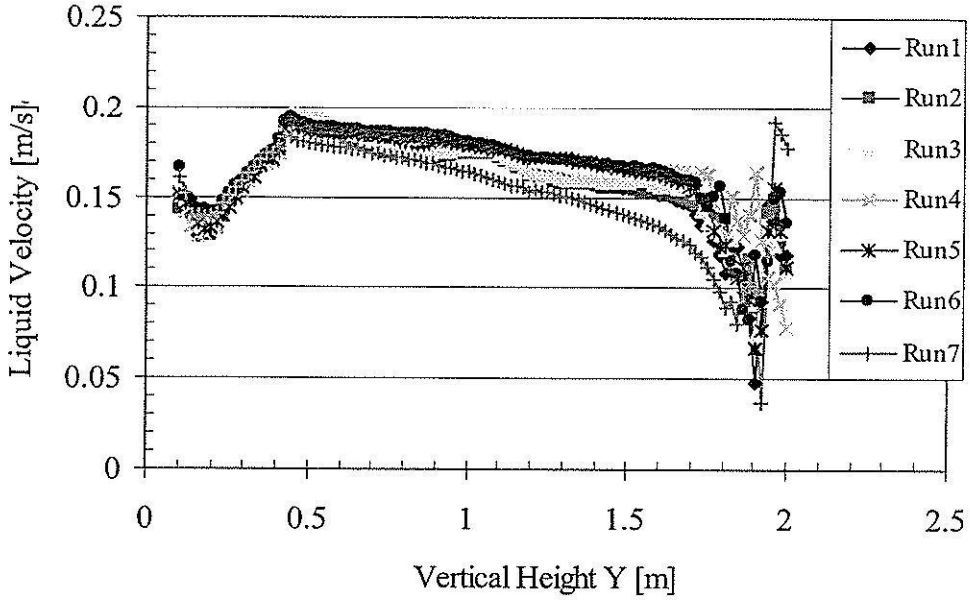

Fig. 4.9 Liquid velocity profile at line 4.

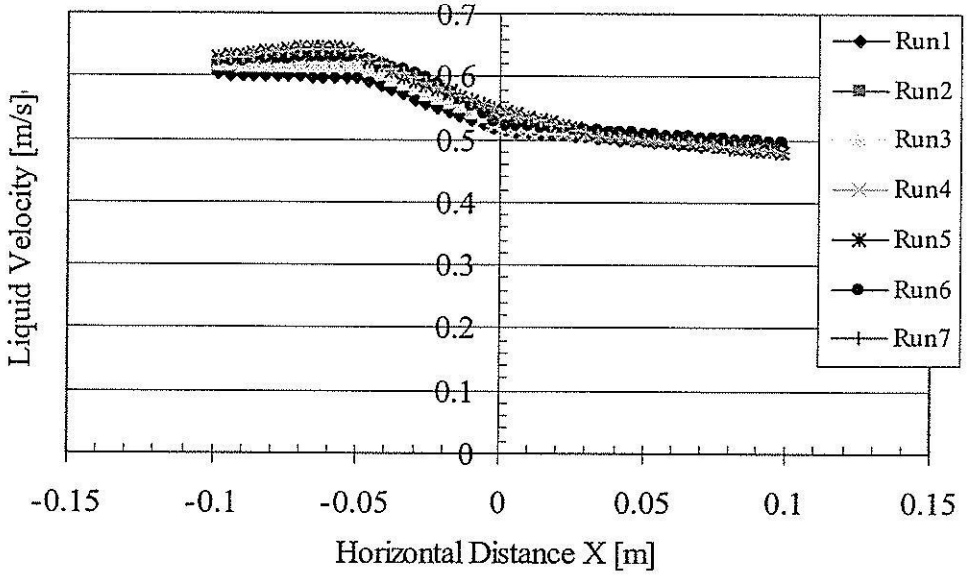

Fig. 4.10 Liquid velocity profile at line 5.

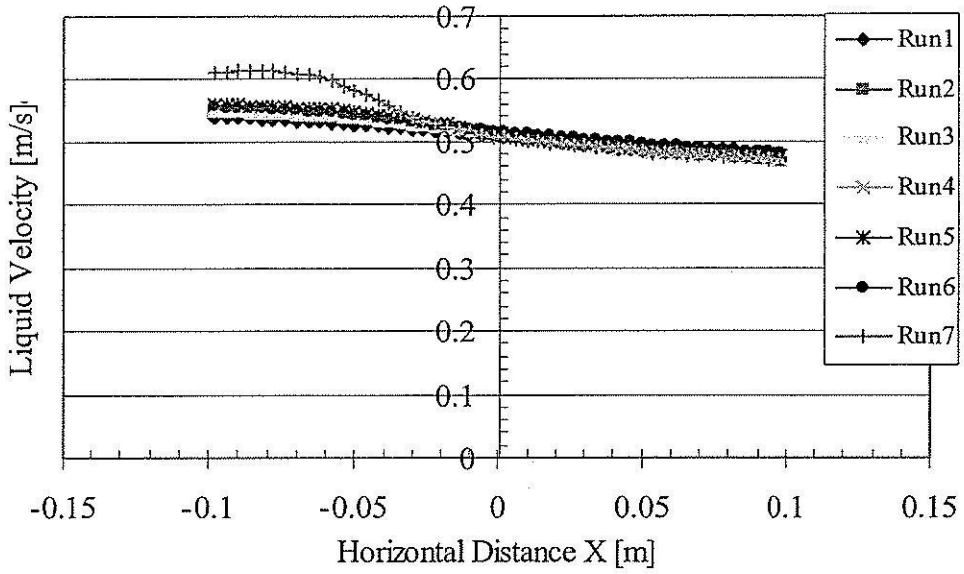

Fig. 4.11 Liquid velocity profile at line 6.

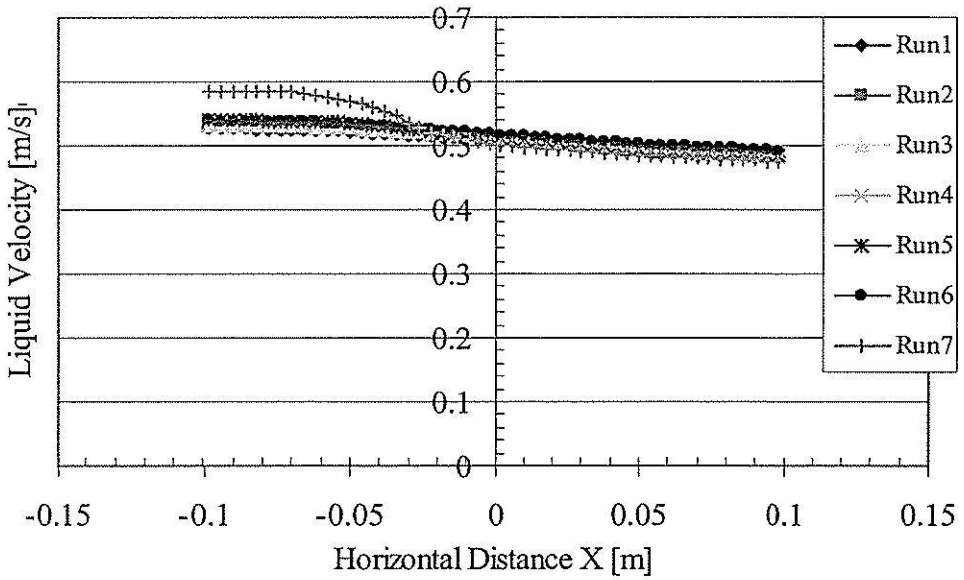

Fig. 4.12 Liquid velocity profile at line 7.

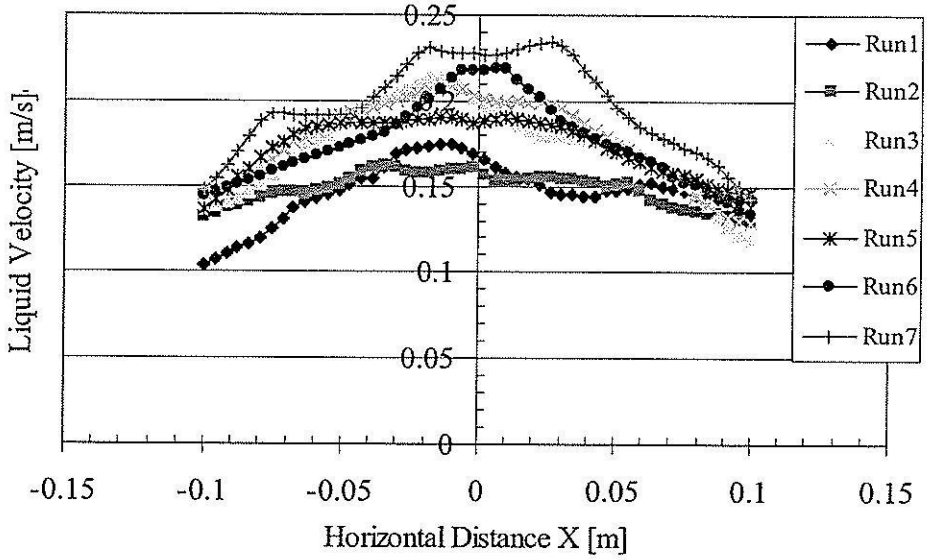

Fig. 4.13 Liquid velocity profile at line 8.

Figures 4.6 to 4.13 show that the liquid velocity profiles at line 1, 2, and 5 of all run are not different or have only small differences, but at line 3, 4, 6, 7, and 8 liquid velocity profiles of run number 7 (the smallest mesh size) is different from the other runs. It can be seen that the different velocity of run number 7 occurs at near the draft tube wall so that the fine mesh size in this region should be considered. This mesh is shown in Figure 4.14 and the new runs with this mesh are shown in Table 4.4 and liquid velocity profiles for each line are shown in Figure 4.15 to 4.22.

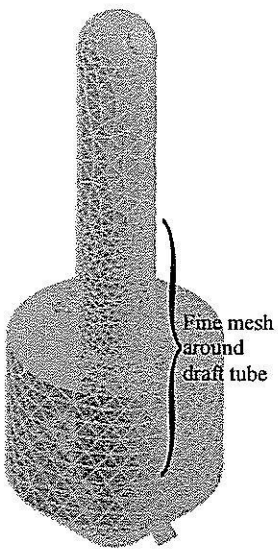

Fig. 4.14 Geometry showing fine mesh around draft tube.

Table 4.4 Mesh sizes of each run with the fine mesh around draft tube.

Run Number	Maximum Edge Length (m)	Minimum Edge Length (m)	Number of Nodes		Number of Elements	
			Before mesh adaption	After mesh adaption	Before mesh adaption	After mesh adaption
8	0.17	0.0085	15,012	71,841	73,672	358,549
9	0.1	0.001	15,630	75,547	77,144	378,233
10	0.09	0.001	15,952	76,619	78,663	383,757
11	0.08	0.001	15,986	77,226	78,726	386,259
12	0.07	0.001	16,962	82,341	83,136	411,021
13	0.06	0.001	17,870	87,467	88,061	437,243
14[1]	0.1	0.001	16,058	77,867	79,460	389,739

[1]This run, the overall edge lengths are the same as run number 9, but the maximum edge length around draft tube is 0.07 m.

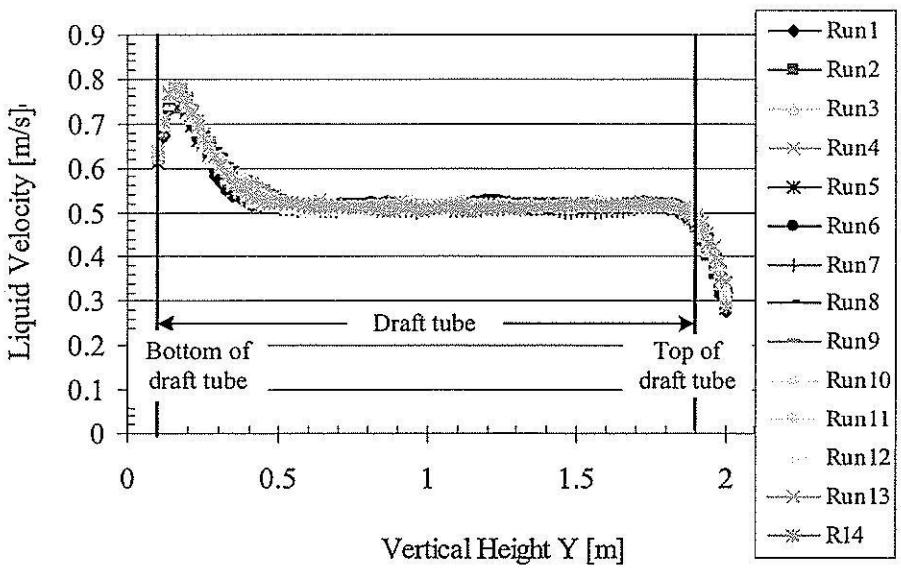

Fig. 4.15 Liquid velocity profile at line 1 with fine mesh around draft tube.

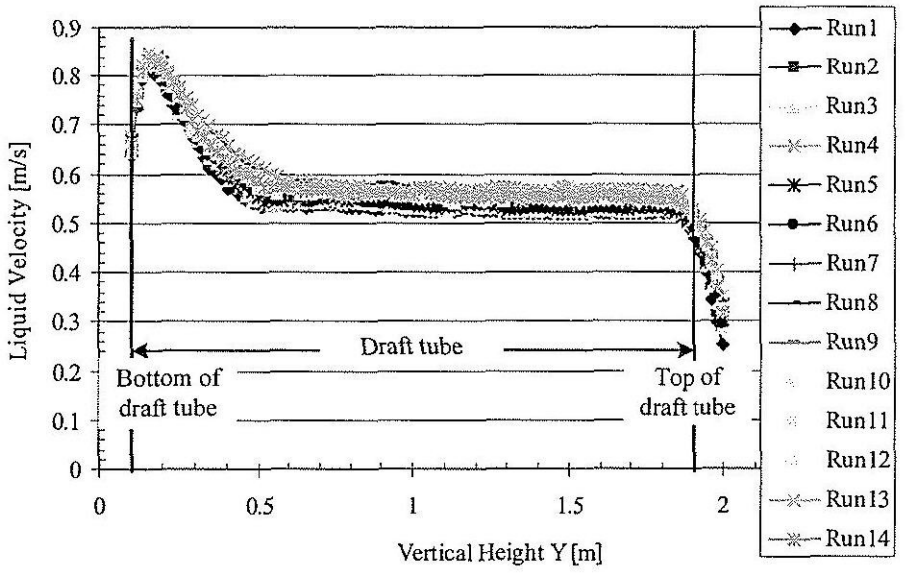

Fig. 4.16 Liquid velocity profile at line 2 with fine mesh around draft tube.

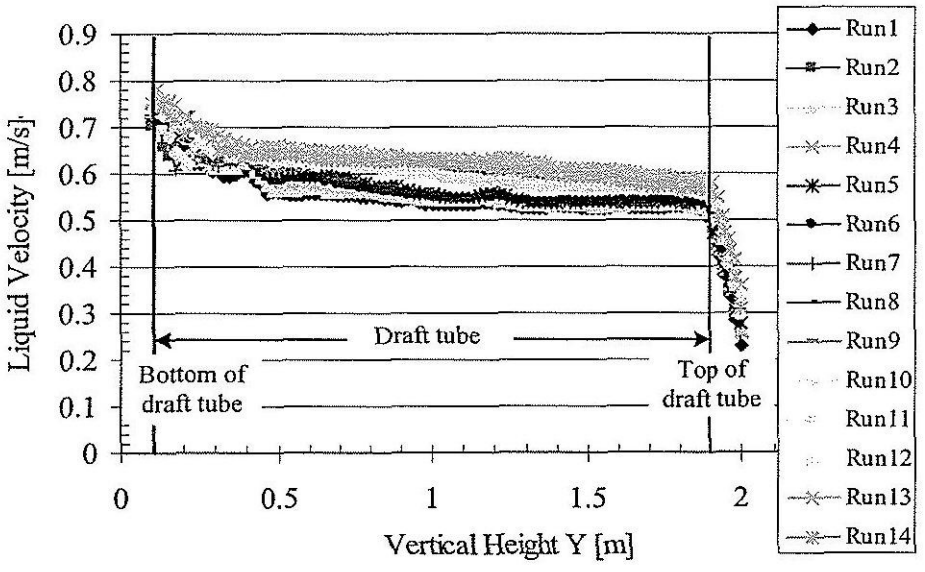

Fig. 4.17 Liquid velocity profile at line 3 with fine mesh around draft tube.

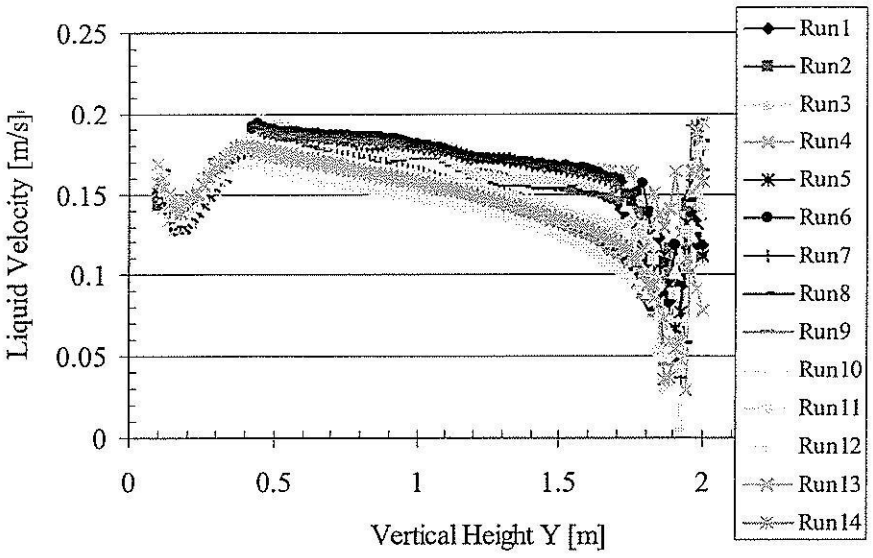

Fig. 4.18 Liquid velocity profile at line 4 with fine mesh around draft tube.

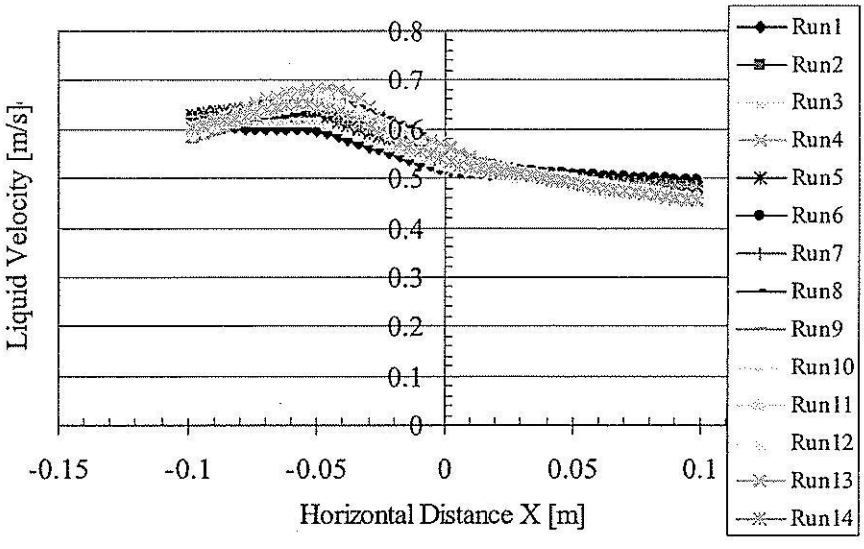

Fig. 4.19 Liquid velocity profile at line 5 with fine mesh around draft tube.

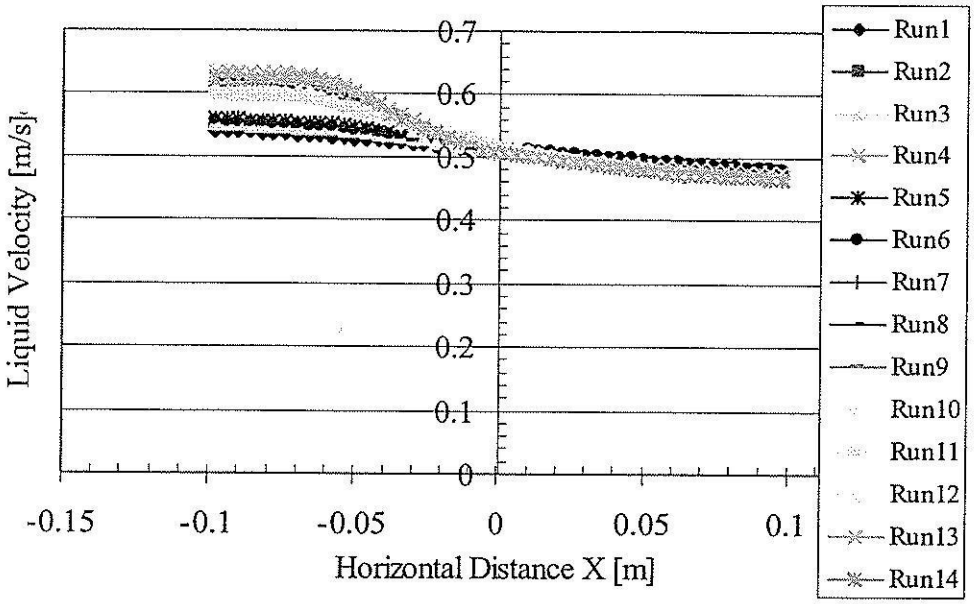

Fig. 4.20 Liquid velocity profile at line 6 with fine mesh around draft tube.

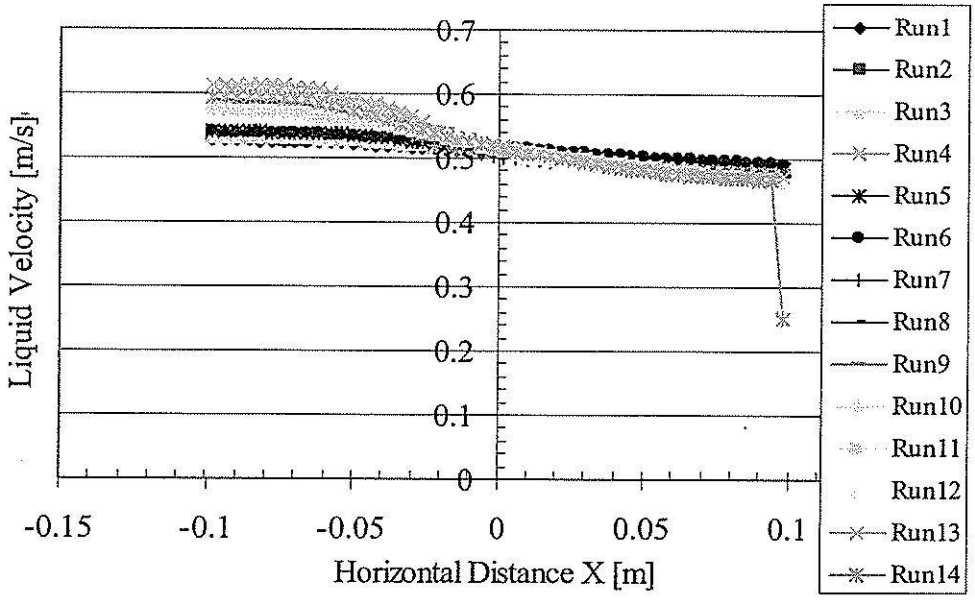

Fig. 4.21 Liquid velocity profile at line 7 with fine mesh around draft tube.

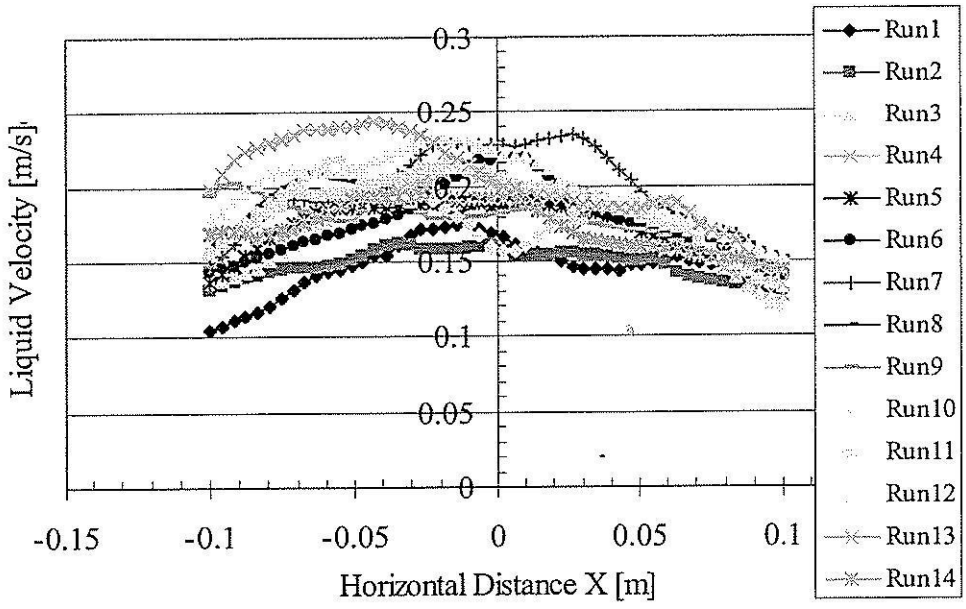

Fig. 4.22 Liquid velocity profile at line 8 with fine mesh around draft tube.

Considering run numbers 8 to 14 in Figure 4.15 to 22, it is seen that the liquid velocity profiles have only small differences so that the mesh size of run number 14 is selected to simulate a DTB crystallizer for all cases studied, because it gives an average value of the velocity profile between the value determined from the maximum and minimum mesh size and the size is small. The mesh of a DTB crystallizer with this mesh size is shown in Figure 4.23. Note that the number of nodes and elements after mesh adaptation are not necessary to equal to the run number in Table 4.4 because they depends on the flow condition in the system.

For the non-isothermal simulation section of the research no modeling of the area above the liquid free surface (the liquid free surface is at the height of 2.11 m) was performed. The optimum mesh size is of the same magnitude as the isothermal simulation section, so that the mesh of the DTB crystallizer for non-isothermal simulation with this mesh size is shown in Figure 4.24. Note that the number of nodes and elements after mesh adaptation is not necessarily equal to Figure 4.24 because this depends on the flow conditions in the system.

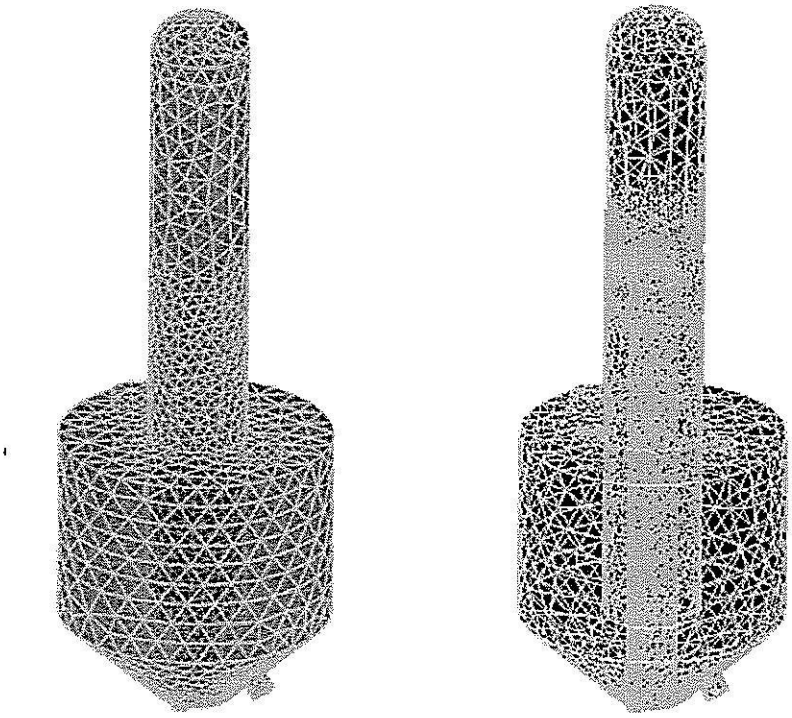

(a) (b)

Fig. 4.23 Mesh size of Run14: (a) before, and (b) after mesh adaptation.

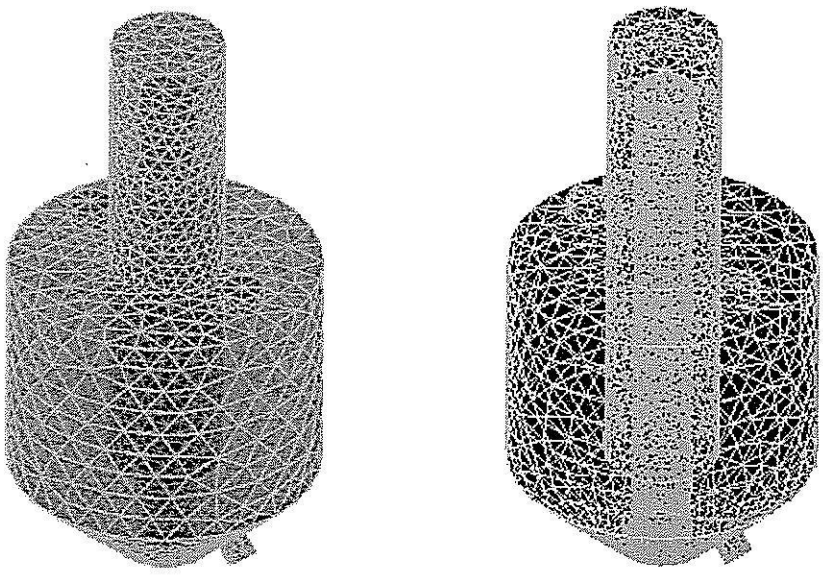

(a) (b)

Fig. 4.24 Examples of mesh size of a DTB crystallizer for non-isothermal simula-tion part: (a) before mesh adaption; (b) after mesh adaption.

4.3.3 Physical definition

The physical definition step comprises several definition steps. The mesh files are loaded into the physics pre-processor, CFX-Pre. The physical models which are to be used in the simulation are selected. Fluid properties and boundary conditions are specified.

4.3.3.1 Fluid properties

The physical properties (water solution with 26.66 % NaCl [liquid] and water-vapor [vapor]) are presented in Table 4.5. Note that all properties of water-vapor are available in ANSYS CFX-10.0 program and all properties of water solution with 26.66% NaCl at 25 °C were taken from Mullin (2001), with the exception of the specific heat capacity which was taken from Perry and Green (1999).

Table 4.5 Physical properties of vapor and liquid.

Physical properties (units)	Phase	
	Liquid	Vapor
Density ($kg \cdot m^{-3}$)	1198.00	0.59
Viscosity ($kg \cdot s^{-1} \cdot m^{-1}$)	0.00152	0.0000124
Thermal conductivity ($W \cdot m^{-1} \cdot K^{-1}$)	0.57	0.025
Boiling temperature (K)	380.60	-
Specific heat capacity ($J \cdot kg^{-1} \cdot K^{-1}$)	3336.85	2080.10
Surface tension ($N \cdot m^{-1}$)	0.077	-

4.3.3.2 Flow conditions

Isothermal simulation

In this part, the following flow conditions were selected:

1. Steady state flow.

2. The reference pressure was set to 0 Pa.

3. The buoyancy reference density was set to the density of the least dense fluid (vapor phase), that is 0.59 kg/m^3.

4. The multiphase option was set to the inhomogeneous free surface flow.

5. Turbulence was set to the homogeneous model with the $k-\varepsilon$ model. The turbulent wall function was set to the scalable wall function. There are more details of this model in chapter 3.

6. The liquid phase was set as the continuous phase. The vapor phase was defined as a dispersed fluid phase with a mean diameter of 2 mm. The fluid buoyancy model was set to the density difference model for both fluids

7. For the interphase transfer model, the interphase transfer model was set to the particle model, the drag force was set to the Ishii and Zuber model, the turbulent dispersion force was to the Lopez de Bertodano model with a dispersion coefficient of 0.3, and the turbulence transfer was set to Sato Enhanced Eddy Viscosity model. More details of these models are provided in chapter 3.

9. The momentum source value was specified directly in the momentum source region (impeller subdomain, see Figure 4.25) and set to the same value for both fluids. The values of each run are shown in Table 4.1 and 4.2.

Non-isothermal simulation

In this part, the following flow conditions were selected:

1. Steady state flow.

2. The reference pressure was set to 0 Pa.

3. The buoyancy reference density was set to the density of the continuous phase (liquid phase), that is 1198 kg/m^3.

4. The multiphase option was set to inhomogeneous multi-phase flow.

5. Turbulence was set to the inhomogeneous model.

6. The heat transfer model was set to the inhomogeneous interphase heat transfer model with fluid dependent heat transfer.

7. For the liquid phase, the liquid phase was set as the continuous phase, the heat transfer was set to the thermal energy heat transfer model, the turbulence model was set to the $k-\varepsilon$ model, the turbulent wall function was set to the Scalable model, and the fluid buoyancy model was set to the density difference model. M ore details of these models is shown in chapter 3.

8. For the vapor phase, the vapor phase was set to the dispersed fluid phase with a mean diameter of 2 mm, the heat transfer was set to an isothermal heat transfer model (at a

constant saturation temperature of 107.6 degree Celsius), the turbulence was set to the dispersed phase zero equation model, and the fluid buoyancy model was set to the density difference model. More details of these models are in chapter 3.

9. For the interphase transfer model, the interphase transfer model was set to the particle model, the drag force was set to the Ishii and Zuber model, the turbulent dispersion force was set to the Lopez de Bertodano model with a dispersion coefficient of 0.3, the turbulence transfer was set to Sato Enhanced Eddy Viscosity model, the heat transfer was set to two resistance model with the Hughmark correlation on the liquid phase and Zero Resistance in the vapor phase, and mass transfer was set to the thermal phase change model with the saturation temperature of 107.6 degree Celsius. More details of these models can be seen in chapter 3.

10. The momentum source value was specified directly in the momentum source region (the impeller subdomain, see Figure 4.25) and set to the same value for both fluids. The heat source value was specified directly to the subdomain and set only for the liquid phase. The values of each run are shown in Table 4.1 and 4.2.

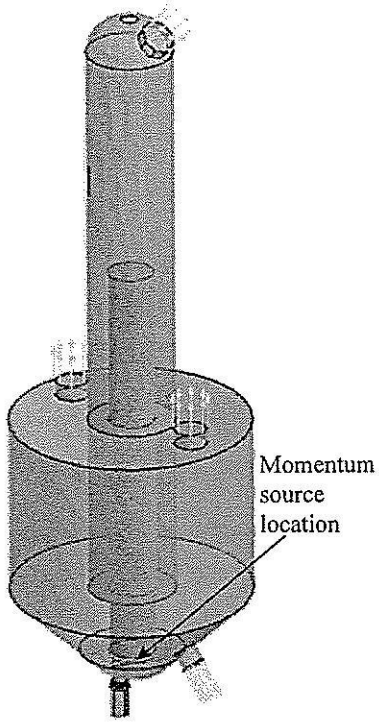

Fig. 4.25 Locations of momentum source and heat source.

4.3.3.3 Initial and boundary conditions

Boundary conditions

Boundary conditions are specifications of properties or condi-tions on the surface of domains and are required to fully define the flow simulation. The following fluid boundary condition types are available in ANSYS CFX-10.0 (ANSYS Canada Ltd., 2005):

1. *Inlet*: Fluid is constrained to flow into the domain only.
2. *Outlet*: Fluid is constrained to flow out of the domain only.
3. *Opening*: Fluid can simultaneously flow both in and out of the domain. This is not available for domains with more than one fluid present.
4. *Wall*: Impenetrable boundary to fluid flow
5. *Symmetry plane*: A plane of both geometric and flow symmetry.

The following boundary conditions were used in this work:

1. *Inlet*: The cross-sectional surface area at the solution inlet tube was set to the inlet boundary condition and called "Solution Inlet". For this boundary, the flow direction is perpendicular to the surface. For the isothermal simulation, the mass flow rates of each phase were specified directly, the volume fraction of vapor was set to 0.1, and the volume fraction of liquid was set to 0.9. For non-isothermal simulation, the bulk mass of the liquid flow rate was specified directly, and the volume fraction of liquid and vapor respectively set to 1.0 and 0.0, and the bulk liquid temperature was set to 107.6 degree Celsius. The values of the mass flow rate of each phase and bulk mass flow rates of each run are shown in Table 4.1 and 4.2. The turbulence option was set to medium (intensity = 5%).

2. *Outlet*: For this boundary, the flow direction is perpendicular to the given surface. In this work, the boundaries are separated into three locations:

- The cross-sectional surface area at the outlet of the product outlet tube, which is called "Product Out". For this boundary, the mass flow rate of each phase was specified directly. The values of each run are shown in Table 4.1 and 4.2.
- The cross-sectional surface area at the two outlet fines removal tubes, which are called "Fines Removal1" and "Fines Removal2", respectively. At these boundaries, the bulk mass flow rate was specified directly. The values of each run are shown in Table 4.1 and 4.2.
- The cross-sectional surface area at the vapor outlet tube, which is called "Vapor Out" (this is only the boundary condition for isothermal simulation part). For

this boundary, the mass flow rate of each phase was specified directly. The values of each run are shown in Table 4.1.

- The cross-sectional surface area at the liquid free surface is an outlet boundary with a degassing condition (this is only a boundary condition for non-isothermal simulation part). For this condition, the continuous phase sees this boundary as a free-slip wall and does not leave the domain but the dispersed phase sees this boundary as an outlet.

3. *Wall*: The wall of the draft tube, baffle, and tank wall were set to the no-slip and smooth wall conditions for both simulation parts. Moreover, these walls were together set to an adiabatic wall conditions for non-isothermal simulation part.

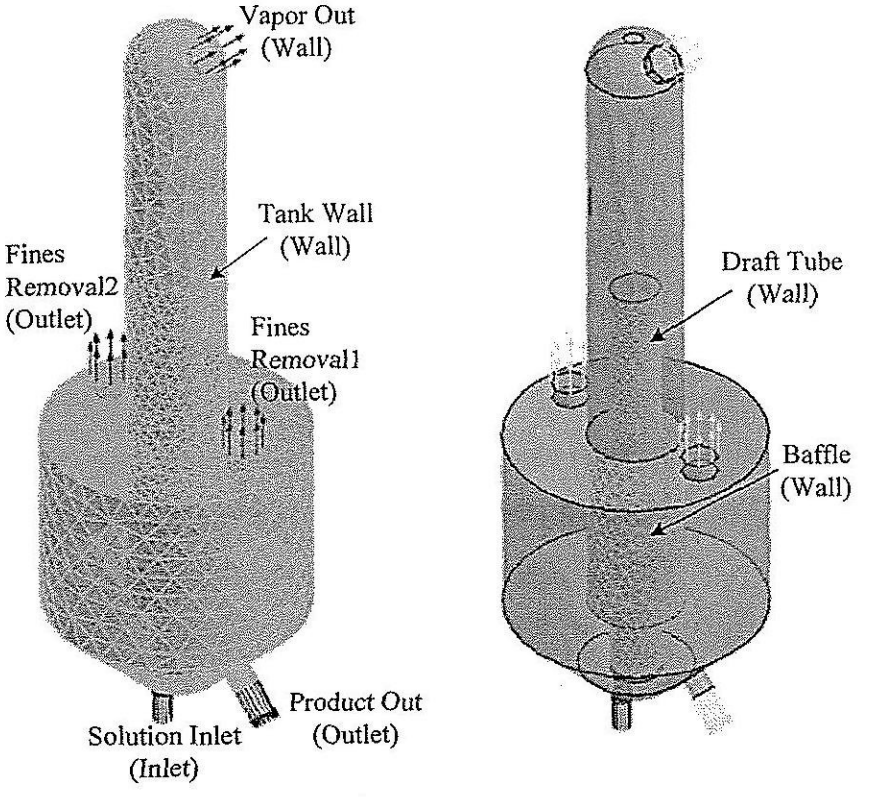

Fig. 4.26 The boundary conditions of the DTB crystallizer for isothermal simulation.

Initial conditions

The initial and boundary conditions for the pressure field and volume fraction of free surface flow must be consistent (i.e. the pressure field is hydrostatic in the liquid phase and

uniform in the vapor phase). This condition was achieved using CEL (the CFX expression language) defining a step function, as shown below:

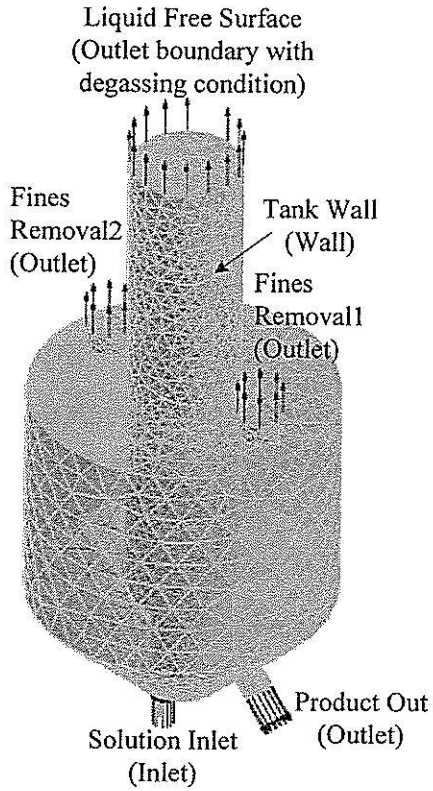

Fig. 4.27 The boundary conditions of the DTB crystallizer for non-isothermal simulation.

Den = *1198* [kg m^-3]

FH = *2.11* [m]

VFLiquid = step((*FH*-*y*)/1 [m])

VFVapor = 1-*VFLiquid*

Press = *Den**g*(*FH*-*y*)**VFLiquid*

where *Den* is the density of liquid phase, *FH* is the liquid level or free surface height, *VFVapor* is the volume fraction of vapor phase, *VFLiquid* is the volume fraction of liquid phase, and *Press* is the pressure. These functions are appropriate to initialize the relative pressure field and volume fraction as shown in Figure 4.28.

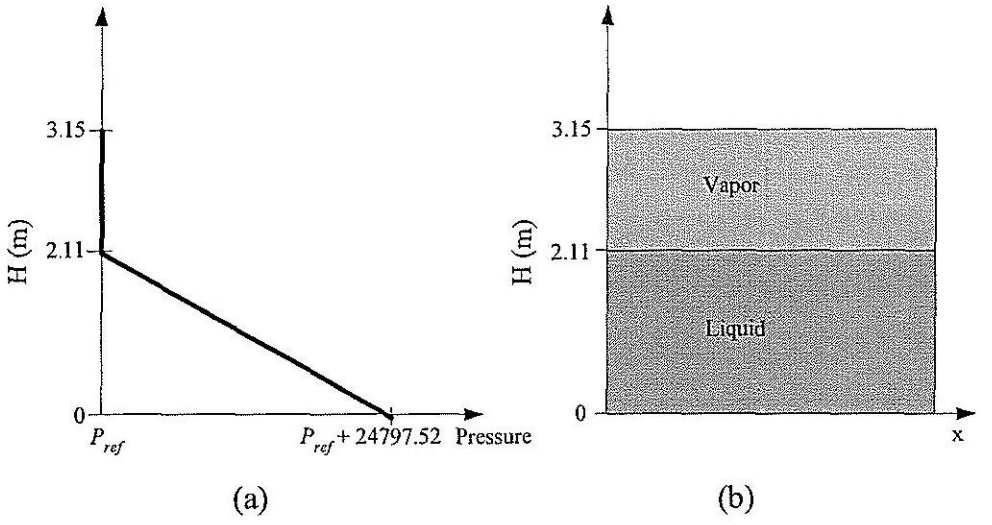

Fig. 4.28 Initial conditions: (a) pressure; (b) volume fraction.

The initial conditions of this work are shown below:

1. The initial static pressure, volume fraction of liquid phase, and volume fraction of vapor phase were set to; *Press*, *VFLiquid*, and *VFVapor*, respectively for isothermal simulation part; and automatic values, 1.0, and 0.0, respectively for non-isothermal simulation part.

2. The velocity of each phase was specified directly with the same with the velocity of the solution inlet.

3. The turbulent kinetic energy and turbulent eddy dissipation was set to automatic values.

4. For the non-isothermal simulation, the static temperature of the liquid was set to 373.0 K.

4.3.3.4 Mesh adaptation and solver control

Since the flow is free surface flow, it is necessary to adjust the mesh at the liquid-vapor interface. CFX-Pre has the mode to do this with more detail shown in the 2^{nd} part of section 4.3.2.2.

Solver control is used to set parameters that control the CFX-Solver during the solution stage, and appropriate parameters are essential in order to obtain good convergence of the solution. In this work, the advection scheme was set to the upwind option. The timescale control was set to auto timescale and the maximum number of

iterations was set to 300. The RMS (root mean square) residual type was used with a target value of 0.00001.

All sub-sections in section 4.3.3 are the processes in CFX-Pre. CFX-Pre produces a solver (definition) file which is then passed to the CFX-Solver to solve the simulation.

4.3.4 Solver

CFX-Solver solves all variables for the simulation of the problem specification in CFX-Pre by the finite volume method with an unstructured mesh.

CFX-Solver is solved as follows:

1. The partial differential equations (mass, momentum, energy equations and turbulent) are integrated over all the control volumes in the region of interest
2. These integral equations are converted to a system of algebraic equations by generating a set of approximations for the term in the integral equations.
3. The algebraic equations are solved iteratively until the convergence criteria or max iteration is reached.

Exact details of the calculation methods for the software are available in the detailed user notes accompanying the software (ANSYS Canada Ltd., 2005). More details about the finite-volume method (the discretisation of equations and solution strategy) to solve the gas-liquid system has been discussed by Oey (2005).

The solver produces a results file which is then passed to the post-processor.

4.3.5 Post-processing

CFX-Post is the component used to analyze, visualize and present the results.

Examples of some important features of CFX-Post are:

- Visualization of the geometry and control volumes
- Vector plots of the direction and magnitude of the flow
- Virtualization of the variation of scalar variables (variables which have only magnitude, not direction, such as pressure, temperature, speed, etc.) through the domain
- Streamline of the vapor and liquid
- Charts showing graphical calculations
- Other representations of variables of interest.

The results from CFX-Post of all studies in this research are shown and discussed in chapter 5.

Chapter V

Results and Discussion for the DTB Crystallizer

5.1 Isothermal Simulations

5.1.1 General characteristics of Flow Fields in an Isothermal DTB crystallizer

The general flow patterns in the DTB crystallizer are shown in Figure 5.1, which represents the velocity vectors, and contours in the vertical center plane, and 3D streamlines for the liquid and vapor phases. It shows that the liquid phase has to flow through and over the draft tube and therefore there is net circulation through the draft tube. It is necessary to have this flow characteristic because the function of the draft tube is to assist in suspension of the crystals as was described in Paul et al. (2004). The liquid velocity in the upflow region (inside the draft tube) is higher than the downflow region (outside the draft tube). This is since the cross sectional area of the up flow region (approximately 0.0314 m^2) is smaller than the down-flow region (approximately 0.0820 m^2). The crystallizer is designed in this way to create a significantly higher velocity in the upward flow region to assist in suspension of particles, and this high upward velocity is produced from the momentum added with the impeller. At a larger distance upward from the impeller, the velocity profile becomes more uniform, although averaged velocities in the core remain low (this is far enough from the bottom tube end of the draft tube that the effect of the impeller is less significant), and the velocity is approximately half of the maximum (0.9843 m/s), which occurs at approximately 0.3 m (1.5 times the diameter of the draft tube) above the impeller. Moreover, there is a small recirculation loop occurring under the region where the flow comes over the top of the draft tube. This is more pronounced at the side of the draft tube above the feed, and is undesirable because it will lead to a non-uniform flow. This recirculation does not contribute at all to the desired circulation, and could lead to different crystallization rates for crystals that are trapped there.

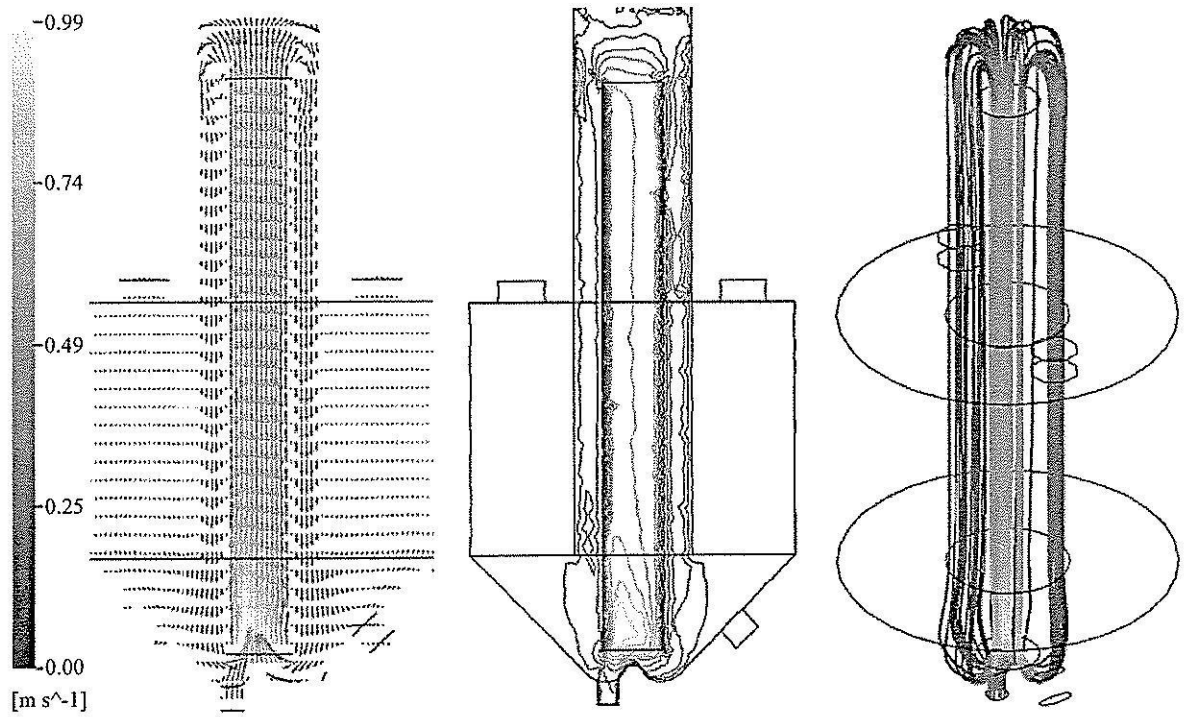

(a)

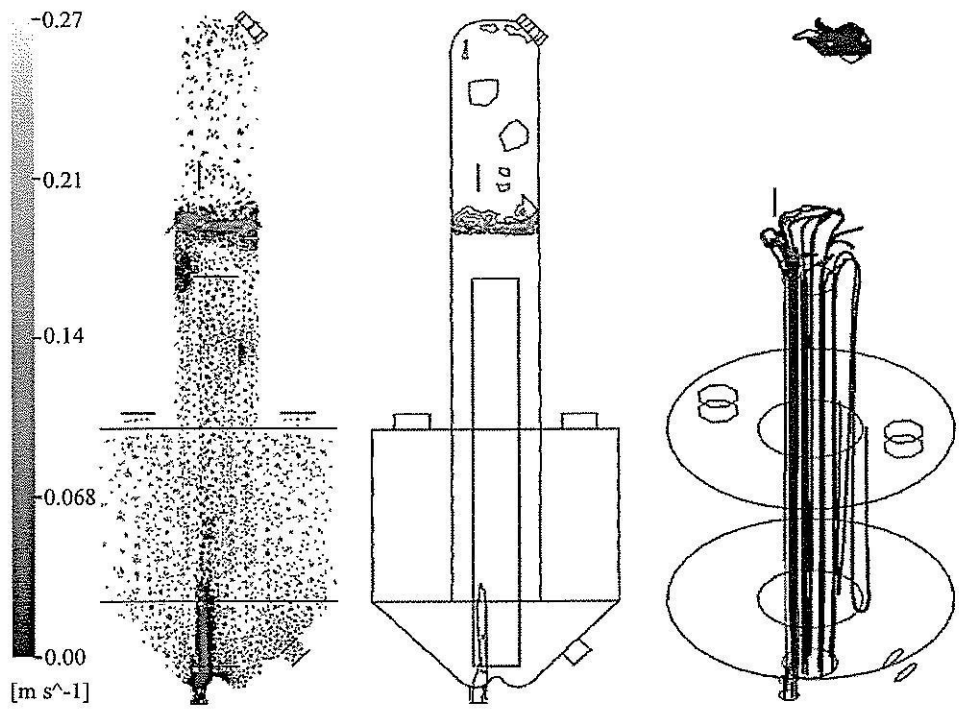

(b)

Fig. 5.1 Velocity vectors, contours, and 3D streamlines of liquid (a) and vapor (b) in the vertical center plane for case study 5.

The vapor phase is only present in small amounts in the system (Figures 5.1(b) and 5.2), and only in the draft tube, after which it is separated out at the vapor-liquid interface. This means that the vapor and liquid regions of the crystallizer are separated by a clearly-defined interface (free surface), which occurs at a height of 2.11 m, the same as the initial height of the free surface in the simulation. A small amount of vapor (less than 10 % by volume) is in the draft tube because the feed to the crystallizer is 10% volume fraction vapor. The vapor is mostly in the regions near the left side of the draft tube and mostly separates out from the liquid at the top of the draft tube near the left side of the tank rather than the center of the tank because the feed is located under a position between the left side of the draft tube and the tank wall, and the rate of the feed (and therefore the rate of vapor feed also) is quite high in this case.

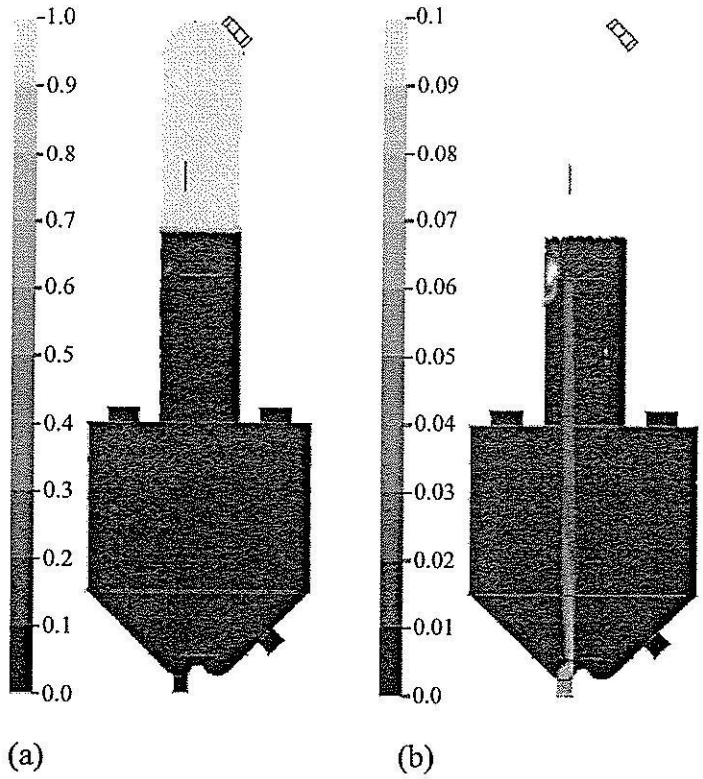

Fig. 5.2 Contours of vapor volume fraction in the vertical center plane for case study 5; (a) overall fraction; (b) using a magnified scale to enable visualization in the draft tube.

One drawback of many crystallizers is the tendency of the particles to sediment to the bottom of the tank and remain there. The shape of the tank bottom can significantly

improve the uniformity of the particle suspension. The rounded tank "corners" and a central peak under the agitator, which is the bottom shape of the DTB crystallizer used in this work, is one of the best configurations for the tank bottom. The rounding of the corners is used to combat settling of particles and the center peak virtually eliminates the stagnation point (dead zone) that would be present at the bottom center of the tank under the agitator (Myerson, 2002). These effects can be confirmed by the velocity vectors shown in Figure 5.3, which demonstrates that the flow of all fluid packets tends to be into the draft tube.

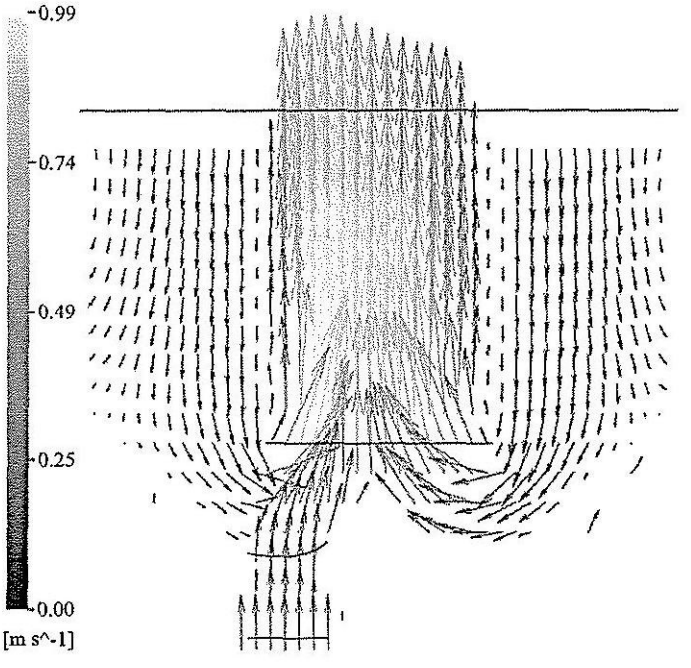

Fig. 5.3 Liquid velocity vectors at the tank bottom for case study 5.

5.1.2 Effect of the momentum source strength on the flow characteristics

The overall liquid velocity vectors and contours are shown in Figure 5.4, for momentum source values of 0, 0.785, and 3.142 kg·m/s^2, and in Figure 5.5 for momentum source values of 5.498, 7.850, 11.78, 19.63, and 23.56 kg·m/s^2. Flow contours for the same conditions as in Figure 5.5 are shown in Figure 5.6. Figure 5.4 indicates that for the cases of 0 (no momentum addition), 0.785, and 3.142 kg·m/s^2, the flow of the liquid phase does not follow the general flow field in a DTB crystallizer at the impeller location: for these three cases there is upward flow in some areas immediately outside the draft tube because the momentum addition through the impeller is very low, and is unable to force all the feed

solution to flow into the draft tube. For the cases of 5.498, 7.850, 11.78, 19.63, and 23.56 kg·m/s^2 (Figure 5.5), the flow of liquid follows the general flow field in a DTB crystallizer because the momentum addition through the impeller is high enough to assist the feed solution to flow into the draft tube.

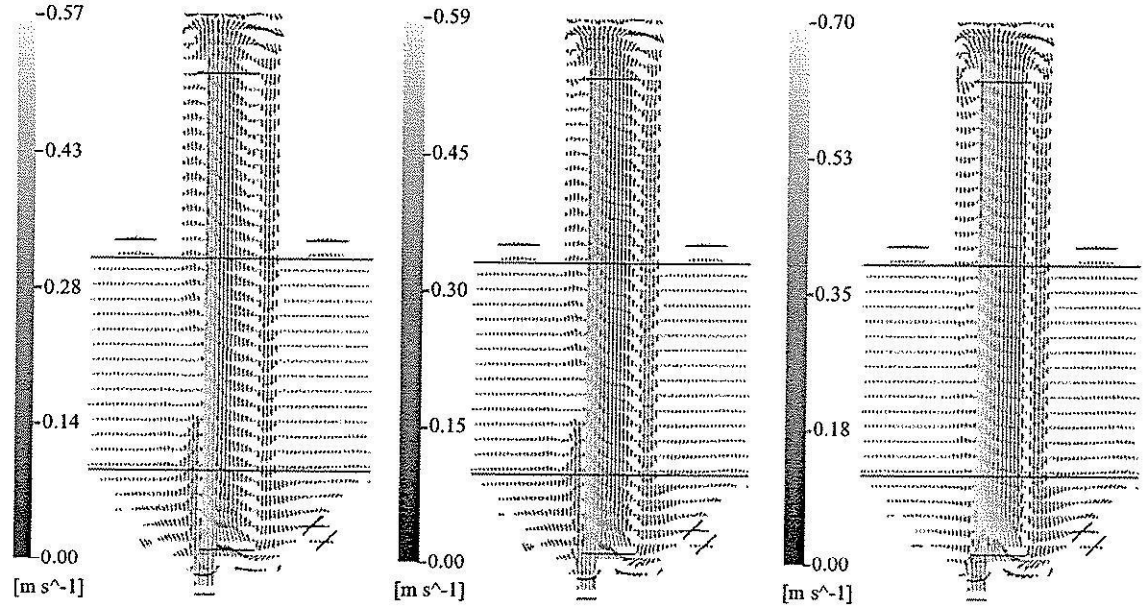

Fig. 5.4 Liquid velocity vectors in the vertical center plane for momentum source additions of (a) 0 kg·m/s^2; (b) 0.785 kg·m/s^2; (c) 3.142 kg·m/s^2.

As the momentum added through the impeller increases, the liquid velocity becomes larger both in the upflow section inside the draft tube and in the downflow area outside the draft tube. This results in a stronger flow at the bottom part of the draft tube and also a higher velocity inside the draft tube and a lower velocity in the annular space. The vapor velocity increases with increasing momentum source addition also, however it increases by a much smaller degree than the liquid velocity (see Figure 5.7).

The uniformity of the liquid flow can be seen by the overall velocity contours in Figure 5.6. Full uniformity for the liquid velocity in the particle settling zone was found for all the case studies; it is necessary to have uniform flow in this zone to aid in the classification of the crystals. The uniform flow and very low velocity of this zone indicate that there will be very slow crystallization kinetics in this zone. This is suitable because this zone is designed for the purpose of the particle settling process only. At the point that

the liquid flows over the top of the draft tube, and at the vapor-liquid interface, the overall flow feature is non-uniform for all case studies. This will lead to spatial variation in the kinetics of the processes occurring in crystallization, in particular the nucleation rate because of variations in the shear stress.

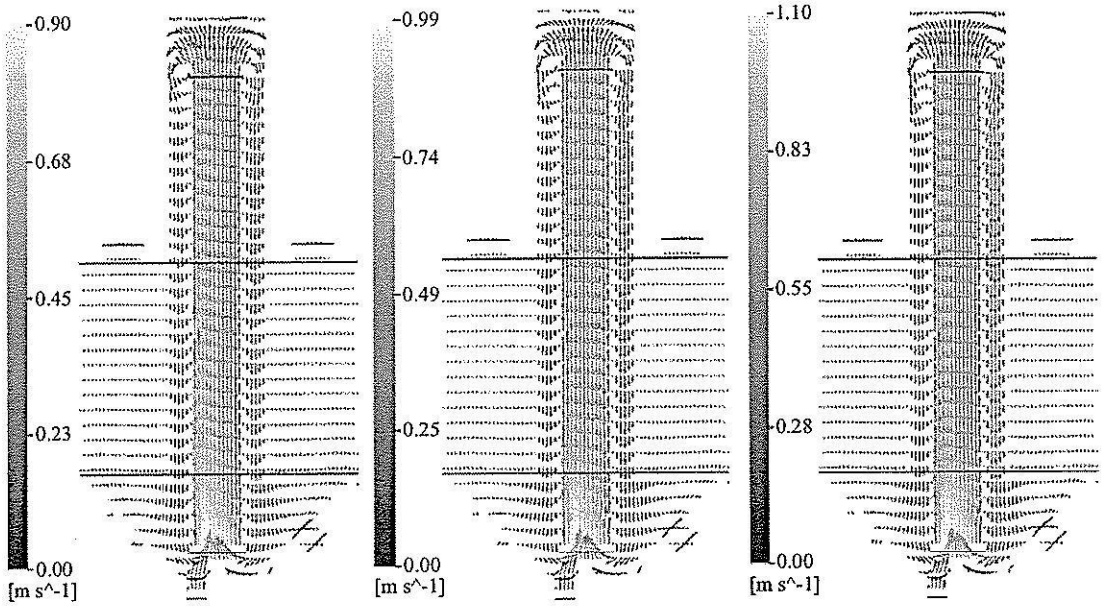

(a) (b) (c)

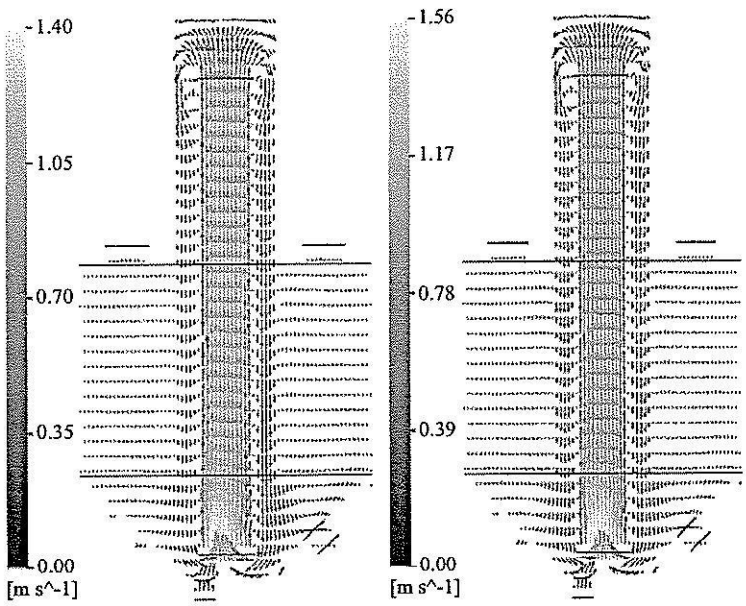

(d) (e)

Fig. 5.5 Liquid velocity vectors in the vertical center plane for momentum source additions of (a) 5.50 kg·m/s^2; (b) 7.85 kg·m/s^2; (c) 11.8 kg·m/s^2; (d) 19.6 kg·m/s^2; (e) 23.6 kg·m/s^2.

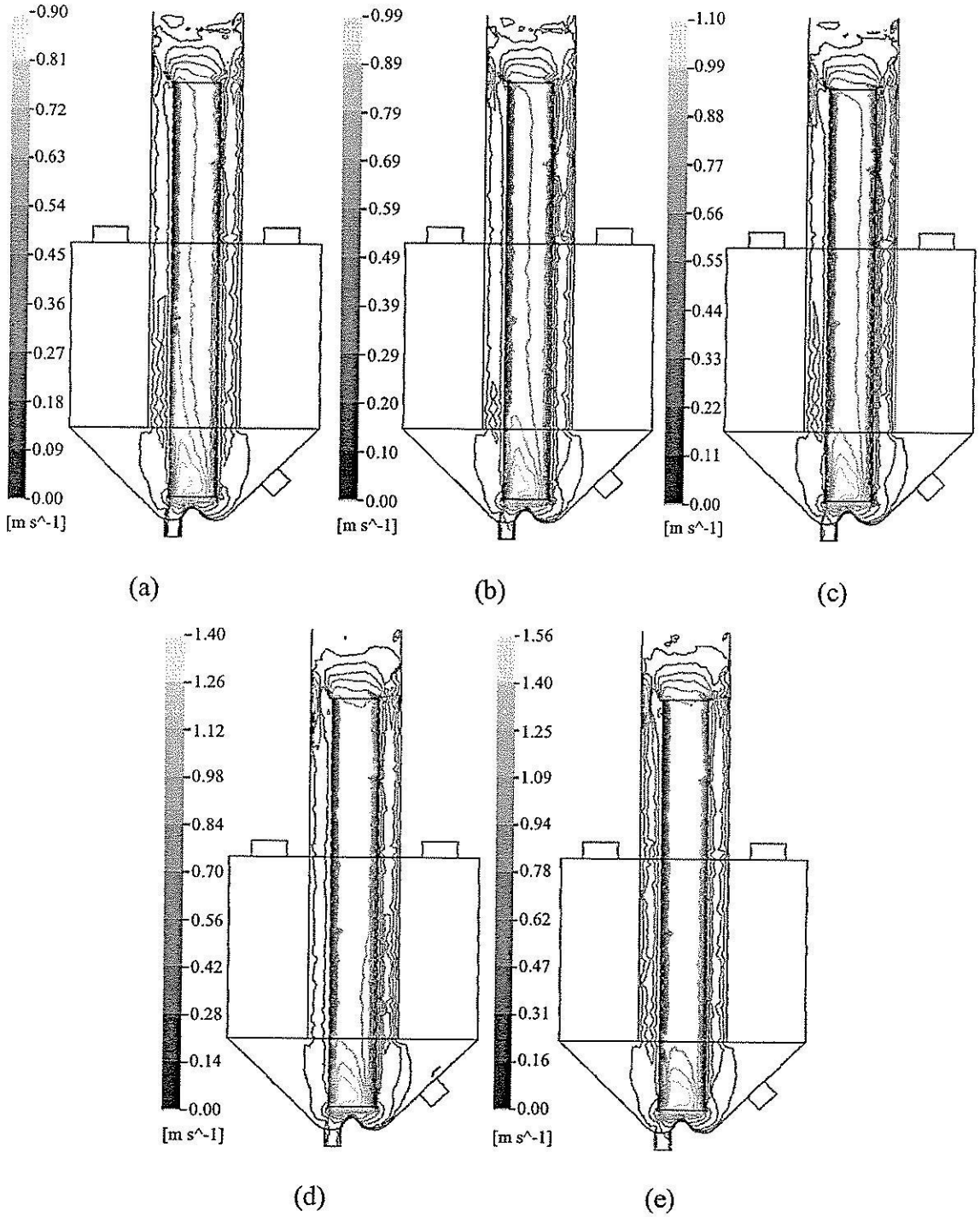

Fig. 5.6 Liquid velocity contours in the vertical center plane for momentum source additions of (a) 5.498 kg·m/s^2; (b) 7.850 kg·m/s^2; (c) 11.78 kg·m/s^2; (d) 19.63 kg·m/s^2; (e) 23.56 kg·m/s^2.

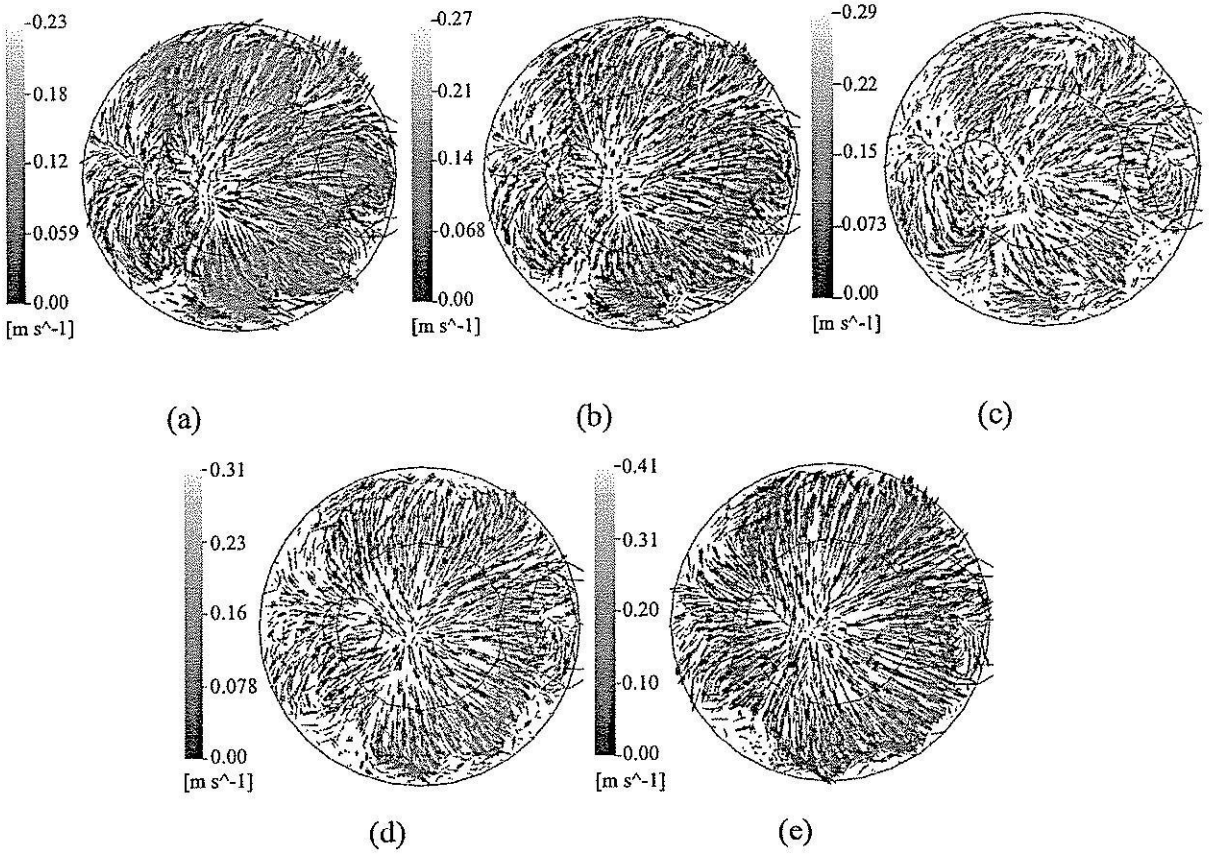

Fig. 5.7 Vapor velocity vectors in the horizontal plane at the vapor-liquid interface for momentum source additions of (a) 5.498 kg·m/s^2; (b) 7.850 kg·m/s^2; (c) 11.78 kg·m/s^2; (d) 19.63 kg·m/s^2; (e) 23.56 kg·m/s^2.

Considering the liquid velocity contours inside and outside the draft tube, it can be seen that the overall flow features are close to uniform at high values of the momentum source addition. Thus it is evident in Figure 8 (for the momentum source values of 7.850, 11.78, 19.63, and 23.56 kg·m/s^2 respectively) that full uniformity is found at the momentum source values of 19.63, and 23.56 kg·m/s^2. This uniform flow occurs from a height of 0.4 m to 1.9 m (at the top of the draft tube) and would assist in producing a narrower crystal size distribution. Uniform flow can lead to the smaller spatial variations in the crystallization rate, in particular a more uniform crystal growth rate, because the level of supersaturation in these areas will be constant. Note that this does not ensure a completely uniform particle size, because there is still a wide distribution of residence times for both the liquid and the crystals in the crystallizer. In addition the residence time distribution of the liquid and the crystals are different because nucleation does not necessarily occur immediately upon the feed entering the crystallizer.

At the vapor-liquid interface, it is seen that at low momentum source additions (momentum source additions of 5.498, 7.850, and 11.78 kg·m/s^2), the vapor will be separated out from the liquid phase in the region from the center of the draft tube to the left side wall of the tank (in the direction of the feed location), as shown in Figures 5.7(a) to (c). This means that momentum source values less than 11.78 kg·m/s^2 are insufficient to cancel the effect of the feed momentum on the flow field in the DTB crystallizer. When the momentum source addition are in the range of 19.63 to 23.56 kg·m/s^2 (Figures 5.7(d) to (e)) all vapor will be separated out only at the center of the tank. This indicates that momentum source values of greater than 19.63 kg·m/s^2 are able to completely cancel the effect of the feed solution momentum on flow field in the DTB crystallizer. There is a transition region between 11.78 and 19.63 kg·m/s^2 where the gas phase is partially separated and flows into both sections of the crystallizer. These values are correct for feed solution flows less than or equal to 1.18 kg/s, which were used in these case studies, in a 1 m^3 crystallizer.

5.1.3 Effect of the fines removal flow rate on the flow characteristics

The overall liquid velocity vectors for the liquid phase for fines removal flows of 0.467, 1.006, 1.545, 2.300, and 3.594 kg/s are shown in Figure 5.8, and velocity contours for the same conditions are shown in Figure 5.9. These figures indicate that for fines removal flows of 0.467, 1.003, 1.545, and 2.300 kg/s the flows of the liquid phase follow the typical flow field in a DTB crystallizer, which are described in a previous section. For a fines removal flow of 3.594 kg/s the flow fields are not typical flow fields in a DTB crystallizer because the momentum source addition of 7.85 kg·m/s^2 is not enough to assist the feed solution to flow into the draft tube (or is not enough to cancel the effect of the fines removal flow pulling the feed in the direction of the settling zone, and the extra momentum in the feed inflow).

As the fines removal flow increases the liquid velocity slightly increases, both in the upflow section inside the draft tube, and in the downflow area in the annular space outside the draft tube. The fines removal flow only slightly influences the overall vapor velocity (Figure 5.8). The flow patterns of the vapor phase have basically the same features without any drastic change in structure, and the other effects of the fines removal flow are the same as described previously (Figure 5.1(b)).

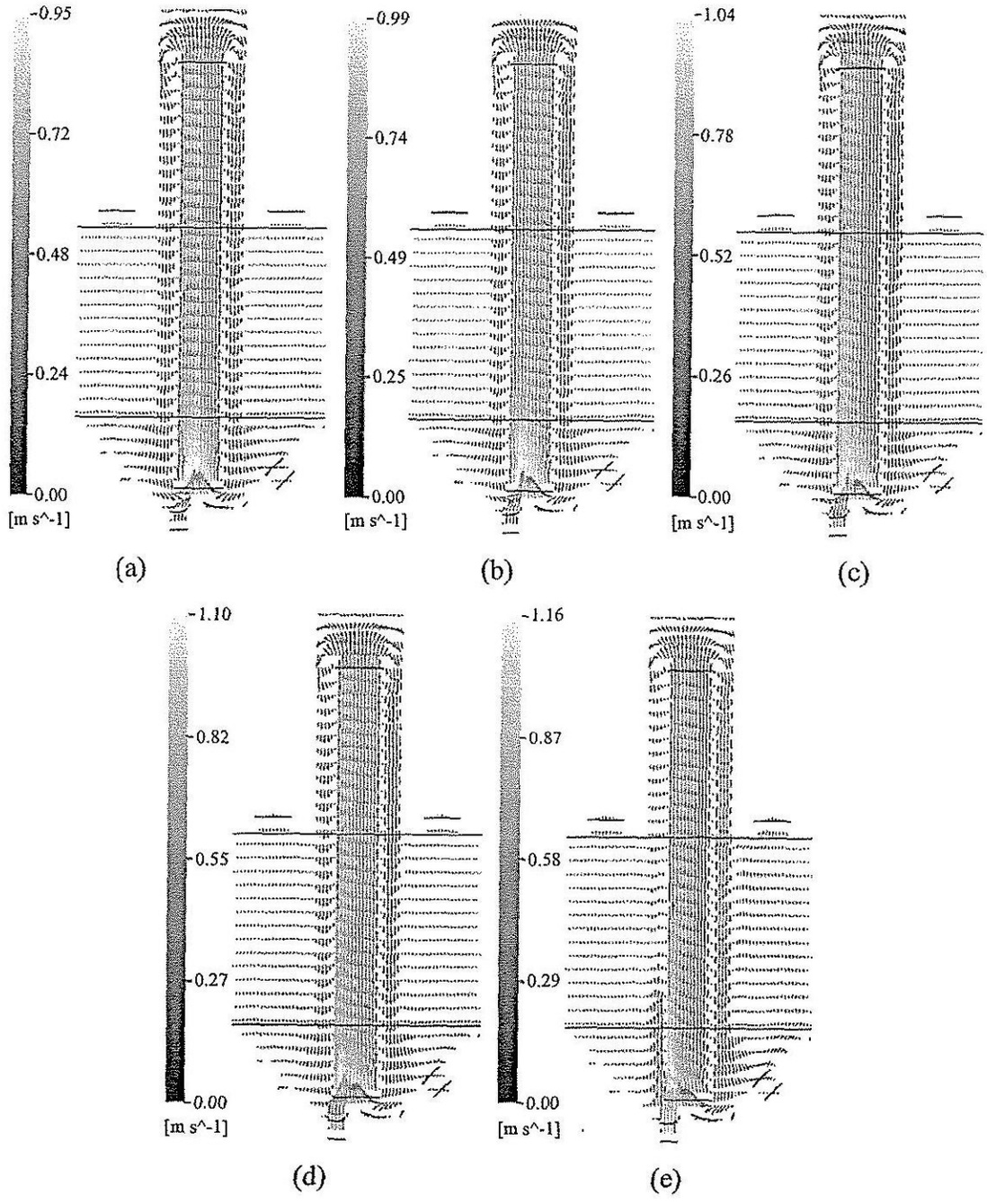

Fig. 5.8 Liquid velocity vectors in the vertical center plane for fines removal flows of (a) 0.4672 kg/s; (b) 1.0063 kg/s; (c) 1.5454 kg/s; (d) 2.3002 kg/s; (e) 3.594 kg/s.

In most fines removal case studies the liquid flow is not uniform (Figure 5.9), except for the fines removal flow of 0.467 kg/s. This is since this low value of the fines removal flow forces the feed solution flow to be very low (the fines removal stream is added to the 'raw' feed to the crystallizer so that small fines removals will also result in low net feed rates), so the rate of momentum source addition used in the case study (7.85 $kg \cdot m/s^2$) completely cancels the effect of the feed flow. At higher fines removal flows the

momentum source addition is not high enough to cancel the effect of the feed flow momentum.

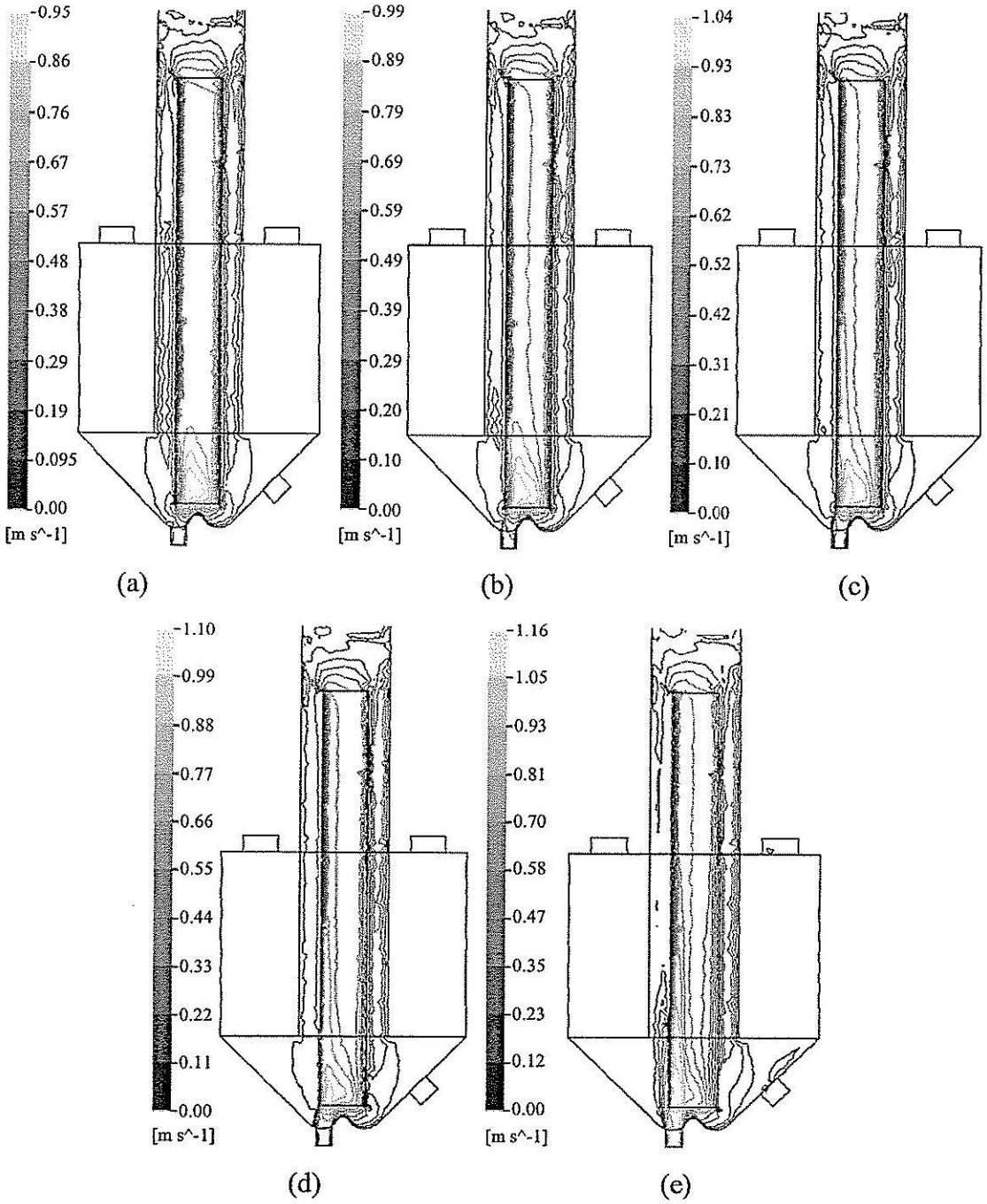

Fig. 5.9 Liquid velocity contours in the vertical center plane for fines removal flows of (a) 0.4672 kg/s; (b) 1.0063 kg/s; (c) 1.5454 kg/s; (d) 2.3002 kg/s; (e) 3.594 kg/s.

Considering the flow features at the vapor-liquid interface, it is seen that at fines removal flows of 1.006, 1.545, 2.300, and 3.594 kg/s, the vapor will be separated out from the liquid phase from the center of the tank to the left side wall of the tank (in the direction

of the feed location); this is shown in Figures 5.10(b) to (e). This indicates that a momentum source value of 7.85 kg·m/s^2 is not enough to cancel the effect of the feed on the flow field in the DTB crystallizer. At the fines removal flow of 0.467 kg/s (for which the feed is equal to 0.6470 kg/s), the majority of the vapor will be separated out from the liquid phase at the center of the tank (Figure 5.10(a)). This indicates that a momentum source value of 7.85 kg·m/s^2 completely cancels the effect of the feed solution flow of 0.467 kg/s or lower.

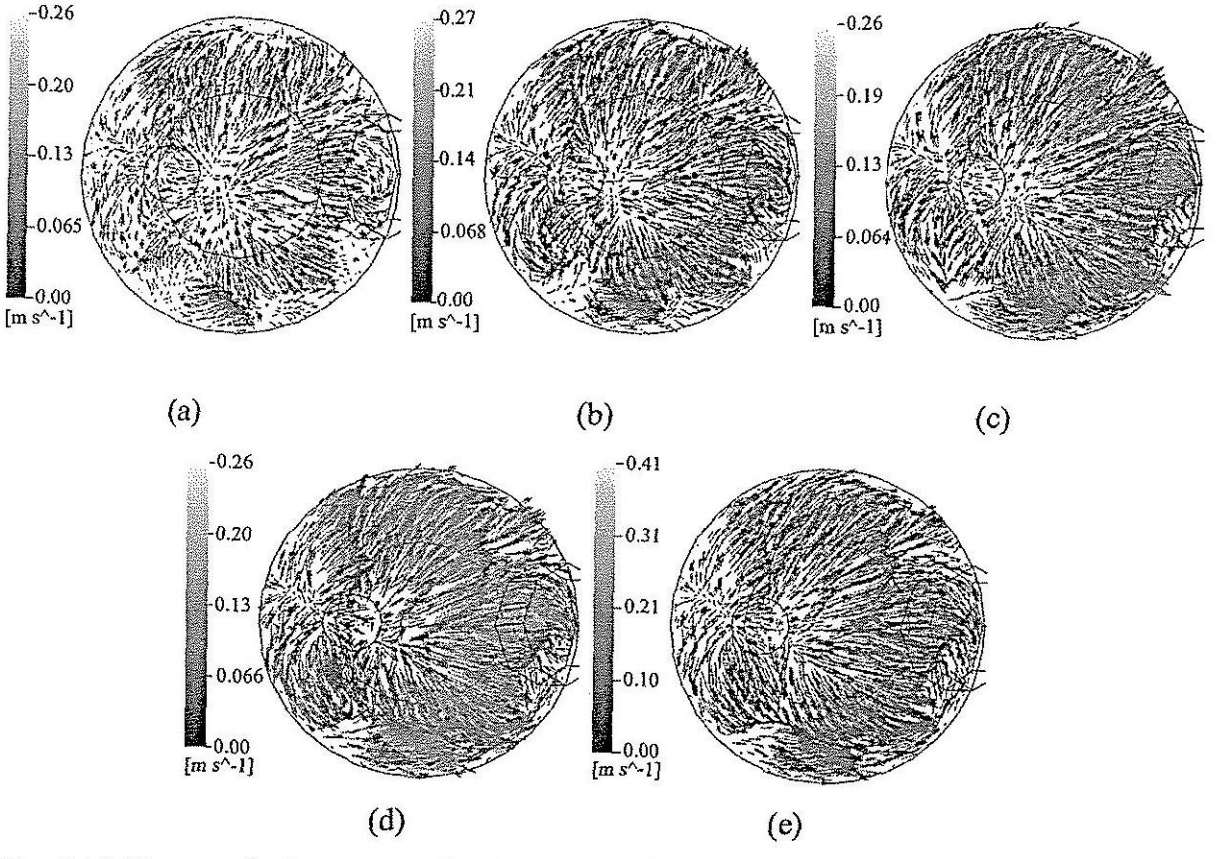

Fig. 5.10 Vapor velocity vectors in the horizontal plane at the vapor-liquid interface for fines removal flows of (a) 0.4672 kg/s; (b) 1.0063 kg/s; (c) 1.5454 kg/s; (d) 2.3002 kg/s; (e) 3.594 kg/s.

5.1.4 The classification of crystals

As described previously, the flow outside the draft tube is downward and the upflow outside the baffle (the annular settling zone) is low enough, and sufficiently uniform, to confirm the gravitational settling process of the crystals. The classification of crystals in this work was studied by analyzing the fines removal cut-size, which was calculated from the free settling velocity, U_t:

$$U_t = \sqrt{\frac{4g(\rho_p - \rho)d_p}{3C_D\rho}} \tag{5.1}$$

where the density of NaCl crystal is 2,155 kg/m^3 (Cheremisinoff, 1986), the C_D of each flow regime is shown Table 2.1 (calculated via the particle Reynolds number, $\mathrm{Re}_p = \rho_c d_p U_t / \mu_c$), and the settling velocity is the predicted value from the simulation, which is the average value of the velocity over the volume in the annular settling zone. Calculation of the fines removal cut-size (d_p) was performed with an iterative calculation since the value of the Reynolds number determines the flow regime. Crystals smaller than the fines removal cut-size will be removed from the crystallizer in the fines removal flows, and crystals larger than this size will settle and leave the crystallizer as product or be re-circulated back into the crystallization zone. Thus, the fines removal cut-size is the minimum size of crystal that would be fully settled in the annular settling zone.

The effects of the power transmitted by the impeller (the effect of the momentum source strength) and the fines removal flow rate on the classification of crystals are shown in Figures 5.11 to 5.13. Figure 5.11 shows that the fines removal cut-size increases with increasing power transmitted by the impeller. This suggests that the mean product crystal size increases with increasing momentum source (although this is not definite since increasing the momentum source may also lead to higher nucleation or attrition rates). This result is due to the varying upflow velocities in the fines removal section since the momentum source affects the flow velocities in the annular space. This will strongly affect the product crystal size distribution. The particle Reynolds numbers increase with increasing power transmitted by the impeller, and all of the values of the Reynolds number are in the lower end of the range of the transition regime for particle flow ($0.3 < \mathrm{Re}_p < 3000$).

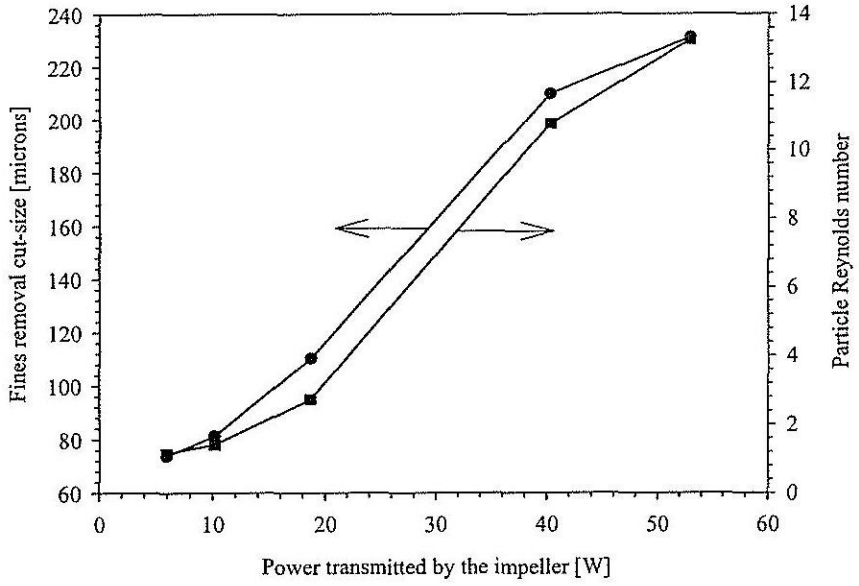

Fig. 5.11 Fines removal cut-size and particle Reynolds number for case studies 1 to 8 as a function of power transmitted by the impeller.

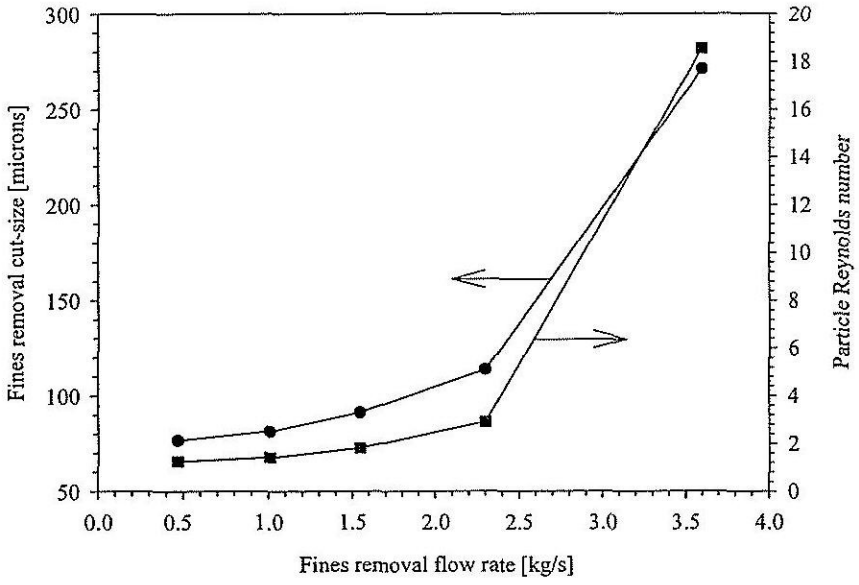

Fig. 5.12 Fines removal cut-size and particle Reynolds number for case studies 9 to 13 as a function of fines removal flow.

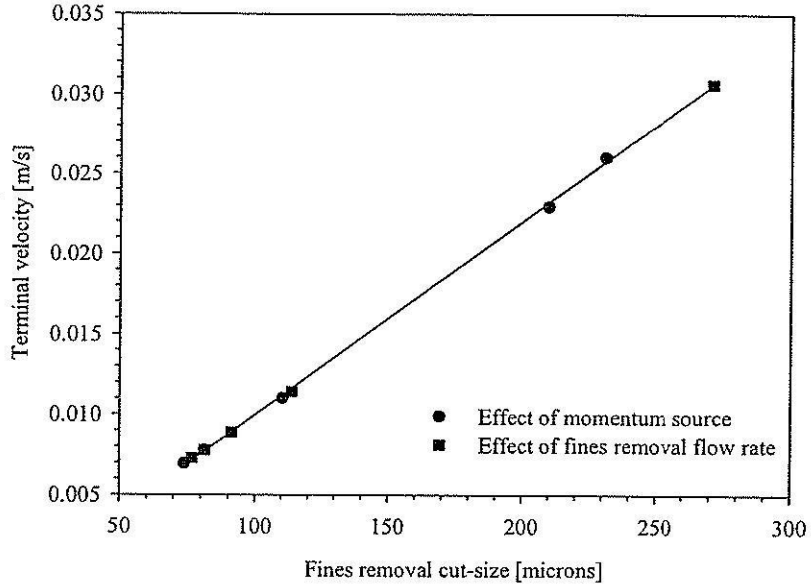

Fig. 5.13 Terminal velocity for case studies 1 to 13 as a function of fines removal cut-size.

Figure 5.12 shows that as the fines removal flow increases (equivalent to increasing the feed solution flow because the product flow is held constant) the fines removal cut-size increases: this agrees well with the experimental results of Eek et al., (1995). This indicates the mean product crystal size increases with increasing fines removal flow. Increasing the fines removal flow also increases the number of fine crystals destroyed in the heat exchanger, thus reducing the total number of crystals in the vessel: from the mass balance for the system it can be seen that this also increases the mean particle size in the system. The particle Reynolds number increases with increasing fines removal flow, and all values of the Reynolds number in the transition regime for particle flow, similar to the experiments which varied the momentum source strength. Figure 5.13 shows the terminal velocity increases approximately linearly with increasing particle size (Figure 5.13); this agrees with the results of Lapple (1951).

5.2 Non-Isothermal Simulations

The main variable investigated in the current study is the effect of the heat source strength on the behavior of the crystallizer. Previous studies on an isothermal model of the crystallizer (with an external heat exchanger assumed, which feeds a two-phase mixture at the saturation temperature into the crystallizer) have already investigated the effect of feed flow rate, product flow rate, fines removal flow rate, and power input via the impeller on

the performance characteristics and flow fields of the crystallizer (Wantha and Flood, 2008).

A significant difference between the two studies (apart from the non-isothermal model containing an internal heat exchanger) is that the liquid surface in the isothermal simulation was modeled using a free surface model, but a degassing condition was used in the non-isothermal simulation to aid convergence of the solution. The fluid flow fields in the two models are expected to be slightly different because the vapor is fed to the crystallizer from an external heat exchanger in the isothermal model, but produced by boiling (mostly near the free surface) in the non-isothermal model, however it was expected that the overall liquid flow vectors would not be significantly altered by this change, and this is shown to be true in Figure 5.14. This indicates that some key conclusions made from the isothermal study will still be valid for the non-isothermal case, particularly the effect of parameters on the velocity in the settling zone, and therefore the predicted fines cut-size (Wantha and Flood, 2008): this is because there is very little difference in the flow fields in the settling zone in the two cases. In the non-isothermal simulation the flow field is more uniform near the base of the draft tube, with less influence of the fluid flowing into the crystallizer body under the left hand side of the impeller.

The main result of the non-isothermal simulation is the effect of the heat source on the evaporation rate, which can be used to predict crystallization rates. Other flow field parameters, particular the flow near the free surface where boiling occurs, are also strongly affected by the heat addition rate. In this study, four test cases are performed, using a constant momentum source addition of 10,000 $kg/m^2/s^2$, feed solution flows of 1.18608 kg/s and product suspension flows of 0.1797 kg/s, with the heat source values varying at 11,000, 12,000, 13,000, and 13,500 kW/m^3. Note that the heat source is the heat input per unit volume (with the volume of the sub-domain equal to 0.0007854 m^3) so that the heat input values of these heat source values are 8.64, 9.42, 10.21, and 10.60 kW, respectively.

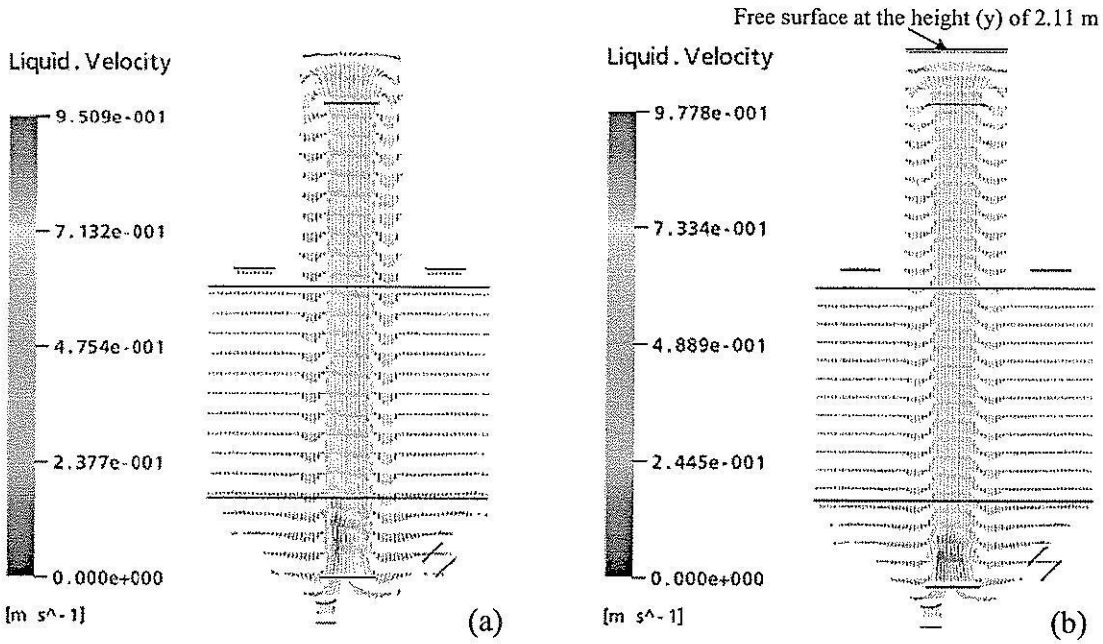

Fig. 5.14 Liquid flow fields in the crystallizer for (a) the isothermal simulation with an external heat exchanger; (b) the non-isothermal simulation with an internal heat exchanger.

The CFD results showed that the vapor formed linearly increases with increasing heat input (Figure 4). This can be shown to be true by the overall energy balance around the crystallizer (neglecting the small heat of crystallization):

$$\dot{m}_F H_F + \dot{Q}_{to} + \dot{W}_{to} = \dot{m}_{Fines} H_{Fines} + \dot{m}_p H_p + \dot{m}_v H^{sat.vap.} \tag{5.2}$$

In this work, the temperature of the feed solution is 379 K, which is near the boiling point of the solution (380.6 K) and the heat added to the system is used to evaporate a relatively small fraction of the solution to induce crystallization, so that the temperature of the solution at the fines removal outlet and product crystals outlet are constant at the saturation temperature. This enables the energy balance to be simplified to

$$\dot{m}_v = \frac{\dot{W}_{to} + \dot{m}_F\left(H_F - H^{sat.sol.}\right)}{L} + \frac{\dot{Q}_{to}}{L} \tag{5.3}$$

Substitution of the relevant constants in this equation results in the linear response

$$\dot{m}_v = 0.00045\dot{Q}_{to} - 0.0035 \tag{5.4}$$

This equation is compared to the vapor production in the crystallizer in Figure 5.15.

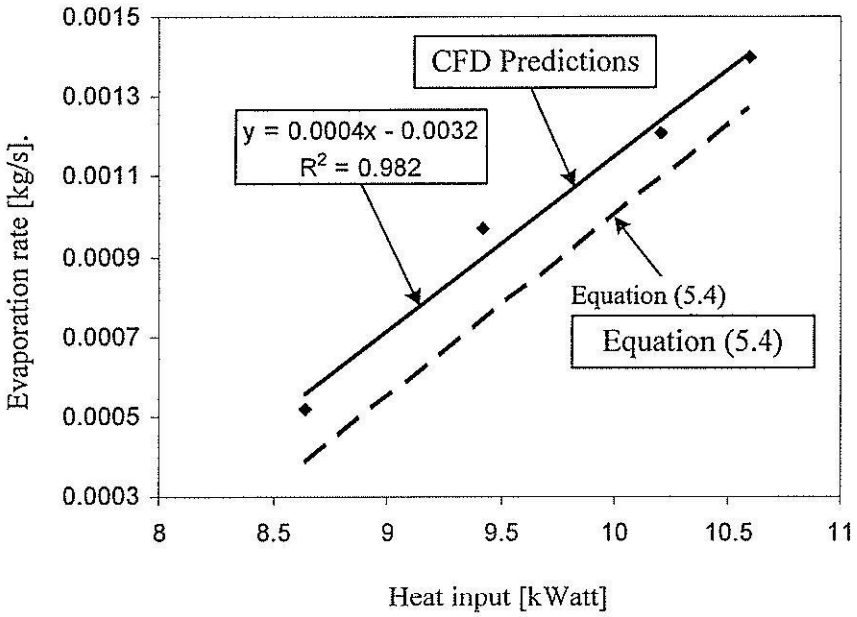

Fig. 5.15 Evaporation rate in the crystallizer as a function of the heat input for both the non-isothermal simulation and the simplified energy balance around the crystallizer.

There are only small temperature gradients noticeable in the solution to the non-isothermal simulation, with the largest gradient being near the feed inlet, as the feed is slightly subcooled. This low temperature fluid is noticeable underneath the left hand side of the draft tube, at the feed inlet, and continues a short distance past the impeller: the fluid being drawn into the right hand side of the impeller is fluid being recirculated from the body of the crystallizer, which is very close to the saturation temperature. Temperature gradients in a real crystallizer might be more than shown here due to heat losses from the body of the crystallizer, which has not been modeled in the current simulations.

Another interesting aspect of the simulation results is the analysis of the vapor volume fraction, as shown in Figure 5.16. The results show that boiling occurs near the free surface, and also at the top edge of the draft tube: this must be due largely to the pressure variations in the crystallizer since the temperature variation is quite low. The static

pressure is the main component of the pressure variation in the crystallizer, and of course this is a minimum near the free surface.

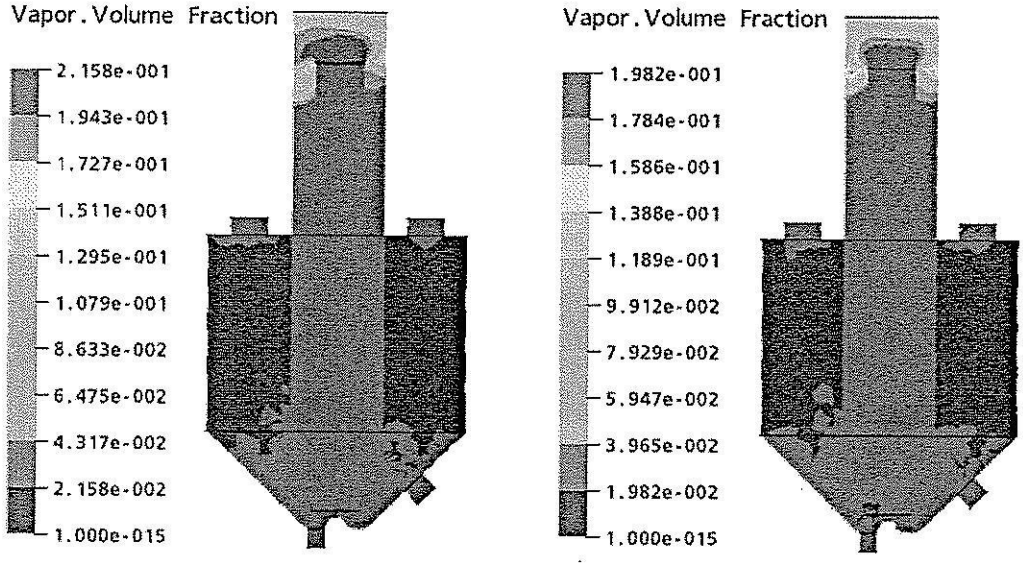

Fig. 5.16 Profiles of the vapor volume fraction in the non-isothermal simulation for heat source additions of (a) 13,000 kW/m^3; (b) 13,500 kW/m^3.

The flow near the free surface of the crystallizer is quite complex, and liquid and vapor have very different flow fields in the area between the top of the draft tube and the free surface. This is illustrated in Figure 5.17. A significant amount of the vapor is produced near the top edge of the draft tube, and this vapor is carried out towards to wall of the crystallizer and then up to the free surface where it exits due to the degassing condition. The liquid, on the other hand, has a strong recirculation loop, where much of the liquid exiting the draft tube falls over the edge of the draft tube into the annular space, while a smaller portion of the liquid is forced into the region above the draft tube into a recirculation loop.

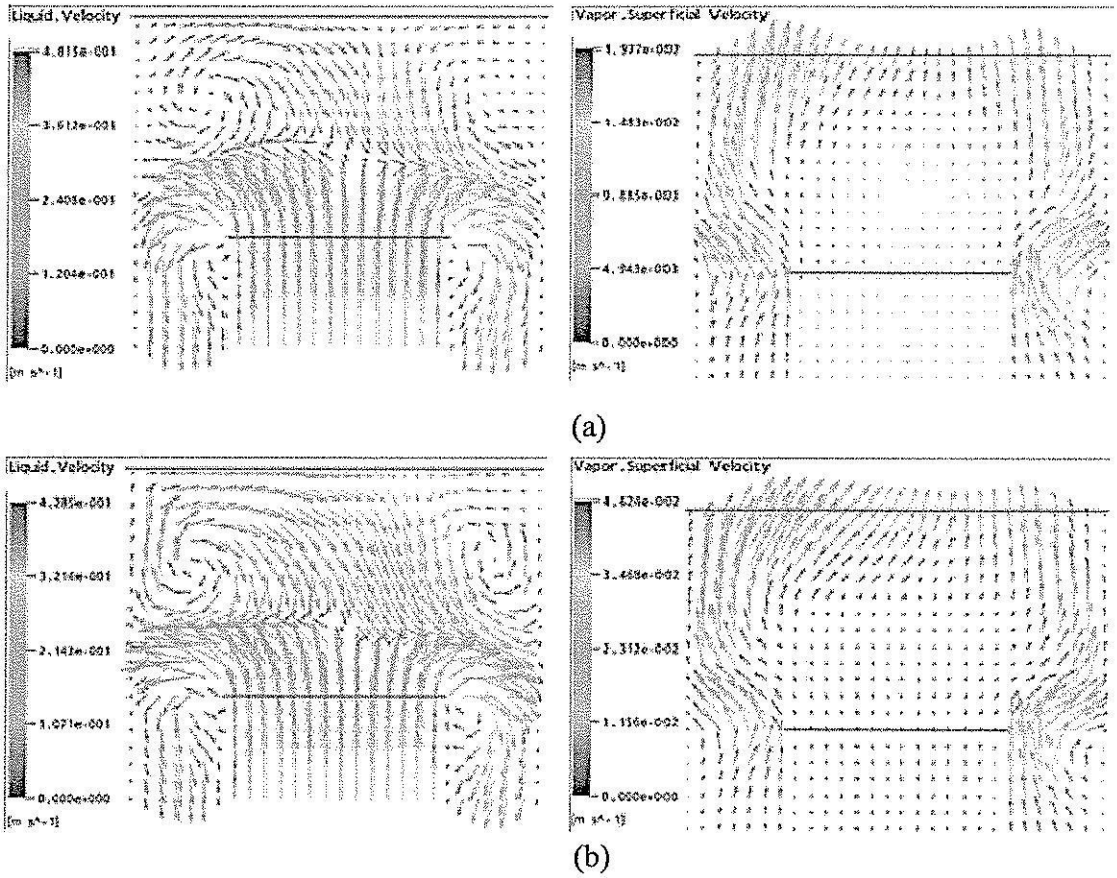

Fig. 5.17 Liquid and vapor velocity vectors at the top of draft tube for heat source additions of (a) 11,000 kW/m^3; (b) 12,000 kW/m^3.

The results discussed here are presented in brief; much more information can be found in the thesis of Wirapong Wantha (2008).

Chapter VI

Methods for the Vacuum Pan Crystallizer

Batch vacuum pan crystallizers are used as the primary crystallizer in the sugar industry. Hot sugar cane juice from multiple effect evaporators is fed into the vacuum pan which has a significant vacuum to lower the boiling point of the juice (which is very high due to boiling point elevation of the sucrose-rich juice), and steam heating to cause evaporation. Steam heating occurs in a section called a calandria, which is typically as set of vertical pipes through which steam passes. Evaporation using steam in the calandria continues until the sugar syrup is at a saturated condition, whereupon seed crystals (in the size range of 10 micrometers) are added to initiate the crystallization. Crystallization continues by evaporation until the suspension of crystals is sufficiently dense that the system must be stopped, and the crystals and remaining mother liquor discharged from the base of the pan.

6.1 Geometry and Design of the Vacuum Pan

Vacuum pans are usually vertically mounted units with a circular cross section. In the base of the unit there is a heat exchanger (similar to a shell and multiple tube heat exchanger) which is called a calandria. Superheated steam flows inside the calandria to cause heat transfer inside the vaccum pan which is responsible for evaporating water from the syrup. Typically there is no agitator in a batch vacuum pan; circulation of the syrup in the pan is provided by the hot juice rising through the calandria, and then falling again as it cools.

The vacuum pan modeled is based on that in Figure 6.1. The total (juice) capacity of the pan is 60 ton, leading to a pan diameter of 5 m. The calandria involves vertical tubes of total length 600 mm, and a tube diameter of 100 mm. The total number of tubes in the calandria (1000) gives a heat exchange area of around 200 m^2. The strike height (the level above the top tube plate) in the pan is 1.4 m. These are typical values for industrial vacuum pans of this size. General features of designs can be seen on the website www.sugartech.com/vacuumpans/batchpan.php.

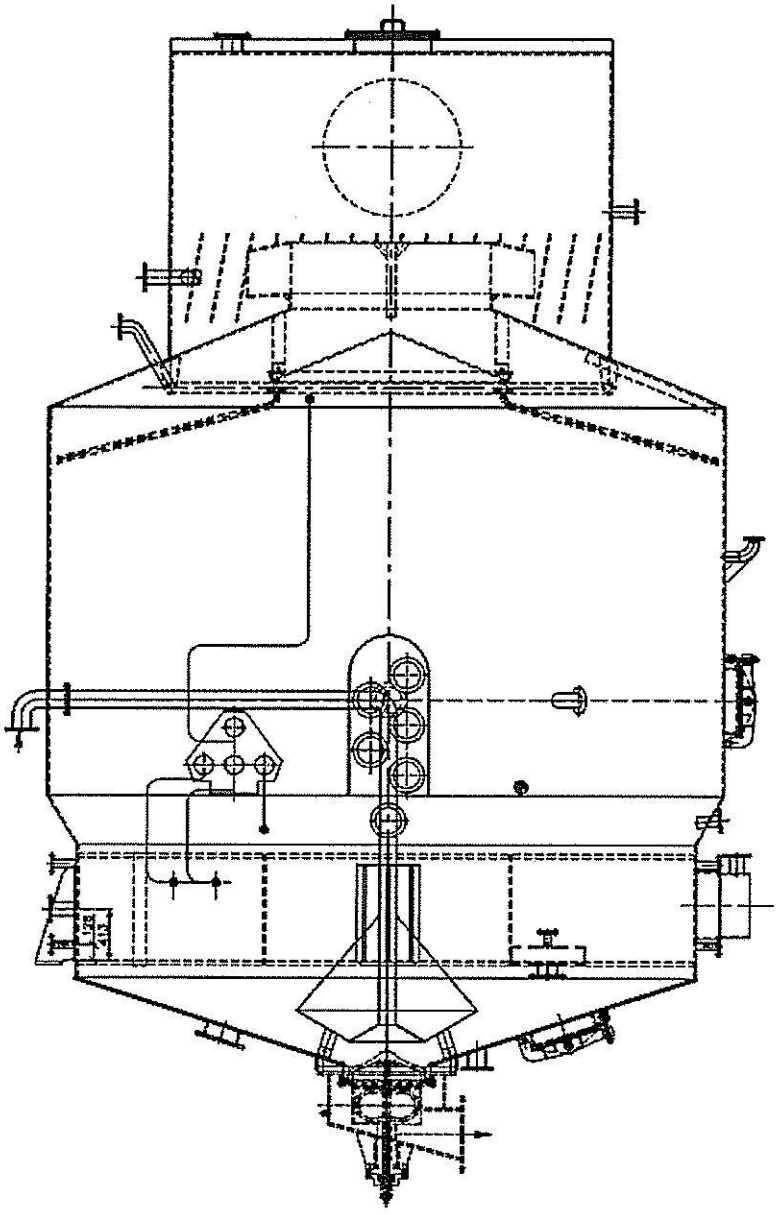

Fig. 6.1 A batch vacuum pan crystallizer. (http://rachitech.com/BOILING_HOUSE). A typical capacity for the pan is 60 ton, although pans range between 25 and 140 ton.

The heat transfer coefficient is assumed to be 570 W/m^2K, based on analysis by Rein (2004) of large number of pans with natural circulation of the juice. With circulation provided by agitators this value may increase to as large as 640 W/m^2K. These are heat transfer coefficients assumed near the beginning of a batch crystallization. As the crystallization continues the amount of crystal in suspension increases, and thus the apparent viscosity of the suspension increases, which reduces the effectiveness of the heat transfer. Towards the end of batch crystallizations the heat transfer coefficient may be as

low as 32 W/m^2K in natural circulation vacuum pans. The current modeling will be performed at a state near the beginning of the batch where the heat transfer coefficients are larger.

In this work the batch vacuum pan crystallizer geometry will be created by the program DesignModeler in ANSYS Workbench v.10.0, as for the DTB crystallizer.

6.1.1 Mesh Generation

In this work the mesh will be created by the program CFX-Mesh in ANSYS Workbench v.10.0. The first step in mesh creation is to create composite 2D regions to specify locations in CFX-Mesh and define boundary conditions in CFX-Pre. These regions include the baffles, calandria surfaces, and tank walls (the remaining outside walls) (see Figure 6.1).

The final step before the physics definition is to create the mesh, which was created by the program CFX-Mesh in ANSYS Workbench v.10.0. ANSYS CFX-10.0 uses the finite volume solution technique with an unstructured mesh. Initially the program creates a 2-D mesh on the boundaries of the crystallizer geometry, and then this mesh is extrapolated into the body of the geometry. The volume of the crystallizer tank is broken into a set of discrete subdomains, computational cells, or control volumes using a grid, or mesh. The mesh can contain elements of many shapes and size. The points of intersection of the lines that make up the sides of the elements are referred to as nodes. In CFX-Mesh, 3-D elements are usually tetrahedral (with four sides), prisms (with five sides), pyramids (with five sides), and hexahedra (with six sides). The meshing will be performed in an identical way as for the DTB crystallizer; see Section 4.3.2.

6.2 Physical and Thermal Properties of Sucrose Solutions

There are a large number of physical and thermal properties required for the fluid phases for CFD simulation to be used. There are two fluid phase present in this work; the first is the water vapor produced by the evaporation. This is equivalent to that produced in the DTB evaporative crystallizer, and the same properties for this phase will be assumed here (refer to Table 4.5). The liquid phase properties depends on the temperature of the phase, the sugar concentration in the phase, and also the concentration of crystals in the suspension. These parameters may vary throughout the batch pan, and so it is not suitable

to model them using a single value. Table 6.1 (from Semlali et al., 2001) gives correlations for these variables as a function of the conditions of the fluid or suspension.

Table 6.1 Properties of Sucrose Solutions (Semlali et al, 2001).

Designations	Expression of the correlation	Units	Reference
Density of massecuite	$1/\rho_m = 1/\rho_c\ Cr + 1/\rho_{sol}\ (1-Cr)$	(kg/m^3)	Bubnik et al., 1995; Koiranen et al., 1999
Dynamic viscosity of massecuite	$\log \eta_m = \log \eta_{sol} + 0.01326\ Bx_m\ [0.85/(0.85-Cr)-1]$	(Pa.s)	Kadlec, Bretschneider & Dandar, 1981; Bubnik et al., 1995
Dynamic viscosity of solution	$\log \eta_{sol} = 22.46$ $\beta - 0.114 + (30 - T_{sol})/(91 + T_{sol})\ (1.1 + 43.1\beta^{1.25}\chi)$ with: $\beta = Bx_{cor}/1900 - 18\ Bx_{cor}$ $Bx_{cor} = Bx_{sol}\ (\gamma + (1-\gamma)\ P_{sol}/100)$ $\chi = 0.85 + 0.15\ P_{sol}/100\ \gamma = 0.915$	(Pa.s)	Noël, 1990; Bubnik et al., 1995; Peacock, 1995 Noël, 1990
Specifics heat capacity and enthalpy of massecuite	$Cp_m = Cp_c Cr + Cp_{sol}(1-Cr)\ h_m = h_c Cr + h_{sol}(1-Cr)$	(kJ/kg.°K)(kJ/kg)	Kadlec, et al., 1981; Azevedo et al., 1994
Latent heat of water vaporization	$h_v = 600.54 + 0.3891\ T_b - 0.7013\ Pr$	(kJ/kg)	Cuel & Longue-Epee, 1984
Boiling point elevation	$\Delta T_b = 0.012\ (T_b + 84)\ Su/W + 0.03\ (T_b + 84)\ NS/W$	(°C)	Maurandi, 1975
Sucrose solubility	$Y = 64.47 + 0.10336\ T_{sol} + 14.24 \times 10^{-4}\ T_{sol}^2 - 60.2 \times 10^{-7}\ T_{sol}^3$	(g sucrose/ 100 g of solution)	Genetolle, 1984
Saturation coefficient	$K_{sat} = 0.178\ (NS/W) + 0.820 + 0.180 \exp(-2.1\ (NS/W))$		Bubnik et al., 1995
Diffusivity of sucrose	$D = 1.665 \times 10^{-15}\ (T_{sol} + 273)/\eta_{sol}$	(m^2/s)	Noël, 1990
Relative velocity of particles in suspension	$u = (0.065\ (\rho_c - \rho_{sol})\ g\ MA^2/\eta_{sol})\varepsilon^{5.1}$	(m/s)	Koiranen et al., 1999
Porosity	$\varepsilon = 1 - [Cr/\rho_c]/[Cr/\rho_c + (1-Cr)/\rho_m]$		

6.3 CFD Modeling of the Vacuum Pan

6.3.1 Boundary Conditions

The crystallizer being modeled is a batch crystallizer, so there are no boundary conditions required except for the zero-slip condition on the walls of the equipment, and the outside of the tubes of the calandria. The use of boundary conditions in the program CFX 10.0 is described in the section on the DTB crystallizer.

6.3.2 Flow Conditions

Flow conditions for simulation equivalent to those for the non-isothermal simulations for the DTB crystallizer. The flow in a vacuum pan crystallizer is such that there is significant temperature variation in the pan, and an isothermal simulation is therefore not able to give a sufficiently accurate model of the system. The assumptions for the isothermal simulations are those used for the DTB crystallizer, described in Section 4.3.3, but with properties of sucrose, taken from table 6.1. The theory for the simulations is already described in the section on Non-isothermal simulation in Chapter 3.

Note that although the geometry and methods used in the simulation of the sugar vacuum pan crystallizer have been developed in this research, in the third year of the research funding the total amount of the grant awarded to the project was 110,000 Baht, which was not sufficient for even purchasing a minimum user (10-user) yearly user license for the CFD software (which was 125,000 Baht at that time). For this reason these simulations could not be performed.

Chapter VII

Summary

The study has shown that it is possible to use CFD to study complex processes in the Chemical Process Industries at a level whereby the process may be analyzed and the design improved upon in order to optimize some features, such as uniformity of supersaturation, uniformity of particle size distribution, or effectiveness of the fines distribution. However in order to achieve this the models used must be entirely comprehensive (correctly modeling continuity, momentum and heat transfer correctly, at least!), and the mesh used must be sufficiently small so that an accurate picture of the process results. This may result in rather long processing times for models of many current systems!

The current study did not look at the flow of the crystal phase in much detail, assuming a Langrangian viewpoint where the details of the crystal flow were required. The models also did not deal with the growth or nucleation of the crystal phase, or mass transfer to or from the crystal phase. This was because the knowledge of such mechanisms still cannot be achieved by CFD alone. Key parameters in nucleation and crystal growth must still be obtained from accurate experimental data recorded under the conditions of interest. Such experiments are costly and time consuming, and were not in the scope of the current study.

Although simulations were designed for a particular batch vacuum pan sugar crystallizer, and models were made based on the physics of the problem (similar as to those in the DTB crystallizer case), as well as boundary conditions being analyzed, it was not possible to carry out detailed simulations due to a lack of funding for the CFD tools in the last year of the grant, which was very unfortunate.

An international journal article (with an SCI Impact Factor) has been published from the research (Wantha and Flood, Numerical Simulation and Analysis of Flow in a DTB Crystallizer, Chem. Eng. Comm. 195, 1345-1370, 2008). In addition, a peer reviewed international conference paper (printed in a published book of proceedings) was also published (Flood and Wantha, Computational Fluid Dynamic Modeling of a 1 m^3 Draft Tube Baffle Crystallizer with Fines Removal, 13th International Workshop on Industrial Crystallization, Ed. Jansens, ter Horst, and Jiang (2006); IOS Press, The Netherlands (ISBN 1-58603-658-0). These articles are attached.

References

1. ANSYS Canada Ltd. (2005). ANSYS CFX-10.0 Manual.
2. Chung, T. J. (2002). Computational fluid dynamics. Cambridge, United Kingdom: Cambridge University Press.
3. Cheremisinoff, N. P. (1986). Handbook of heat and mass transfer; V2: Mass transfer and reactor design. Honston, Taxas: Gulf publishing company.
4. Deen, N. G., Solberg, T., and Hjertager, B. H. (2002). Flow generated by an aerated Rushton impeller: Two-phase PIV experiments and numerical simulation. The Canadian Journal of Chemical Engineering 80: 1-15.
5. Flood, A. E. (2009). Industrial Crystallization from Solution: A Primer. Suranaree University of Technology, Nakhon Ratchasima, Thailand.
6. Hughmark, G. (1967). Mass and heat transfer from rigid sphere. AIChE Journal 13:1219-1221.
7. Ishii, M. and Zuber, N. (1979). Drag coefficient and relative velocity in bubbly, droplets or particulate flows. AIChE Journal 25(5):843-855.
8. Jakobsen, H. A., Sannaes, B. H., Grevskott, S., and Svendsen, H. F. (1997). Modeling of vertical bubble-driven flows. Industrial Engineering Chemistry and Research 36: 4052-4074.
9. Kramer, H. J. M., Dijkstra, J. W., Neumann, A. M., Meadhra, R. Ó., and van Rosmalen, G. M. (1996). Modeling of industrial crystallizers, a compartmental approach using a dynamic flow-sheeting tool. Journal of Crystal Growth 166: 1084-1088.
10. Lapple. C. E. (1951). Fluid and Particle Mechanics 1st Edition. University of Delaware.
11. Lopez de Bertodano, M. (1995). Turbulent bubbly flow in triangular duct. Ph.D. Thesis, Rensselare Polytechnic Institute; Troy New York.
12. Maqableh, A., Simmons, K., Hibberd, S., Power, H., and Young, C. (2003). CFD modelling of three-component air/oil flow and heat transfer in rotating an-nualus. In The Eleventh Annual Conference of the CFD society of Canada. Tenue ́a Vaconner,Canada.
13. Maude (1958). Cited in Chemical engineers' handbook, Perry, R. H. and Green, D., McGraw-Hill, New York, 1984, pp. 5-66.

14. McCabe, W. L., Smith, J. C., and Harriott, P. (2001). Unit operations of chemical engineering (6th ed.). Singapore: McGraw-Hill.
15. Mersmann, A. (2001). Crystallization technology handbook (2nd ed.). New York: Marcel Dekker.
16. Micale, G. and Montante, G. (1999). On the simulation of two-phase solid-liquid stirred vessels. In The Fith CFX International User Conference. Friedrich-shafen, Germany.
17. Mullin, J. W. (2001). Crystallization (4th ed.). Oxford: Butterworth-Heinemann. Myerson, A. E. (2002). Handbook of industrial crystallization (2nd ed.). USA: Butterworth-Heinemann.
18. Oey, R. S. (2005). Gas-liquid flows in a two-fluid formalism: modeling and validation of closure relations. PhD Thesis, Delft University of Technology; The Netherlands.
19. Paul, E. L., Atiemo-Obeng, V. A., and Kresta, S. M. (2004). Handbook of industrial mixing: Science and practice. New Jersey: John Wiley & Sons.
20. Pericleous, K. A. and Patel, M. K. (1987). The source-sink approach in the modeling of stirred reactor. PCH Physiochemical Hydrodynamics 9:279-297.
21. Perry, R. H. and Green, D. W. (1997). Perry's chemical engineers' handbook (7th ed.). New York: McGraw-Hill.
22. Randolph, A. D. and Larson, M. A. (1988). Theory of particulate processes: Analysis and techniques of continuous crystallization (2nd ed.). California: Academic Press.
23. Rein, P. W., Echeverri, L. F., and Acharya, S. (2004). Circulation in vacuum pans. Journal American Society of Sugar Can Technologists 24: 1-17.
24. Sato, Y. and Sekoguchi. K. (1975). Liquid velocity distribution in two-phase bubble flow. International Journal of Multiphase Flow 2: 79-95.
25. Schiller, L. and Naumann, A. (1933). VDI Zeits 77: 318.
26. Semlali, N., Hassani, A., Saidi, K. and Bounahmidi, T. (2001). Steady state modeling and simulation of an industrial sugar continuous crystallizer. Comp. Chem. Eng. 25: 1351-1370.
27. Sha, Z. and Palosaari, S. (2000). Size dependent classification function in imper-fectly mixed suspension continuous crystallizer. Mixing and Crystallization (pp. 133-149). Netherland: Kluwer Academic Publishers.
28. Wantha, W. Computation Fluid Dynamics Simulation of a DTB Crystallizer. M.E. Thesis, Suranaree University of Technology; Thailand.

29. Wantha, W. and Flood, A. E. (2008). Chem. Eng. Comm. 195: 1345-1370.

30. Yang, W. (2003). Handbook of fluidization and fluid-particle system. New York: Marcel Dekker, Inc.

Chem. Eng. Comm., 195:1345–1370, 2008

ISSN: 0098-6445 print/1563-5201 online
DOI: 10.1080/00986440801963527

Taylor & Francis
Taylor & Francis Group

Numerical Simulation and Analysis of Flow in a DTB Crystallizer

WIRAPONG WANTHA AND ADRIAN E. FLOOD

School of Chemical Engineering, Institute of Engineering, Suranaree University of Technology, Nakhon Ratchasima, Thailand

This research numerically simulates the two-phase (liquid and vapor) flow in a 1 m^3 draft tube baffle (DTB) crystallizer with fines removal streams. The computational fluid dynamics (CFD) commercial software ANSYS CFX-10.0 was employed to perform 3-D simulation using the finite volume method with an unstructured mesh topology. The influence of hydrodynamics in the crystallizer, as characterized by the momentum source strength and fines removal flow, on the flow characteristics and the classification of crystals are investigated. The results showed the liquid flow is fully uniform in the main body of the crystallizer studied for momentum sources larger than or equal to 19.63 $kg \cdot m/s^2$. The uniformity of the suspension will strongly affect the product crystal size distribution. Momentum source strengths and fines removal flow rates also have a significant effect on the fines removal cut-size due to varying up-flow velocities in the fines removal section, altering the size at which particles are carried out in the fines removal stream. The CFD predictions are compared with the experimental results from the literature and can be used for the optimization of commercial-scale DTB crystallizer design.

Keywords Computational fluid dynamics (CFD); Draft tube baffle (DTB) crystallizer; Multiphase flow

Introduction

Crystallization is a separation and purification process widely used in the process industry. In most commercial processes, both the ease of separation of the product and the commercial value of the product increase with an increase in crystal size. The prediction of the crystal size distribution (CSD) is an important part of crystallizer design. The CSD is commonly modeled by population balance equations, as a function of process conditions, crystallizer layout, and type of crystallization process. This equation is also used to describe the crystal population distribution dynamics. Unfortunately, in industrial crystallizers, conditions such as the fluid shear, concentration, and temperature vary strongly according to the position in the vessel, meaning that the parameters in the population balance are not constant throughout the vessel; this means that it is not possible to accurately model an industrial crystallizer using the population balance unless the fluid flow/heat transfer/mass transfer conditions are known in advance so that kinetic rates (nucleation, crystal growth,

Address correspondence to Adrian E. Flood, School of Chemical Engineering, Institute of Engineering, Suranaree University of Technology, 111 University Ave., Muang District, Nakhon Ratchasima 30000, Thailand. E-mail: adrianfl@sut.ac.th

and other phenomena) in the process can be estimated as a function of spatial position.

Uniformity of crystal size (a narrow CSD) is an important factor in manufacturing processes and the market. Poor CSD causes problems in manufacturing processes, particularly in separation of the product from the mother liquor. Too large crystal size may result in crystals settling to the bottom of the tank and agglomerating. Wide CSD also causes marketing problems, such as when the crystal sizes are not in the desirable range, resulting in a low-quality product, which reduces the sale price or requires additional post-processing to separate and classify.

Many industrial crystallizers are of the draft tube baffle (DTB) crystallizer type. The main advantages of the DTB crystallizer are that it is able to produce a "single crystal" product with a large median size and a narrow size distribution, gives little change in product size with respect to changes in throughput, has low operating costs, and is simple to operate, start up, and shut down (Svenson Technology, 2002). The DTB crystallizer studied here is a combination of a mixed-suspension mixed-product removal (MSMPR) crystallizer (the crystallization zone) and a classifier. The classifier is employed to remove some fraction of particles of less than a given size from the crystallizer vessel; it is a particle settling zone from which fine particles can be removed. The most common use of this crystallizer type is as evaporative crystallizer with materials having the solubility slightly increasing, remaining constant, or even decreasing with increasing temperature. The DTB crystallizer produces large single crystals and narrows their size distribution for easier drying and less caking. Theoretical models of crystallization assume a perfectly mixed suspension in the crystallization zone, but the validity of this assumption is sensitive to the mixing intensity and the mechanical configuration of the crystallizer vessel. In the classifier zone, a large cross-sectional area with a low fines removal flow rate leads to a low upward velocity. This low velocity leads the classifier to act as a settling zone in which small crystals are separated from larger crystals by gravitational forces (Neumann, 2001).

In the DTB crystallizer, the evaluation of the impact of processing variables (such as impeller speed, fines removal flow rate, feed flow rate, and others) on the crystallization and particle settling processes can be determined using computational fluid dynamics (CFD) modeling tools. In particular, the effect of the fluid dynamics in the process on the crystallization rate (which relates to both the rate of nucleation and the rate of crystal growth) is not completely understood, but it is critical to the accurate design of the crystallizer. The crystallization rate is an important determinate of the necessary crystallizer volume required for a particular throughput, and if it is predicted incorrectly, the product crystal size may be considerably different than the value in the design criteria.

CFD is a body of knowledge and techniques to solve mathematical models of fluid dynamics on digital computers; it is used to obtain solutions for single or multiphase flow analysis, temperature distribution, and distribution of chemical composition, through solutions of the equation of continuity and equations describing momentum transfer, heat transfer, mass transfer, phase change, and chemical reaction. There is a large body of literature concerning the use of CFD to model chemical processing equipment; however, here it is sufficient to discuss the use of CFD in studies relevant to industrial suspension crystallization processes.

Several studies have used CFD modeling for continuous suspension crystallizers, including Sha et al. (2001) and Rielly and Marquis (2001). The study of Sha et al.

concluded that the suspension density in the crystallizer affects the classification process; in an imperfect suspension, the properties of the suspension depend on both the mixing intensity and product removal location. It was also noted that tanks of different geometries had different efficiencies of classification. These results are in good agreement with the experiments of Sha and Palosaari (2000a). The study of Rielly and Marquis examined a nonideal MSMPR or imperfectly mixed suspension crystallizer and gave results in good agreement with the experiments of Sha and Palosaari (2000b). A suspension crystallizer with a draft tube was studied by Synowiec et al. (2002) using a CFD package for a homogeneous liquid in conditions of turbulent flow. They found that systems without a draft tube and having a flat bottom used a power input higher than those with a draft tube and an elliptic bottom, so that the draft tube helped to reduce the cost. In addition, increased stirrer diameter was shown to decrease the required power input.

CFD modeling of evaporative crystallizations has been performed for many types of crystallizers, such as vacuum pan crystallizers and forced-circulation (FC) crystallizers. Rein et al. (2004) used CFD to model the two-phase (massecuite-vapor) flow inside a vacuum pan where the temperature field was assumed isothermal. The results showed that circulation in a vacuum pan is one of the most important parameters affecting performance. A system similar to this work was studied by Pennisi et al. (2003); this study focused on a sugar mill evaporator and modeled the areas above and below the calandria in the evaporator. The free surface in the region above the calandria was modeled with a rigid boundary with free slip. The results showed reasonable agreement when compared with measurements taken from the actual vessel that was modeled. The predictions showed that the design of the juice distribution system at the inlet to the vessel had a major influence on the flow field in the remainder of the vessel. A large amount of mixing was found to occur at the evaporator inlet which meant that juice with properties similar to that of the outlet stream was forced to the region of the calandria, and this reduced the efficiency of the equipment. Kramer et al. (2000) and Essemiani et al. (2004) performed CFD studies on FC crystallizers. Their work assumed the crystallizers were isothermal systems and hence considered only the hydrodynamic effects. The group of Kramer modeled only the part below the free surface by a single-phase (liquid) model. Their results showed that the flow in an FC crystallizer was not uniform. This indicates that the MSMPR assumption cannot be used to analyze the parameters in this crystallizer. The authors suggested that crystallization parameters need to be estimated at all locations in the crystallizer in order to correctly model the system. The group of Essemiani modeled an entire tank with two-phase (liquid-vapor) flow. Their results showed that the system was not perfectly mixed, and the feed rate and crystallizer geometry affected the flow characteristics.

None of the reviewed literature models two-phase (liquid-vapor) flow in a DTB crystallizer. Therefore, the present study proposes to numerically simulate the two-phase (liquid-vapor) flow in that type of crystallizer. In particular, this work aims to numerically study the general characteristics of the flow fields and classification of crystals and effects of the momentum source strength (this is the representation of the power transmitted by the impeller) and the fines removal flow rate on the flow patterns and classification of crystals by using the CFD commercial software ANSYS CFX-10.0.

Mathematical Models

Numerical simulations of two-phase flow inside a DTB crystallizer were carried out using the Eulerian-Eulerian multiphase models in the program CFX-10.0. In this model both the continuous and dispersed phases are considered as continuous media: the different phases are treated mathematically as interpenetrating continua. The concept of the phase volume fraction is introduced because the volume occupied by a particular phase cannot be occupied by any other phase. The phase volume fraction is defined as the proportion of the spatial volume taken up by the phase identified by the volume fraction. The volume fractions of the phases are predicted based on the condition that the sum of the volume fractions for all phases is equal to 1 at all times in all control volumes. Conservation equations for each phase are derived to obtain a set of equations that have a similar structure for all phases. Within the Eulerian-Eulerian model, the interphase transfer terms can be modeled using the particle model (inhomogeneous model), the mixture model, or the homogeneous model.

Because the liquid and vapor in this system are separated by a distinct interface, the particle model (for the vapor bubbles in the liquid flow) and the free surface flow model (for the liquid free surface) should be used together to model the vapor-liquid two-phase flow (which consists of gas bubbles produced in an external heat exchanger contained within the bulk liquid). This research deals with an essentially isothermal system, so that we model the system with respect only to momentum transfer. Based on these methods the software solves the continuity and momentum equations for a generic multiphase system and therefore allows the determination of separate solution flow fields for each phase simultaneously.

In the numerical model the vapor phase is modeled as a dispersed phase and the liquid phase is modeled as a continuous phase. The set of equations for the general case of Newtonian two-phase systems is given below (ANSYS Canada, 2005).

Continuity:

$$\frac{\partial(r_d\rho_d)}{\partial t} + \nabla \bullet (r_d\rho_d\mathbf{U}_d) = 0 \tag{1}$$

$$\frac{\partial(r_c\rho_c)}{\partial t} + \nabla \bullet (r_c\rho_c\mathbf{U}_c) = 0 \tag{2}$$

Volume balance:

$$r_d + r_c = 1 \tag{3}$$

Momentum:

$$\frac{\partial}{\partial t}(r_d\rho_d\mathbf{U}_d) + \nabla \bullet (r_d\rho_d\mathbf{U}_d\mathbf{U}_d) = -r_d\nabla p'_d + r_d\rho_d\mathbf{g} + \nabla \bullet \left(r_d\mu_{eff,d}(\nabla\mathbf{U}_d + (\nabla\mathbf{U}_d)^T)\right) + \mathbf{S}_{M,d} + \mathbf{M}_{dc} \tag{4}$$

$$\frac{\partial}{\partial t}(r_c\rho_c\mathbf{U}_c) + \nabla \bullet (r_c\rho_c\mathbf{U}_c\mathbf{U}_c) = -r_c\nabla p'_c + r_c\rho_c\mathbf{g} + \nabla \bullet \left(r_c\mu_{eff,c}(\nabla\mathbf{U}_c + (\nabla\mathbf{U}_c)^T)\right) + \mathbf{S}_{M,c} + \mathbf{M}_{cd} \tag{5}$$

where r is the volume fraction of the relevant phase, the subscripts d and c refer to the dispersed and continuous phases respectively, μ_{eff} is the effective viscosity, and

$S_{M,d}$ and $S_{M,c}$ are user-defined momentum sources for the vapor and liquid phases, respectively (in this work a momentum source is used to represent the power transmitted by the impeller, $S = P/UV$). For the liquid phase, the effective viscosity is composed of three contributions, the molecular viscosity, the turbulent viscosity, and the particle-induced viscosity:

$$\mu_{eff,c} = \mu_c + \mu_t = \mu_c + \mu_{t,c} + \mu_{t,b} \tag{6}$$

The turbulent viscosity of the liquid phase is based on the $k - \varepsilon$ model and formulated as follows:

$$\mu_{t,c} = C_\mu \rho_c \frac{k^2}{\varepsilon} \tag{7}$$

where C_μ is a dimensionless variable with a value of 0.09. The constants k and ε are determined from the equations for the turbulent kinetic energy and turbulence dissipation rate. The term $\mu_{t,b}$ is the particle-induced eddy viscosity. There are several models available to take account of this viscosity. In this work the model proposed by Sato and Sekoguchi (1975) was used:

$$\mu_{t,b} = C_{\mu,b} \rho_c r_d d |\mathbf{U}_d - \mathbf{U}_c| \tag{8}$$

where $C_{\mu,b}$ is a model constant that equals 0.6 (Deen et al., 2002) and d is the bubble diameter. The effective vapor viscosity is calculated from the effective liquid viscosity as follows:

$$\mu_{eff,d} = \frac{\rho_d}{\rho_c} \mu_{eff,c} \tag{9}$$

as was proposed by Jakobsen et al. (1997). The term p' is the modified pressure given by:

$$p'_d = p_d + \frac{2}{3} \rho_d k \tag{10}$$

$$p'_c = p_c + \frac{2}{3} \rho_c k \tag{11}$$

In this work, the turbulence was treated using the $k - \varepsilon$ model where both phases share the same values for k and ε (Micale and Montante, 1999; Montante and Magelli, 2003). The values of k and ε come directly from the differential transport equation for the turbulence kinetic energy and turbulent dissipation rate, as shown below:

$$\frac{\partial(\rho k)}{\partial t} + \nabla \bullet (\rho \mathbf{U} k) = \nabla \bullet \left[\left(\mu + \frac{\mu_t}{\sigma_k} \right) \nabla k \right] + P_k - \rho \varepsilon \tag{12}$$

$$\frac{\partial(\rho \varepsilon)}{\partial t} + \nabla \bullet (\rho \mathbf{U} \varepsilon) = \nabla \bullet \left[\left(\mu + \frac{\mu_t}{\sigma_\varepsilon} \right) \nabla \varepsilon \right] + \frac{\varepsilon}{k} (C_{\varepsilon 1} P_k - C_{\varepsilon 2} \rho \varepsilon) \tag{13}$$

where $\sigma_k = 1.0$, $\sigma_\varepsilon = 1.3$, $C_{\varepsilon 1} = 1.44$, $C_{\varepsilon 2} = 1.92$, $\rho = r_d \rho_d + r_c \rho_c$, $\mu = r_d \mu_d + r_c \mu_c$, $\mathbf{U} = (r_d \rho_d \mathbf{U}_d + r_c \rho_c \mathbf{U}_c)/\rho$, and $\mu_t = C_\mu \rho k^2/\varepsilon$. The term P_k is the production of

turbulent kinetic energy, determined via the equation:

$$P_k = \mu_t \nabla \mathbf{U} \bullet \left(\nabla \mathbf{U} + (\nabla \mathbf{U})^T\right) - \frac{\mu_t}{\rho \mathrm{Pr}_t} \mathbf{g} \bullet \nabla \rho \tag{14}$$

where Pr_t is the turbulent Prandtl number, defined as $c_p \mu / \lambda_t$, and μ, c_p, and λ_t represent the viscosity, specific heat capacity at constant pressure, and thermal conductivity, respectively, for the liquid phase.

The interfacial momentum transport between both phases is expressed in the term **M**. This term can consist of several forces, for example, the interphase drag, lift, wall lubrication, virtual mass, turbulence dispersion, and solid pressure forces. The drag and turbulence dispersion forces are the most important forces and are described as follows:

$$\mathbf{M}_{cd}^{D} = -\mathbf{M}_{dc}^{D} = \frac{3}{4} \frac{C_D}{d} r_d \rho_c |\mathbf{U}_d - \mathbf{U}_c| (\mathbf{U}_d - \mathbf{U}_c) \tag{15}$$

$$\mathbf{M}_{cd}^{TD} = -\mathbf{M}_{dc}^{TD} = -C_{TD} \rho_c k_c \nabla r_c \tag{16}$$

In the spherical cap regime, the drag coefficient C_D (cap) is approximately equal to 8/3. In the distorted regime, Ishii and Zuber (1979) gave the following expression for the drag coefficient C_D(ellipse):

$$C_D(ellipse) = \frac{2}{3} E_0^{1/2} \tag{17}$$

where E_0 is the Eotvos number ($E_0 = g \Delta \rho d_d^2 / \sigma$). A typical bubble size of 2.0 mm gives $E_0 = 0.76$ and C_D(ellipse) = 0.58. A relation for the drag coefficient of spherical bubbles was given by Schiller and Naumann (1933), and ANSYS CFX-10.0 modifies this to ensure the correct limiting behavior in the inertial regime by taking:

$$C_D(sphere) = \max\left[\frac{24}{\mathrm{Re}_b}(1 + 0.15\mathrm{Re}_b^{0.687}), 0.44\right] \tag{18}$$

with $\mathrm{Re}_b = \rho_c |U_d - U_c| d_d / \mu_c$, the bubble Reynolds number. In this case, ANSYS CFX automatically takes into account the spherical particle and spherical cap limits by setting:

$$C_D(dist) = \min[C_D(ellipse), C_D(cap)] \tag{19}$$

$$C_D = \max[C_D(sphere), C_D(dist)] \tag{20}$$

For the turbulent dispersion force, $\mathbf{M}_{cd}^{TD}$ is given by Lopez de Bertodano (1991), and is shown as Equation (16), where C_{TD} values of 0.1–0.5 are used in this work, since the bubble diameter is in the order of a few millimeters.

Methods

Physical Description and Geometry

In this study, the internal two-phase (liquid-vapor) flow of a pilot scale 1.05 m^3 DTB crystallizer was simulated. The crystallizer geometry and dimensions are given in Figure 1.

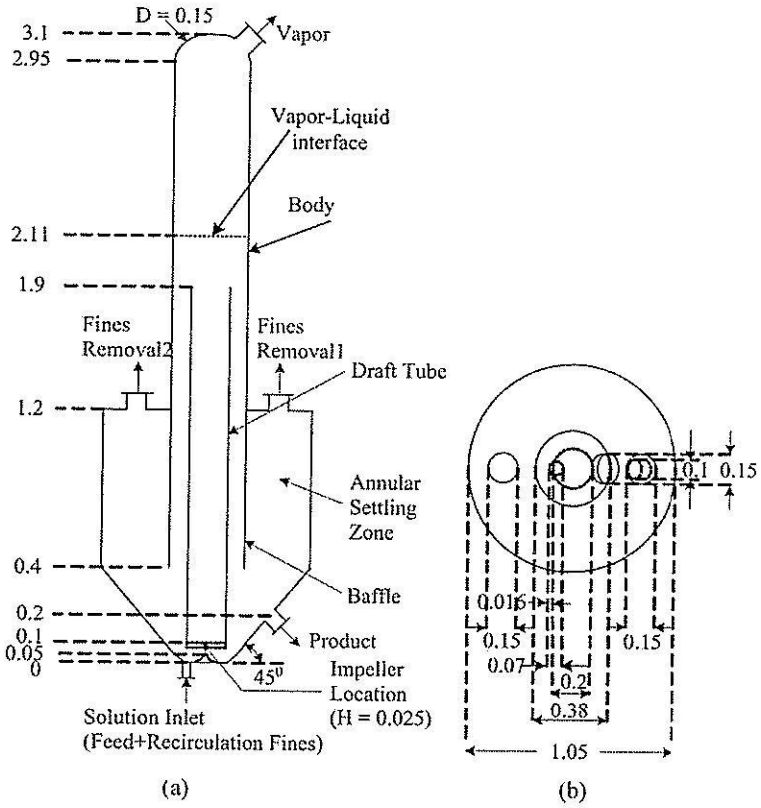

Figure 1. DTB crystallizer geometry and dimensions: (a) side view; (b) top view. Dimensions are given in meters.

The axial flow impeller revolves in such a way that the flow is directed upward from the bottom of the draft tube to the top section of the crystallizer. The vapor will be separated out from the liquid phase at the free surface at the top of the crystallizer body. The crystal suspension is circulated downwards along the outside of the draft tube. The outside shell of the crystallizer is a settling zone where an upward flow causes classification such that fine crystals are removed from the crystallizer through the fines removal flows, and large crystals settle and leave the crystallizer at the product outlet tube or are recirculated into the main crystallizer body. The flow of mother liquor containing fine crystals is mixed with fresh feed solution, passed through an external heat exchanger for heat input and dissolution of fine crystals, and then returned to the bottom section of the crystallizer.

Flow Simulation

The commercial software ANSYS CFX-10.0 was employed to simulate three-dimensional flow in the DTB crystallizer. The wall of the solution inlet tube, product outlet tube, fines removal tube, vapor outlet tube, draft tube, baffle, and tank are described using a thin surface material.

The impeller is represented as a momentum source term (Pericleous and Patel, 1987) in the vertical direction (upward flow) only. In the real impeller there are also

radial components of the momentum addition, however, they are effectively damped out by baffles placed in the normal direction to the tank walls. Since the radial components of the momentum addition are damped out in this design, we have not attempted to model them here to reduce the model complexity. A momentum source term has been added at the base of the draft tube, at the position and size ($0.000785\,m^3$) of the true impeller.

The material is assumed to occur as two phases (liquid and vapor), which is an acceptable approach considering that the particles are mostly sufficiently small to be considered to follow the liquid flow and that the particle suspension is reasonably dilute so that the impact of solids on the flow field is negligible. A water solution with 26.66% NaCl is the liquid phase in the crystallizer, and water vapor is the vapor phase. The physical properties of these materials at 106°C (the boiling point of the solution) are constant, as shown in Table I. All of the properties of water vapor are available in ANSYS CFX-10.0, and all properties of water solution with 26.66% NaCl at 106°C were taken from Mullin (2001), with the exception of the viscosity, which was taken from McCabe et al. (2001). Steady-state flow is assumed throughout because this type of industrial crystallizer is mostly operated as a steady-state continuous process. Turbulent flow is assumed throughout because the mixing process in the crystallizer normally produces turbulent flow, and this is modeled using the homogeneous model with the standard $k-\varepsilon$ model, which is described in the previous section.

Because the vapor is assumed to form in an external heat exchanger before being fed into the crystallizer the temperature rise in the circulated magma is caused only by the impeller and heat of crystallization, and it is a low value, in the order of 1°C (Myerson, 2002). Therefore, the flow can be assumed to be an isothermal process without significant error.

All the walls (the wall of the solution inlet tube, product outlet tube, fines removal tubes, vapor outlet tube, draft tube, baffle, and tank) had boundary conditions of smooth walls, and zero-slip conditions are used for both the liquid and vapor phases. At the solution inlet conditions the mass flow rates of each phase were specified directly, the volume fraction of vapor was set to 0.1, and the volume fraction of liquid was set to 0.9. At all the outlets (vapor out, product out, and fines removal) the mass flow rate of each phase was specified directly.

The free surface is treated as an inhomogeneous free surface flow model. This model is used to separate the vapor phase from the liquid phase. The surface-tension effect along the interface is included. In this work, the surface tension was specified directly, and the initial liquid level is located at the height of 2.11 m from the bottom

Table I. Physical properties of vapor and liquid at 106°C

	Phase	
Physical properties	Liquid	Vapor
Density (kg/m^3)	1164	0.59
Viscosity (kg/s/m)	0.00052	0.0000128
Thermal conductivity (W/m/K)	0.65	0.025
Surface tension (N/m)	0.06	—

of the tank. The initial volume fraction must be consistent (vapor is the only phase present in the area above the free surface and liquid is the only phase present in the area under the free surface). The initial pressure field is hydrostatic in the area under the free surface continuing to the bottom of the tank (the hydrostatic pressure is defined as a function of the height of the tank, gravitational acceleration, and density of the liquid phase) and uniform in the area above the free surface. These conditions are easily programmed using step functions and defined in the ANSYS CFX program.

The 3-D computation of an unstructured mesh adopted to run all simulations is depicted in Figure 2(a). It consisted of 16058 nodes and 77867 tetrahedral elements. Automatic mesh adaptation was applied to increase the mesh density in regions where a finer mesh is required for accurate solution. This means that as the solution is calculated, the mesh density can automatically be increased in regions where the solution is likely to require a finer mesh, in order to resolve the features of the flow in these regions, and decreased in regions where a less dense mesh will still result in an accurate simulation. In this work, the vapor volume fraction was selected as the adaptation variable, because it is an important variable that changes rapidly in the region of the liquid-vapor interface. An example of an unstructured mesh after mesh adaptation is depicted in Figure 2(b): this particular mesh consists of 79460 nodes and 389738 tetrahedral elements. Note that the number of nodes and elements after mesh adaptation is not necessary equal to Figure 2(b) because the adaptation depends on the flow conditions in the system. The number of nodes and elements

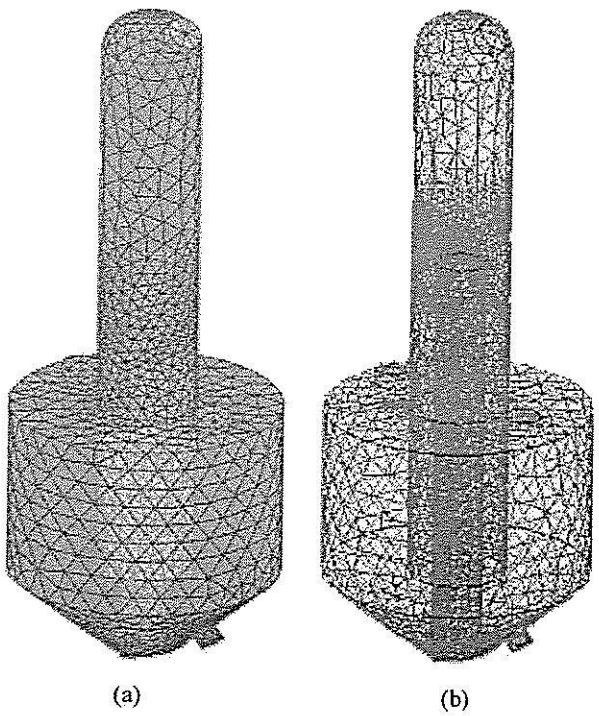

Figure 2. Examples of the computational mesh of the DTB crystallizer: (a) before mesh adaptation; (b) after mesh adaptation.

after mesh adaptation used in this work are in the range of 70000–82000 nodes and 381000–408000 tetrahedral elements.

The numerical model is based on solving Equations (1)–(5) and Equations (12) and (13) numerically using ANSYS CFX-10.0. This program uses a range of space and time discretization methods in order to enable a numerical solution to be calculated. The finite volume method is used to solve over the crystallizer volume. First, the volume being investigated is discretized into small tetrahedral elements with nodes at each corner of the element (this, as described above, is the mesh generation step). The partial differential equations (Equations (1)–(5) and Equations (12)–(13)) are integrated over all the control volumes in the region of interest. All the solution variables and fluid properties are stored in the nodes of the element. These integral equations are then converted to a system of algebraic equations by generating a set of approximations for the term in the integral equations. Finally, the algebraic equations are solved iteratively until the convergence criteria or maximum iteration is reached. Note that exact details of the calculation methods for the software are available in the detailed user notes accompanying the software (ANSYS Canada, 2005).

The solution was first obtained using a coarse grid, and the calculation was preformed iteratively until the residuals reduced to an acceptable level. To achieve grid independent results, the grids were refined step by step until changes in the numerical solution were unnoticeable.

Case Studies

Simulations were performed with eight different momentum source strengths and five different fines removal flow rate values, as indicated in case studies 1 to 13 in Table II. For all case studies the amount of the vapor in the feed solution is 10% of the volume of the total feed solution, the amount of vapor leaving the crystallizer is equal to the amount of vapor in the feed solution, and the product crystal suspension flow rate is maintained constant at 0.1797 kg/s. Note that the values of the parameters chosen were based on values used in an experimental and theoretical article on the same crystallizer at Delft University of Technology (Eek et al., 1995).

Results and Discussion

General Characteristics of Flow Fields in a DTB Crystallizer

The general flow patterns in the DTB crystallizer are shown in Figure 3, which represents the velocity vectors, contours in the vertical center plane, and 3-D streamlines for the liquid and vapor phases. It shows that the liquid phase has to flow through and over the draft tube, and therefore there is net circulation through the draft tube. It is necessary to have this flow characteristic because the function of the draft tube is to assist in suspension of the crystals, as described in Paul et al. (2004). The liquid velocity in the up-flow region (inside the draft tube) is higher than in the down-flow region (outside the draft tube). This is because the cross-sectional area of the up-flow region (approximately $0.0314\,m^2$) is smaller than that of the down-flow region (approximately $0.0820\,m^2$). The crystallizer is designed in this way to create a significantly higher velocity in the upward flow region to assist in suspension of particles, and this high upward velocity is produced from the momentum added with the impeller. At a greater distance upward from the impeller, the velocity profile

Table II. Case studies

Case study	Variable (units)		
	Solution inlet flow (kg/s)	Total fines flow (kg/s)	Momentum source ($kg \cdot m/s^2$)
1	1.186	1.006	0
2	1.186	1.006	0.785
3	1.186	1.006	3.142
4	1.186	1.006	5.498
5	1.186	1.006	7.850
6	1.186	1.006	11.78
7	1.186	1.006	19.63
8	1.186	1.006	23.56
9	0.647	0.427	7.850
10	1.186	1.006	7.850
11	1.725	1.545	7.850
12	2.480	2.300	7.850
13	3.776	3.594	7.850

becomes more uniform, although averaged velocities in the core remain low (this is far enough from the bottom tube end of the draft tube that the effect of the impeller is less significant), and the velocity is approximately half of the maximum (0.9843 m/s), which occurs at approximately 0.3 m (1.5 times the diameter of the draft tube) above the impeller. Moreover, there is a small recirculation loop occurring under the region where the flow comes over the top of the draft tube. This is more pronounced at the side of the draft tube above the feed and is undesirable because it will lead to a nonuniform flow. This recirculation does not contribute at all to the desired circulation and could lead to different crystallization rates for crystals that are trapped there.

The vapor phase is present in only small amounts in the system (Figures 3(b) and 4), and only in the draft tube, after which it is separated out at the vapor-liquid interface. This means that the vapor and liquid regions of the crystallizer are separated by a clearly defined interface (free surface), which occurs at a height of 2.11 m, the same as the initial height of the free surface in the simulation. A small amount of vapor (less than 10% by volume) is in the draft tube because the feed to the crystallizer is 10% volume fraction vapor. The vapor is mostly in the regions near the left side of the draft tube and mostly separates out from the liquid at the top of the draft tube near the left side of the tank rather than the center of the tank because the feed is located under a position between the left side of the draft tube and the tank wall, and the rate of the feed (and also, therefore, the rate of vapor feed) is quite high in this case.

One drawback of many crystallizers is the tendency of the particles to sediment to the bottom of the tank and remain there. The shape of the tank bottom can significantly improve the uniformity of the particle suspension. The rounded tank "corners" and a central peak under the agitator, which is the bottom shape of the DTB crystallizer used in this work, constitute one of the best configurations for the tank bottom. The rounding of the corners is used to combat settling of particles

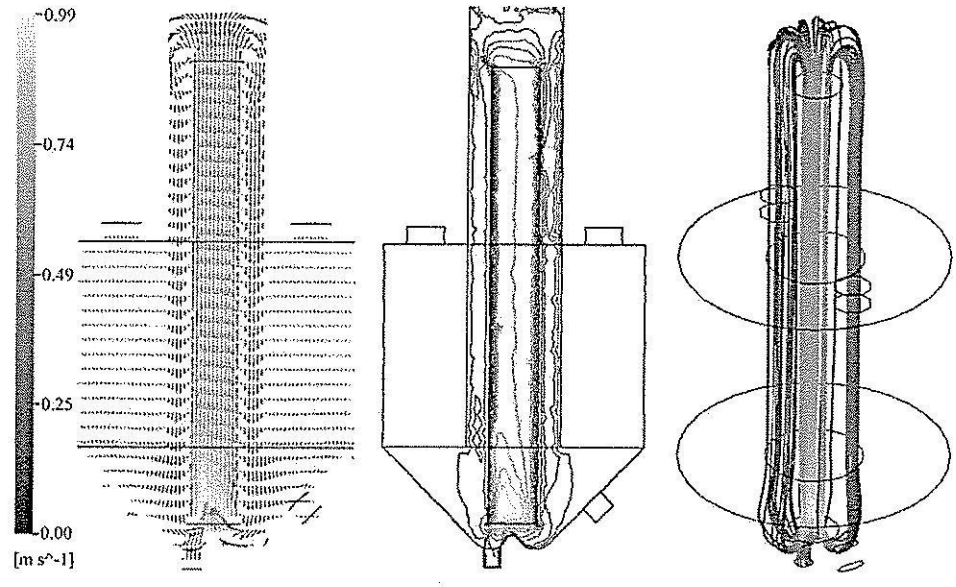

(a)

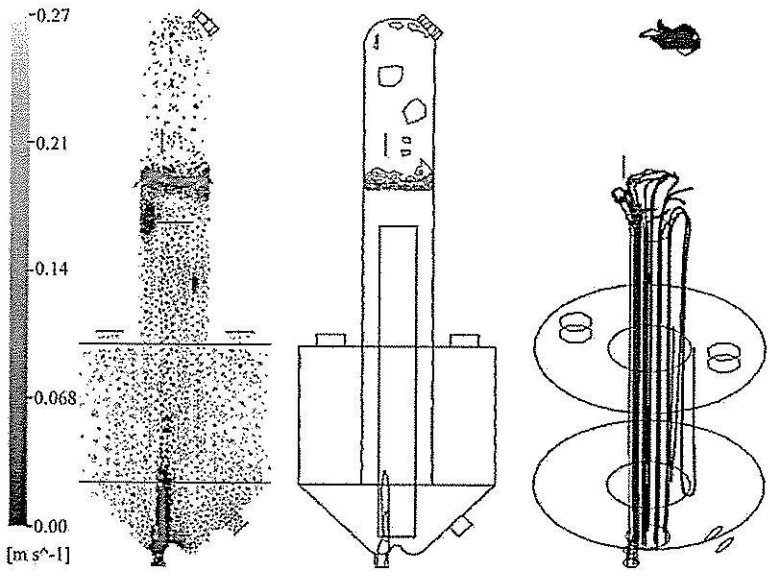

(b)

Figure 3. Velocity vectors, contours, and 3-D streamlines of liquid (a) and vapor (b) in the vertical center plane for case study 5.

and the center peak virtually eliminates the stagnation point (dead zone) that would be present at the bottom center of the tank under the agitator (Myerson, 2002). These effects can be confirmed by the velocity vectors shown in Figure 5, which demonstrates that the flow of all fluid packets tends to be into the draft tube.

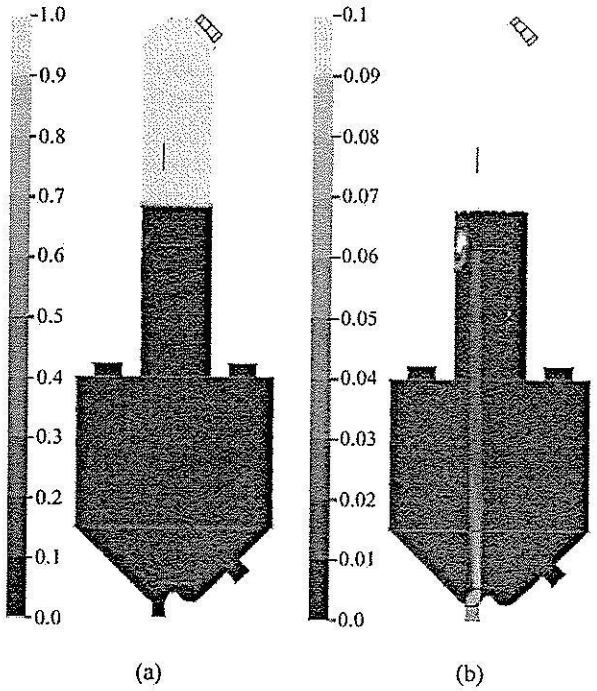

Figure 4. Contours of vapor volume fraction in the vertical center plane for case study 5: (a) overall fraction; (b) using a magnified scale to enable visualization in the draft tube.

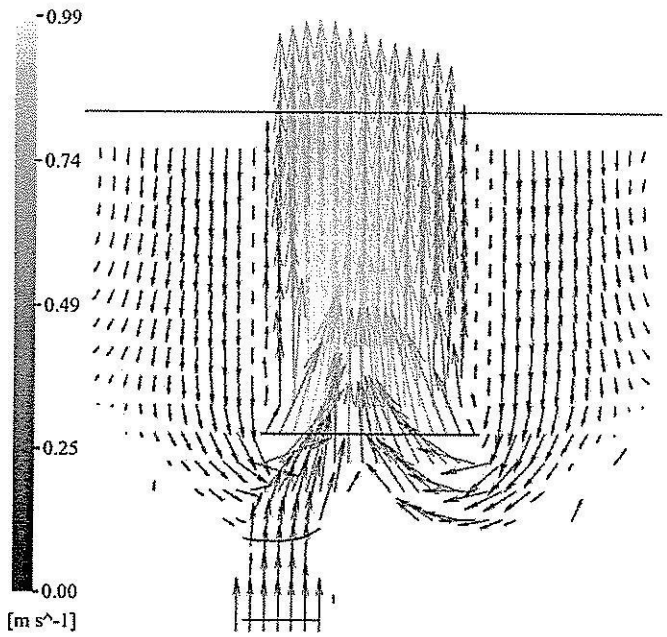

Figure 5. Liquid velocity vectors at the tank bottom for case study 5.

Effect of Momentum Source Strength on Flow Characteristics

The overall liquid velocity vectors and contours are shown in Figure 6, for momentum source values of 0, 0.785 and 3.142 $kg \cdot m/s^2$, and in Figure 7 for momentum source values of 5.498, 7.850, 11.78, 19.63, and 23.56 $kg \cdot m/s^2$. Flow contours for the same conditions as in Figure 7 are shown in Figure 8. Figure 6 indicates that for the cases of 0 (no momentum addition), 0.785, and 3.142 $kg \cdot m/s^2$, the flow of the liquid phase does not follow the general flow field in a DTB crystallizer at the impeller location; for these three cases there is upward flow in some areas immediately outside the draft tube because the momentum addition through the impeller is very low and is unable to force all the feed solution to flow into the draft tube. For the cases of 5.498, 7.850, 11.78, 19.63, and 23.56 $kg \cdot m/s^2$ (Figure 7), the flow of liquid follows the general flow field in a DTB crystallizer because the momentum addition through the impeller is high enough to assist the feed solution to flow into the draft tube.

As the momentum added through the impeller increases, the liquid velocity becomes larger both in the up-flow section inside the draft tube and in the down-flow area outside the draft tube. This results in a stronger flow at the bottom part of the draft tube (near the impeller location) and also a higher velocity inside the draft tube and a lower velocity in the annular space that assists in suspension of particles. The vapor velocity also increases with increasing momentum source addition, however, it increases by a much smaller degree than the liquid velocity (Figure 9).

The uniformity of the liquid flow can be clearly depicted by the overall velocity contours in Figure 8. The results show that full uniformity for the low liquid velocity in the particle settling zone was found for all the case studies; it is necessary to have uniform flow in this zone to aid in the classification of the crystals. The uniform flow and very low velocity of this zone indicate that there will be very slow crystallization

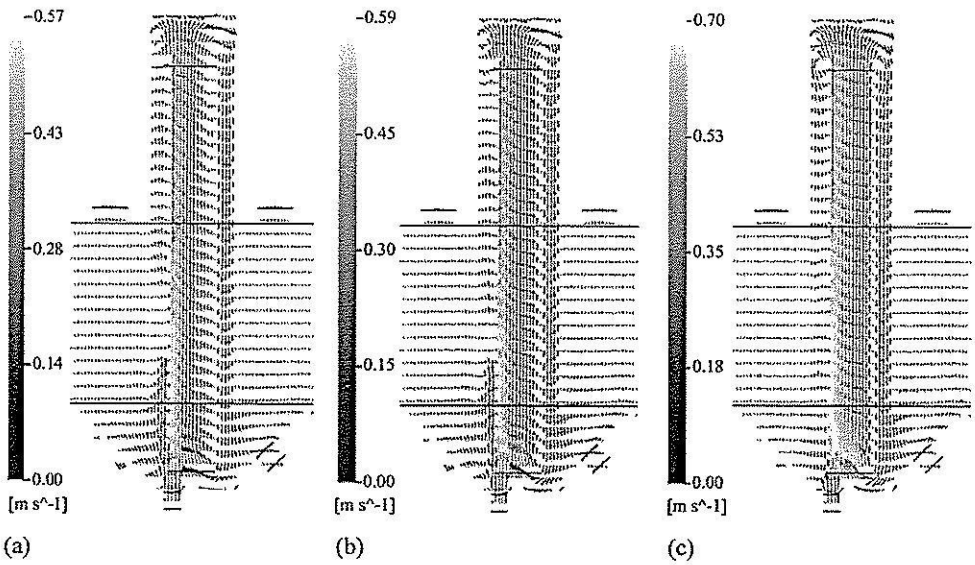

Figure 6. Liquid velocity vectors in the vertical center plane for momentum source additions of (a) 0 $kg \cdot m/s^2$, (b) 0.785 $kg \cdot m/s^2$, and (c) 3.142 $kg \cdot m/s^2$.

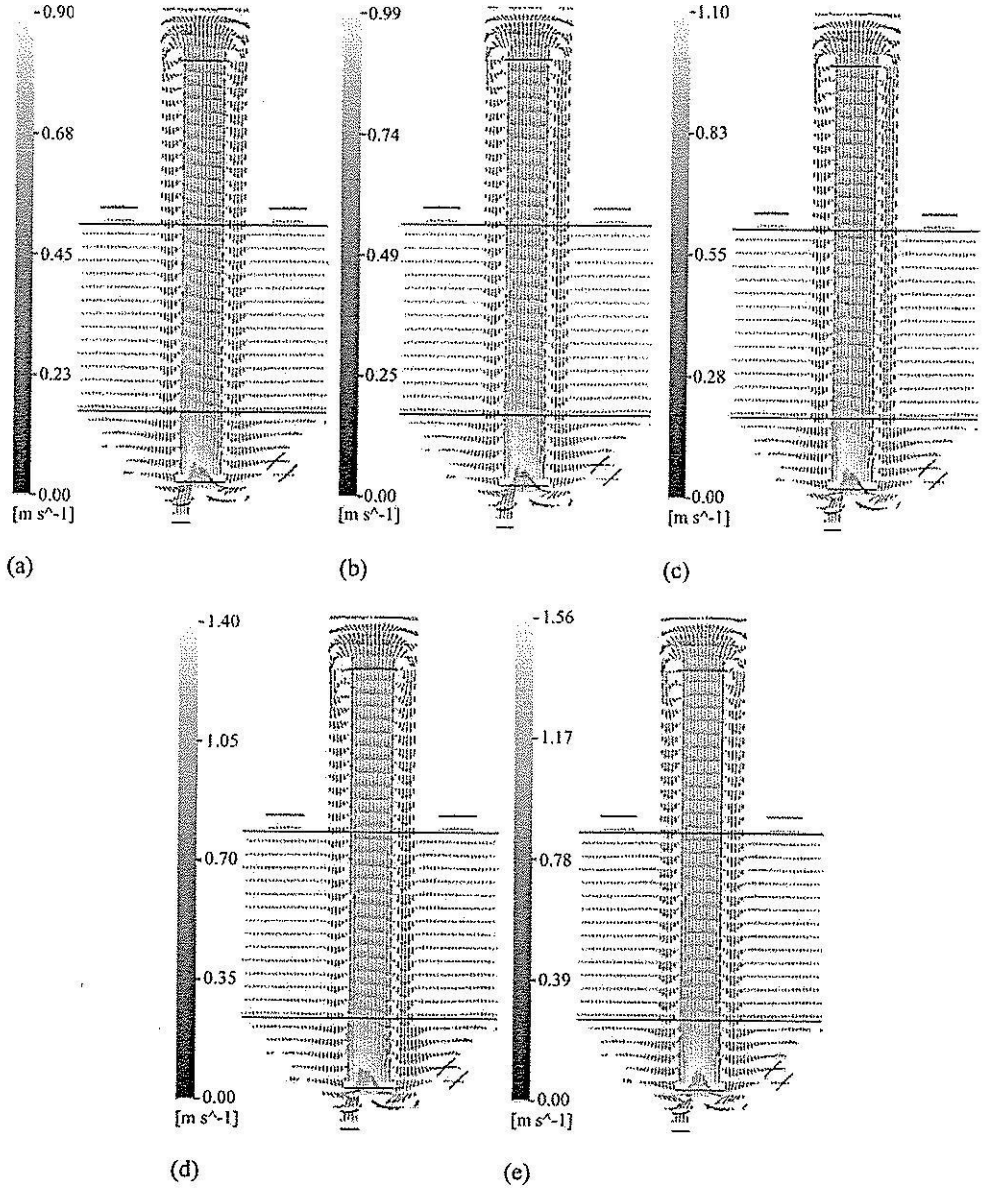

Figure 7. Liquid velocity vectors in the vertical center plane for momentum source additions of (a) 5.498 $kg \cdot m/s^2$, (b) 7.850 $kg \cdot m/s^2$, (c) 11.78 $kg \cdot m/s^2$, (d) 19.63 $kg \cdot m/s^2$, and (e) 23.56 $kg \cdot m/s^2$.

kinetics, probably entirely mass transfer controlled, in this zone. This is suitable because this zone is designed for the purpose of the particle settling process only. At the point that the liquid flows over the top of the draft tube and at the vapor-liquid interface, the overall flow feature is nonuniform for all case studies. This will lead to spatial variation in the kinetics of the processes occurring in crystallization, in particular the nucleation rate because of variations in the shear stress.

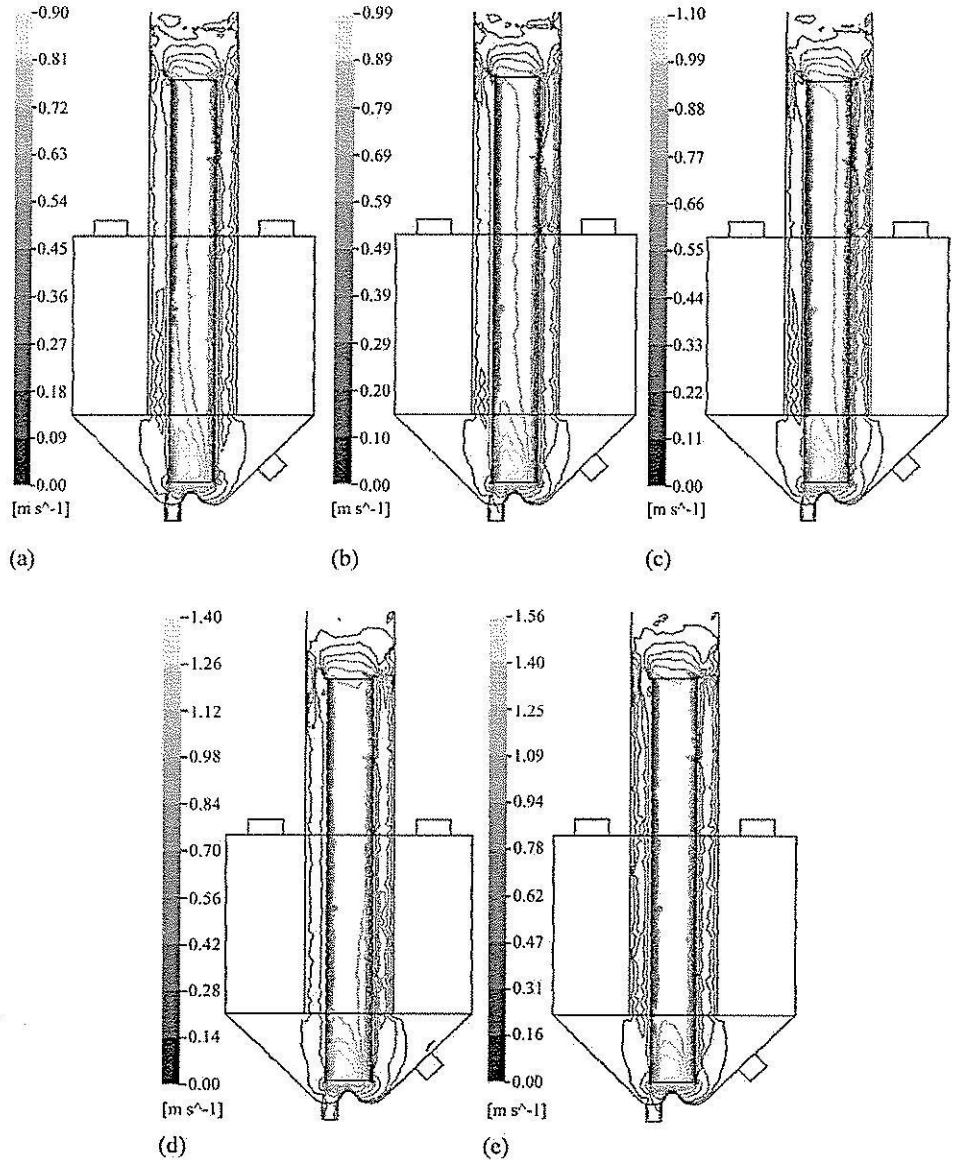

Figure 8. Liquid velocity contours in the vertical center plane for momentum source additions of (a) 5.498 kg · m/s^2, (b) 7.850 kg · m/s^2, (c) 11.78 kg · m/s^2, (d) 19.63 kg · m/s^2, and (e) 23.56 kg · m/s^2.

Considering the liquid velocity contours inside and outside the draft tube, it can be seen that the overall flow features are close to uniform at high values of the momentum source addition. Thus it is evident in Figure 8 (for the momentum source values of 7.850, 11.78, 19.63, and 23.56 kg · m/s^2 respectively) that full uniformity is found at the momentum source values of 19.63 and 23.56 kg · m/s^2. This uniform flow occurs from a height of 0.4 to 1.9 m (at the top of the draft tube) and would assist in producing a narrower crystal size distribution. Uniform flow can lead to

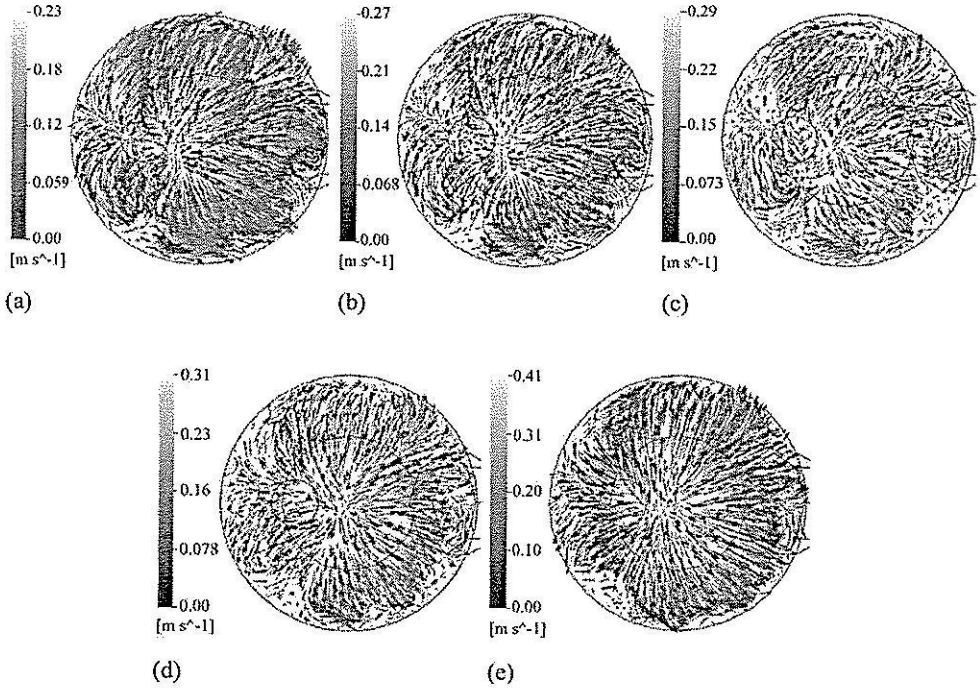

Figure 9. Vapor velocity vectors in the horizontal plane at the vapor-liquid interface for momentum source additions of (a) 5.498 kg·m/s^2, (b) 7.850 kg·m/s^2, (c) 11.78 kg·m/s^2, (d) 19.63 kg·m/s^2, and (e) 23.56 kg·m/s^2.

the smaller spatial variations in the crystallization rate, in particular a more uniform crystal growth rate, because the level of supersaturation in these areas will be constant. Note that this does not ensure a completely uniform particle size, because there is still a wide distribution of residence times for both the liquid and the crystals in the crystallizer. In addition, the residence time distributions of the liquid and the crystals are different because nucleation does not necessarily occur immediately upon the feed entering the crystallizer.

At the vapor-liquid interface, it is seen that at low momentum source additions (momentum source additions of 5.498, 7.850, and 11.78 kg · m/s^2), the vapor will be separated out from the liquid phase in the region from the center of the draft tube to the left wall of the tank (in the direction of the feed location), as shown in Figures 9(a)–(c). This means that momentum source values less than 11.78 kg · m/s^2 are insufficient to cancel the effect of the feed momentum on the flow field in the DTB crystallizer. When the momentum source addition are in the range of 19.63 to 23.56 kg · m/s^2 (Figures 9(d) and (e)) all vapor will be separated out only at the center of the tank. This indicates that momentum source values greater than 19.63 kg · m/s^2 are able to completely cancel the effect of the feed solution momentum on the flow field in the DTB crystallizer. There is a transition region between 11.78 and 19.63 kg · m/s^2 where the gas phase is partially separated and flows into both sections of the crystallizer. These values are correct for feed solution flows less

than or equal to 1.18 kg/s, which were used in these case studies, in a 1 m^3 crystallizer.

Effect of Fines Removal Flow Rate on Flow Characteristics

The overall liquid velocity vectors for the liquid phase for fines removal flows of 0.467, 1.006, 1.545, 2.300, and 3.594 kg/s are shown in Figure 10, and velocity contours for the same conditions are shown in Figure 11. These figures indicate that for fines removal flows of 0.467, 1.003, 1.545, and 2.300 kg/s the flows of the liquid

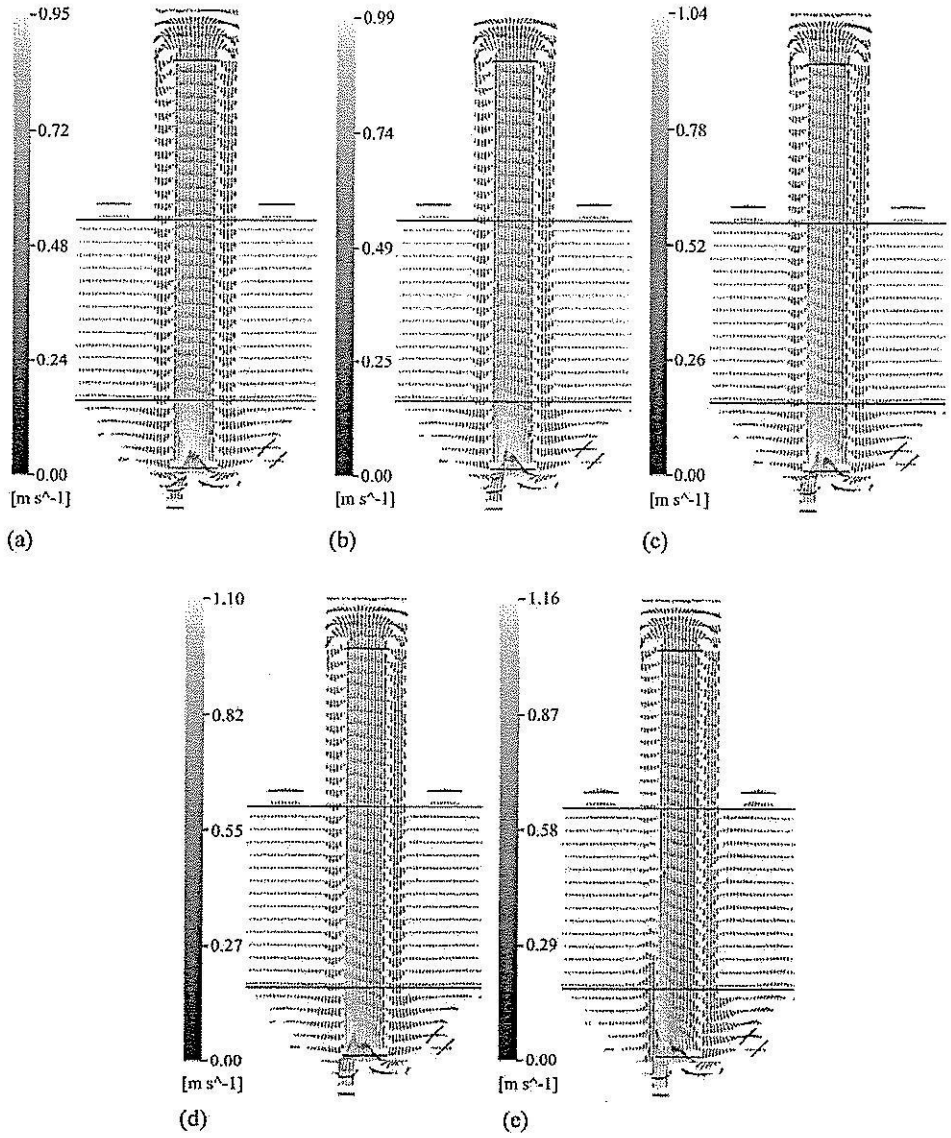

Figure 10. Liquid velocity vectors in the vertical center plane for fines removal flows of (a) 0.4672 kg/s, (b) 1.0063 kg/s, (c) 1.5454 kg/s, (d) 2.3002 kg/s, and (e) 3.594 kg/s.

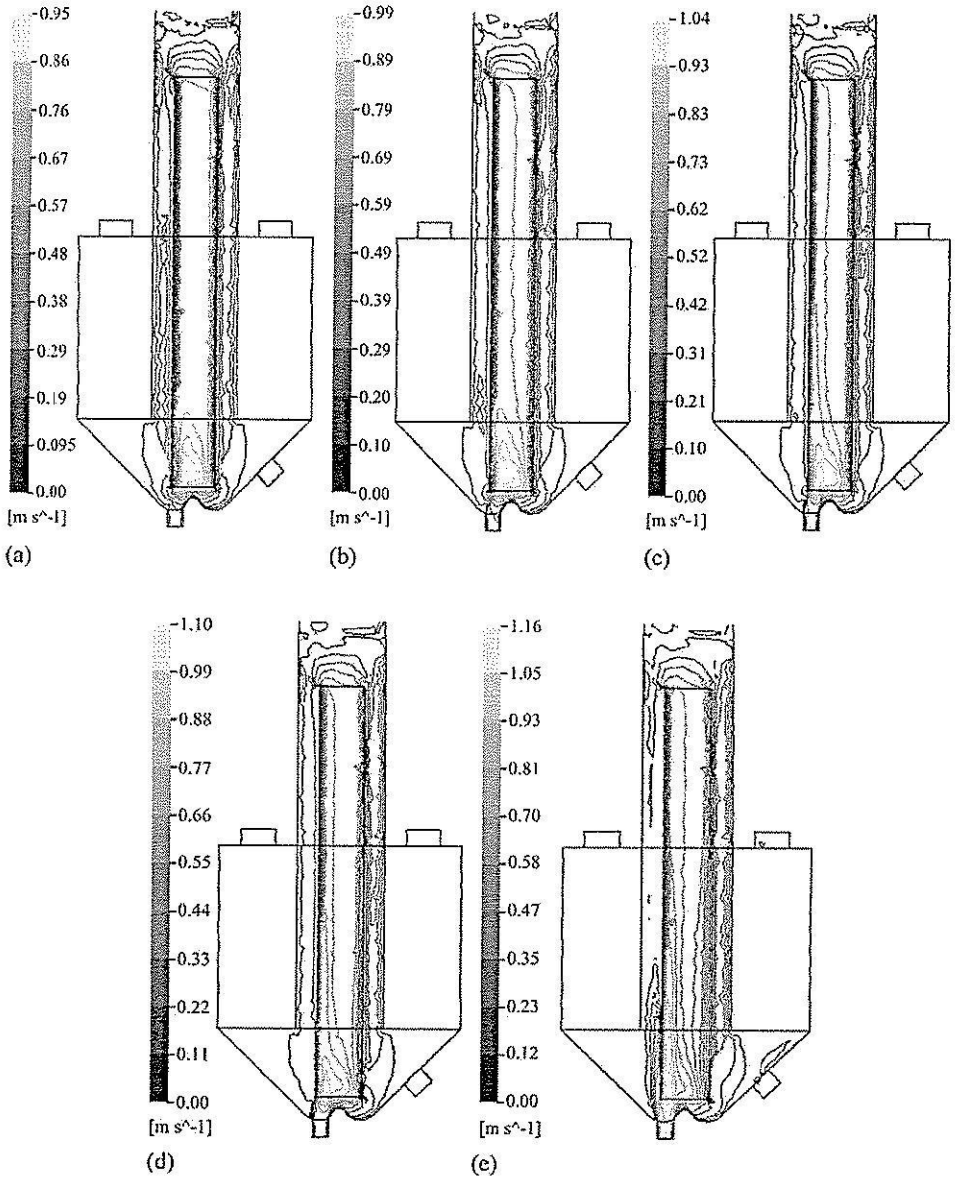

Figure 11. Liquid velocity contours in the vertical center plane for fines removal flows of (a) 0.4672 kg/s, (b) 1.0063 kg/s, (c) 1.5454 kg/s, (d) 2.3002 kg/s, and (e) 3.594 kg/s.

phase follow the typical flow field in a DTB crystallizer, which are described in a previous section. For a fines removal flow of 3.594 kg/s the flow fields are not typical flow fields in a DTB crystallizer because the momentum source addition of $7.85\,\mathrm{kg \cdot m/s^2}$ is not enough to assist the feed solution to flow into the draft tube (or is not enough to cancel the effect of the fines removal flow pulling the feed in the direction of the settling zone and the extra momentum in the feed inflow).

As the fines removal flow increases the liquid velocity slightly increases, both in the up-flow section inside the draft tube and in the down-flow area in the annular

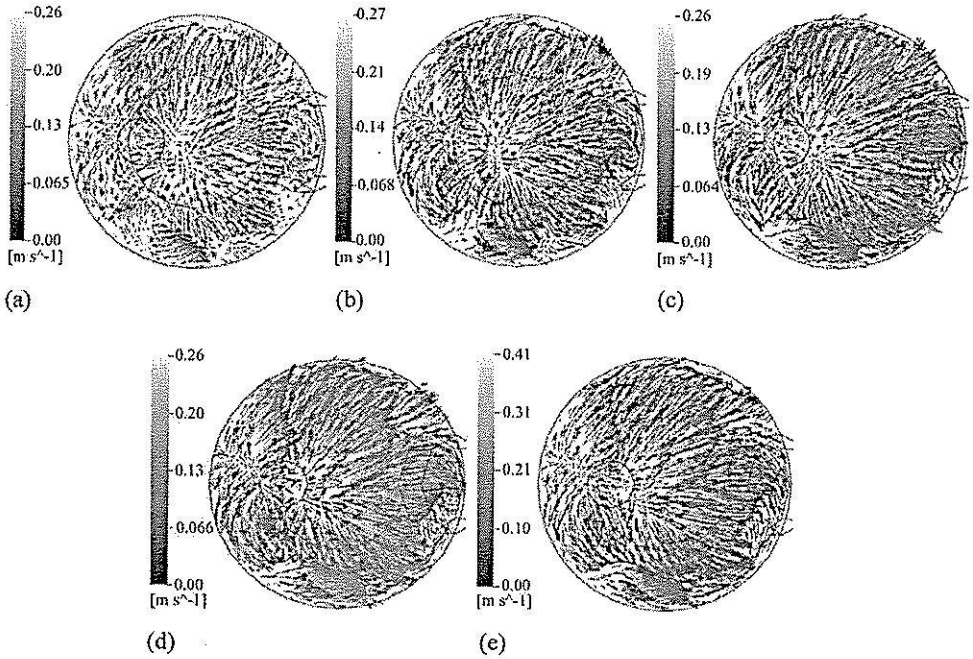

Figure 12. Vapor velocity vectors in the horizontal plane at the vapor-liquid interface for fines removal flows of (a) 0.4672 kg/s, (b) 1.0063 kg/s, (c) 1.5454 kg/s, (d) 2.3002 kg/s, and (e) 3.594 kg/s.

space outside the draft tube. The fines removal flow only slightly influences the overall vapor velocity (Figure 12). The flow patterns of the vapor phase have basically the same features without any drastic change in structure, and the other effects of the fines removal flow are the same as described previously (Figure 3(b)).

In most fines removal case studies the liquid flow is not uniform (Figure 11), except for the fines removal flow of 0.467 kg/s. This is because this low value of the fines removal flow forces the feed solution flow to be very low (the fines removal stream is added to the "raw" feed to the crystallizer so that small fines removals will also result in low net feed rates), so the rate of momentum source addition used in the case study ($7.85\,\mathrm{kg \cdot m/s^2}$) completely cancels the effect of the feed flow. At higher fines removal flows the momentum source addition is not high enough to cancel the effect of the feed flow momentum.

Considering the flow features at the vapor-liquid interface, it is seen that at fines removal flows of 1.006, 1.545, 2.300, and 3.594 kg/s, the vapor will be separated out from the liquid phase from the center of the tank to the left wall of the tank (in the direction of the feed location); this is shown in Figures 12(b)–(e). This indicates that a momentum source value of $7.85\,\mathrm{kg \cdot m/s^2}$ is not enough to cancel the effect of the feed on the flow field in the DTB crystallizer. At the fines removal flow of 0.467 kg/s (for which the feed is equal to 0.6470 kg/s), the majority of the vapor will be separated out from the liquid phase at the center of the tank (Figure 12(a)). This indicates that a momentum source value of $7.85\,\mathrm{kg \cdot m/s^2}$ completely cancels the effect of the feed solution flow of 0.467 kg/s or lower.

Table III. Hydrodynamic regimes for settling particles

Regime	Reynolds number	C_D expression
Stokes' law (laminar)	$Re_p < 0.3$	$C_D = 24/Re_p$
Intermediate law	$0.3 < Re_p < 1000$	$C_D = 18.5/Re_p^{3/5}$
Newton's law (turbulent)	$1000 < Re_p < 3.5 \times 10^5$	$C_D = 0.44$

Source: Paul et al. (2004).

Classification of Crystals

As described previously, the flow outside the draft tube is downward and the up flow outside the baffle (the annular settling zone) is low enough, and sufficiently uniform, to confirm the gravitational settling process of the crystals. The classification of crystals in this work was studied by analyzing the fines removal cut-size, which was calculated from the free settling velocity, U_t:

$$U_t = \sqrt{\frac{4g(\rho_p - \rho)d_p}{3C_D\rho}} \tag{21}$$

where the density of NaCl crystal is 2,155 kg/m^3 (Cheremisinoff, 1986), the C_D of each flow regime is shown Table III (calculated via the particle Reynolds number, $Re_p = \rho_c d_p U_t/\mu_c$), and the settling velocity is the predicted value from the simulation, which is the average value of the velocity over the volume in the annular settling zone. Calculation of the fines removal cut-size (d_p) was performed with an iterative calculation since the value of the Reynolds number determines the flow regime. Crystals smaller than the fines removal cut-size will be removed from the crystallizer in the fines removal flows, and crystals larger than this size will settle and leave the crystallizer as product or be recirculated back into the crystallization zone. Thus,

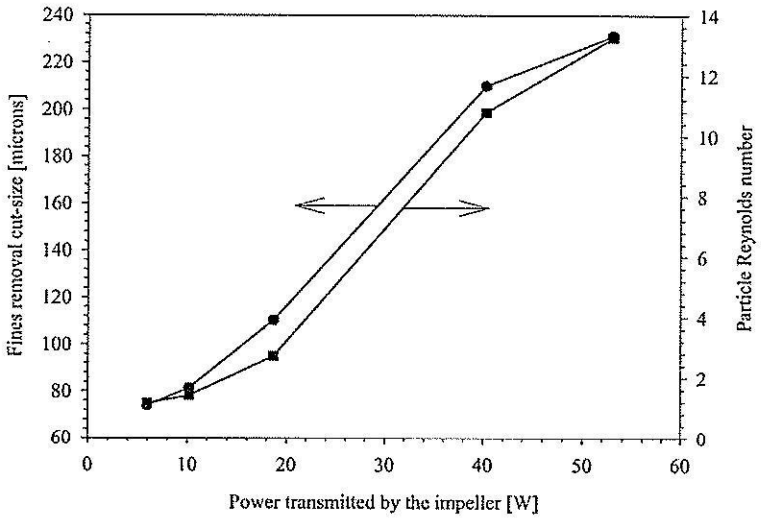

Figure 13. Fines removal cut-size and particle Reynolds number for case studies 1 to 8 as a function of power transmitted by the impeller.

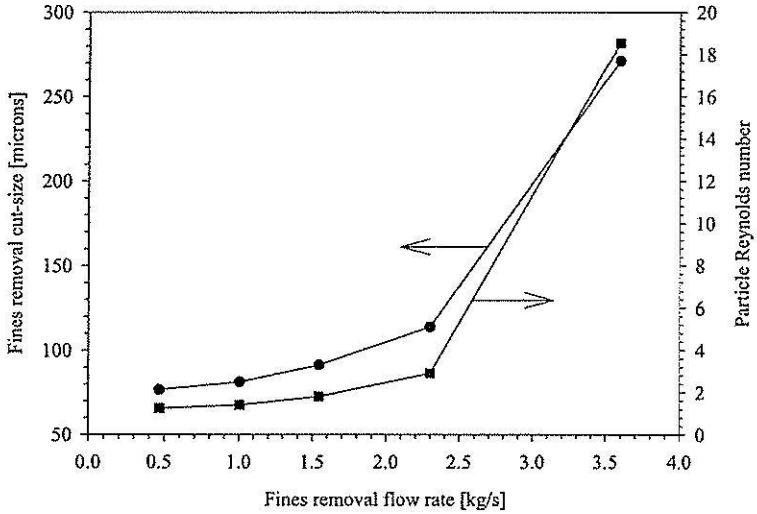

Figure 14. Fines removal cut-size and particle Reynolds number for case studies 9 to 13 as a function of fines removal flow.

the fines removal cut-size is the minimum size of crystal that would be fully settled in the annular settling zone.

The effects of the power transmitted by the impeller (the effect of the momentum source strength) and the fines removal flow rate on the classification of crystals are shown in Figures 13–15. Figure 13 shows that the fines removal cut-size increases with increasing power transmitted by the impeller. This suggests that the mean product crystal size increases with increasing momentum source (although this is not definite since increasing the momentum source may also lead to higher nucleation

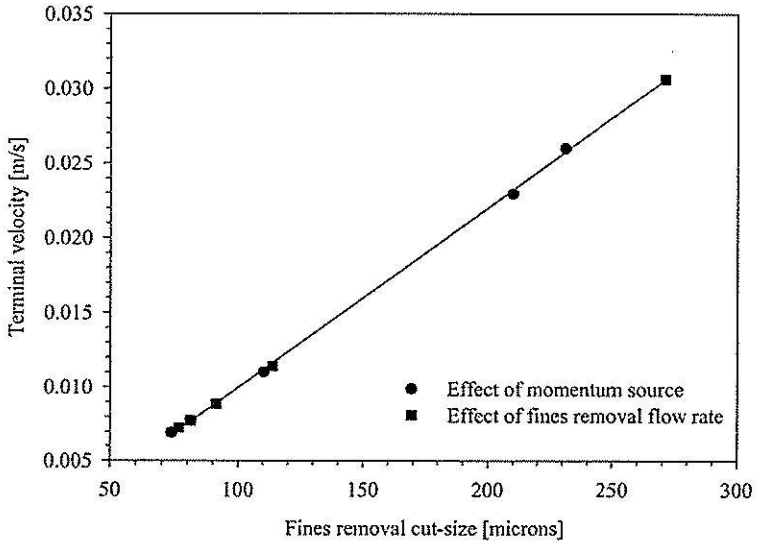

Figure 15. Terminal velocity for case studies 1 to 13 as a function of fines removal cut-size.

or attrition rates). This result is due to the varying up-flow velocities in the fines removal section since the momentum source affects the flow velocities in the annular space. This will strongly affect the product crystal size distribution. The particle Reynolds numbers increase with increasing power transmitted by the impeller, and all the values of the Reynolds number are in the lower end of the range of the transition regime for particle flow ($0.3 < \mathrm{Re}_p < 3000$).

Figure 14 shows that as the fines removal flow increases (equivalent to increasing the feed solution flow because the product flow is held constant) the fines removal cut-size increases; this agrees well with the experimental results of Eek et al. (1995). This indicates that the mean product crystal size increases with increasing fines removal flow. Increasing the fines removal flow also increases the number of fine crystals destroyed in the heat exchanger, thus reducing the total number of crystals in the vessel; from the mass balance for the system it can be seen that this also increases the mean particle size in the system. The particle Reynolds number increases with increasing fines removal flow, and all values of the Reynolds number in the transition regime for particle flow, similar to the experiments that varied the momentum source strength. Figure 15 shows that the terminal velocity increases approximately linearly with increasing particle size; this agrees with the results of Lapple (1951).

Conclusions

The proposed computational study to obtain flow fields and to study the classification of crystals within the model DTB crystallizer with fines removal appears to successfully model a DTB crystallizer, and the results obtained are a reasonable representation of what would occur in a real crystallizer. The following conclusions can be made.

1. The overall magnitude of liquid velocity within the crystallizer can be strongly increased by increasing the axial momentum source but only slightly increased by the fines removal flow rate. For the vapor phase, the overall magnitude of the velocity can be slightly increased by the axial momentum source and only slightly influenced by the fines removal flow rates.
2. The effect of feed solution flow on flow characteristics in the DTB crystallizer can be cancelled by momentum source values equal to or higher than $19.63\,\mathrm{kg \cdot m/s^2}$ for a feed solution lower than 1.2 kg/s. The liquid flow is found to be uniform in the main body of the crystallizer with this condition also.
3. Momentum source strengths and fines removal flow rates also have a significant effect on the fines removal cut-size due to varying up-flow velocities in the fines removal section altering the size at which particles are carried out in the fines removal stream. This will strongly affect the product crystal size distribution. The fines removal cut-size increases with increasing momentum source (or power transmitted by the impeller) and fines removal flow rate.

The results from the current study show how CFD can be used to analyze the performance of a DTB crystallizer to produce a suitable product particle size distribution. In particular, the fines removal cut-size can be changed by alteration of the fines removal flow rate, the agitator speed, and the area used for the settling space in ways that are predictable using a CFD model. If experimental values of the nucleation and crystal growth kinetics are available for a system, it is possible to

determine a suitable fines removal flow rate and fines removal cut-size that will result in a narrow particle size distribution with a suitable mean particle size.

CFD tools can be used for new efforts to improve the design, operation, and upgrade of industrial crystallizers and give results that should predict well the true situation in the crystallizer. This tool provides a cost-effective approach to process optimization, thus enabling analysis of the equipment design before committing to a final configuration.

Acknowledgment

This research was supported by the Suranaree University of Technology Research Fund, grant number SUT7-706-47-36-07.

Nomenclature

C_D	drag coefficient
$C_{\varepsilon 1}$	$k-\varepsilon$ turbulent model constant, 1.44
$C_{\varepsilon 2}$	$k-\varepsilon$ turbulent model constant, 1.92
C_μ	$k-\varepsilon$ turbulent model constant, 0.09
$C_{\mu b}$	model constant bubble-induced turbulence, 0.6
c_p	specific constant pressure heat capacity, kJ/kg/K
d	mean diameter, m and microns
E_0	Eotvos number
g	gravity magnitude, m/s^2
g	gravity vector, m/s^2
k	turbulent kinetic energy, m^2/s^2
M	interphase momentum transfer, $kg/m^2/s^2$
P	power, W
Pr	Prandtl number
P_k	shear production of turbulent, $kg/m/s^3$
p'	modified pressure, Pa
Re_p	particle Reynolds number
r	volume fraction
$\mathbf{S}_M$	momentum source, $kg/m^2/s^2$
S	magnitude of momentum source, $kg/m^2/s^2$
t	time, s
U	velocity magnitude, m/s
U	vector of velocity, m/s
V	volume of impeller subdomain, m^3

Greek Letters

ε	turbulence eddy dissipation, m^2/s^3
λ	thermal conductivity, W/m/K
μ	dynamic viscosity, kg/s/m
μ_{eff}	effective viscosity, kg/m/s
μ_t	turbulent viscosity, kg/m/s
μ_{tb}	particle-induced eddy viscosity, kg/m/s

ρ density, kg/m^3
σ surface tension coefficient, kg/s^2
σ_ε $k-\varepsilon$ turbulent model constant, 1.3
σ_k turbulent model constant for the k equation, 1.0

Superscripts

D drag
T matrix transpose
TD turbulent dispersion force

Subscripts

c continuous phase (liquid)
d dispersed phase (vapor)
p particle, droplet, and bubble

References

ANSYS Canada. (2005). *ANSYS CFX-10.0 Manual*, ANSYS Canada, Waterloo, Ont.

Cheremisinoff, N. P. (1986). *Handbook of Heat and Mass Transfer, vol. 2,Mass Transfer and Reactor Design*, Gulf Publishing, Houston.

Deen, N. G., Solberg, T., and Hjertager, B. H. (2002). Flow generated by an aerated Rushton impeller: Two-phase PIV experiments and numerical simulation, *Can. J. Chem. Eng.*, **80**, 1–15.

Eek, R. A., Dijkstra, Sj., and van Rosmalen, G. M. (1995). Dynamics modeling of suspension crystallizers, using experimental process data, *AIChE J.*, **41**(3), 571–584.

Essemiani, K., Traversay, C. D., and Gallot, J. C. (2004). Computational fluid dynamics (CFD) modeling of an industrial crystallizer: Application to the forced-circulation reactor, *Biotechnol. Appl. Biochem.*, **40**, 235–241.

Ishii, M. and Zuber, N. (1979). Drag coefficient and relative velocity in bubbly, droplets or particulate flows, *AIChE J.*, **25**(5), 843–855.

Jakobsen, H. A., Sannaes, B. H., Grevskott, S., and Svendsen, H. F. (1997). Modeling of vertical bubble-driven flows, *Ind. Eng. Chem. Res.*, **36**, 4052–4074.

Kramer, H. J. M., Dijkstra, J. W., Verheijen, P. J. T., and van Rosmalen, G. M. (2000). Modeling of industrial crystallizers for control and design purposes, *Powder Technol.*, **108**, 185–197.

Lapple, C. E. (1951). *Fluid and Particle Mechanics*, University of Delaware, Newark.

Lopez de Bertodano, M. (1991). Turbulent bubbly flow in triangular duct, Ph.D. diss., Rensselaer Polytechnic Institute, Troy, New York.

McCabe, W. L., Smith, J. C., and Harriott, P. (2001). *Unit Operations of Chemical Engineering*, 6th ed., McGraw-Hill, Singapore.

Micale, G. and Montante, G. (1999). On the simulation of two-phase solid-liquid stirred vessels, in *Proceedings of the Fifth CFX International User Conference, Friedrichshafen, Germany*.

Montante, G. and Magelli, F. (2003). CFD simulation of solid-liquid stirred chemical reactors, in *Science and Supercomputing at CINECA, Report 2003*, 343–347, DOI: 10.1388/SSC(2003)-EN-343, CINECA, Bologna, Italy.

Mullin, J. W. (2001). *Crystallzation*, 4th ed., Butterworth-Heinemann, Oxford.

Myerson, A. E. (2002). *Handbook of Industrial Crystallization*, 2nd ed., Butterworth-Heinemann, Boston.

Neumann, A. M. (2001). Characterizing industrial crystallizers of different scale and type, Ph.D. diss., Delft University of Technology, The Netherlands.

Paul, E. L., Atiemo-Obeng, V. A., and Kresta, S. M. (2004). *Handbook of Industrial Mixing: Science and Practice*, John Wiley, Hoboken, N.J.

Pennisi, S. N., Liow, J., and Schneider, P. A. (2003). CFD model development for sugar mill evaporators, in *Proceedings of the Third International Conference on CFD in the Minerals and Process Industries*, Melbourne, Australia, 105–110, CSIRO, Clayton, Vic., Australia.

Pericleous, K. A. and Patel, M. K. (1987). The source-sink approach in the modeling of stirred reactor, *PCH. Physicochem. Hydrodyn.*, **9**, 279–297.

Rein, P. W., Echeverri, L. F., and Acharya, S. (2004). Circulation in vacuum pans, *J. Am. Soc. Sugar Cane Technol.*, **24**, 1–17.

Rielly, C. D. and Marquis, A. J. (2001). A particle's eye view of crystallizer fluid mechanics, *Chem. Eng. Sci.*, **56**, 2475–2493.

Sato, Y. and Sekoguchi, K. (1975). Liquid velocity distribution in two-phase bubble flow, *Int. J. Multiph. Flow*, **2**, 79–95.

Schiller, L. and Naumann, A. (1933). A drag coefficient correlation, *VDI Z.*, **77**, 250–318.

Sha, Z. and Palosaari, S. (2000a). Size dependent classification function in imperfectly mixed suspension continuous crystallizer, in *Mixing and Crystallization: Selected Papers from the International Conference on Mixing and Crystallization Held at Tioman Island, Malaysia in April 1998*, 133–149, Kluwer Academic, Boston.

Sha, Z. and Palosaari, S. (2000b). Mixing and crystallization in suspensions, *Chem. Eng. Sci.*, **55**(10), 1797–1806.

Sha, Z., Oinas, P., Louhi-Kultanen, M., Yang, G., and Palosaari, S. (2001). Application of CFD simulation to suspension crystallization factors affecting size-dependent classification, *Powder Technol.*, **121**, 20–25.

Svenson Technology. (2002). Draft Tube Baffle Crystallizer. http://www.swensontechnology.com/dtbxtaliz.html (accessed 18 March 2008).

Synowiec, P., Bigda, J., and Wójcik, J. (2002). Comparison of the CFD and experimental data of turbulence field in the MSMPR crystallizer, *Chem. Eng. Trans.*, **1**, 1191–1196.

Paul, E. L., Atiemo-Obeng, V. A., and Kresta, S. M. (2004). *Handbook of Industrial Mixing: Science and Practice*, John Wiley, Hoboken, N.J.

Pennisi, S. N., Liow, J., and Schneider, P. A. (2003). CFD model development for sugar mill evaporators, in *Proceedings of the Third International Conference on CFD in the Minerals and Process Industries*, Melbourne, Australia, 105–110, CSIRO, Clayton, Vic., Australia.

Pericleous, K. A. and Patel, M. K. (1987). The source-sink approach in the modeling of stirred reactor, *PCH. Physicochem. Hydrodyn.*, **9**, 279–297.

Rein, P. W., Echeverri, L. F., and Acharya, S. (2004). Circulation in vacuum pans, *J. Am. Soc. Sugar Cane Technol.*, **24**, 1–17.

Rielly, C. D. and Marquis, A. J. (2001). A particle's eye view of crystallizer fluid mechanics, *Chem. Eng. Sci.*, **56**, 2475–2493.

Sato, Y. and Sekoguchi, K. (1975). Liquid velocity distribution in two-phase bubble flow, *Int. J. Multiph. Flow*, **2**, 79–95.

Schiller, L. and Naumann, A. (1933). A drag coefficient correlation, *VDI Z.*, **77**, 250–318.

Sha, Z. and Palosaari, S. (2000a). Size dependent classification function in imperfectly mixed suspension continuous crystallizer, in *Mixing and Crystallization: Selected Papers from the International Conference on Mixing and Crystallization Held at Tioman Island, Malaysia in April 1998*, 133–149, Kluwer Academic, Boston.

Sha, Z. and Palosaari, S. (2000b). Mixing and crystallization in suspensions, *Chem. Eng. Sci.*, **55**(10), 1797–1806.

Sha, Z., Oinas, P., Louhi-Kultanen, M., Yang, G., and Palosaari, S. (2001). Application of CFD simulation to suspension crystallization factors affecting size-dependent classification, *Powder Technol.*, **121**, 20–25.

Svenson Technology. (2002). Draft Tube Baffle Crystallizer. http://www.swensontechnology.com/dtbxtaliz.html (accessed 18 March 2008).

Synowiec, P., Bigda, J., and Wójcik, J. (2002). Comparison of the CFD and experimental data of turbulence field in the MSMPR crystallizer, *Chem. Eng. Trans.*, **1**, 1191–1196.

Conclusions & future work

A generic methodology for template induced crystallization experiments was developed. For this purpose the solubility curve and its metastable zone width for pH-shift crystallization of cinnamic acid were experimentally determined, as well as the induction time as a function of pH. From the results is deduced that a total concentration of cinnamic acid 6.75·mmol·l^{-1} is required for the TIC-experiments. The pH of the crystallizing solution therefore should be in the range of 2.5 to 4.5.

Based on the developed generic methodology, TIC experiments will be conducted to find suitable templates for the crystallization of cinnamic acid. Future work will focus on the development of an integrated process of crystallization and fermentation. For this purpose a suitable driving force has to be created (bulk or locally) and a separation and regeneration tool for templates has to be developed.

References

[1] www.b-basic.nl

[2] Kashchiev, D., van Rosmalen, G.M., Review: Nucleation in solutions revisited. *Crystal Research and Technology* **38** (2003) 555-574

[3] Davey, R., Garside, J. *From molecules to crystallizers*. 1st edition. Oxford university press inc., New York, 2000

[4] Verdoes, D., van der Meer, H., Nienoord, M., D: Filtration Assisted Crystallization Technology: Heterogeneous seeds enable fast crystallization and easy filtration. *'Proceedings ISIC 16' VDI-Berichte* **1901.2** (2005) 787-792

[5] Bisselink, R.J.M., van Erkel, J., Haalbaarheidsonderzoek om door waterelektrolyse kaneelzuur te kristalliseren in fermentoren. *Internal report TNO*, 2005.

[6] Nijkamp, K., van Luijk, N., de Bont, J.A.M., Wery, J. The solvent-tolerant *Pseudomonas putida* S12 as host for the production of cinnamic acid from glucose. *Applied genetics and molecular biotechnology* **69** (2005) 170-177

[7] Yalkowsky, S.H., Dannenfelser, R.M., *Aquasol database of aqueous solubility*. Version 5. College of Pharmacy, Tucson, 1992.

Acknowledgements

This project is financially supported by the Netherlands Ministry of Economic Affairs and the B-Basic partner organizations (www.b-basic.nl) through B-Basic, a public-private NWO-ACTS programme (ACTS = Advanced Chemical Technologies for Sustainability).

Computational Fluid Dynamic Modeling of a 1 m^3 Draft Tube Baffle Crystallizer with Fines Removal

A. E. Flood and W. Wantha
School of Chemical Engineering, Suranaree University of Technology, 111 University Ave., Nakhon Ratchasima 30000, Thailand.
adrianfl@sut.ac.th

The commercial software ANSYS CFX10.0 has been used to model fluid flow, heat transfer and boiling in a 1m^3 Draft Tube Baffle (DTB) crystallizer with fines removal, used for the crystallization of salt. The crystallizer contains several sections with very different flow and heat transfer conditions, including a draft tube, an annular space for down-flow of liquid outside the draft tube, and an annular settling zone separated from the main body by a baffle, which is used for fines removal. The feed, and the flow of the dissolved fines, are fed directly under an upflow impeller located at the base of the draft tube. A variety of parameters in the crystallization process were varied in the course of the study, including the power input to the impeller, the total rate of heat transfer in the crystallizer, and flow rates of the feed stream, and fines removal stream. The results demonstrate the relationship between the operating conditions and the flow regimes in different sections of the crystallizer, and also the boiling behavior, vapor flow, and phase separation at the free surface of the crystallizer. Of special importance to the operation of the crystallizer is the predicted effect of the fines removal rate on the fines cut-size, which could have a significant impact on the overall product particle size distribution.

1. Introduction

Fluid and particle flows in industrial crystallizers are critical in determining key parameters for the crystallization process, including the temperature and concentration (and therefore supersaturation) distributions in the vessel, crystal growth, nucleation, attrition, and breakage rates, and settling rates in fines removal sections of the crystallizer, in addition to other variables. It is important to understand that, contrary to common models used such as the MSMPR model, these variables are not constant over the volume of the crystallizer, but vary due to limitations in heat and mass transfer rates, and variations in the fluid dynamics in different regions of the crystallizer. One method to model crystallizers which is able to deal with such variations is the compartmental approach [1]. This approach breaks the body of the crystallizer into several 'compartments', with each compartment having more or less uniform levels of the major variables over its entire volume: the compartments may then be connected by input/output streams in order to be able to model the full crystallizer. The alternative approach is to fully solve the population balance, including determination of crystal nucleation rate, growth rate, attrition and breakage rate, as a function of temperature, supersaturation, suspension density, and fluid shear, for each element in a computation fluid dynamic mesh of the crystallizer, in addition to solving the usual CFD equations for motion and heat transfer. This approach is obviously extremely computationally intensive, since most CFD meshes have of the order of 10^5 or 10^6 nodes defined in the geometry.

In order to be able to generate a compartmental model of an industrial crystallizer it is suitable to initially perform a basic CFD study of the crystallizer to determine the optimum number

and geometry for the compartments, the average conditions (temperature, supersaturation, fluid velocities, shear, etc.) in each compartment, and also the potential deviation from the average conditions in each compartment. The current research performs basic non-isothermal CFD analysis of the fluid (liquid and vapor) flows in a 1 m^3 draft tube baffle (DTB) crystallizer with fines removal, similar to an existing crystallizer at Delft University of Technology [2], for which a clear geometry has been published [3].

2. Methods

The CFD simulation of the DTB crystallizer with fines removal was performed with the commercial CFD software ANSYS CFX 10.0. In this preliminary study, only the fluid (vapor and liquid) flows were analyzed: if suspension densities in the crystallizer are relatively low then particle flows can be determined using a Langrangian model superimposed on the fluid flows; at high suspension densities it will be necessary to re-simulate the crystallizer including momentum transfer terms between the solid and fluid phases.

The multiphase flow in the crystallizer was modeled with the "inter-fluid transfer" or in-homogenous model, which is suitable for dispersion of vapor bubbles in a liquid (i.e. vapor is the disperse phase, and liquid is the continuous phase). In this model separate velocity fields and other relevant fields exist for each fluid. The pressure field is shared by all fluids. The fluids interact via an interphase transfer term. To reduce the complexity of the two phase model at the top of the liquid mass in the crystallizer, a degassing condition was assumed at this surface. For this boundary condition the dispersed phase is allowed to exit through the surface, while the surface is treated as a free-slip wall for the continuous phase. Interphase heat transfer is modeled with an inhomogeneous interphase transfer model using the two resistance model, and also the thermal phase change model. The Hughmark correlation is used for the heat transfer coefficient of the liquid phase, while it was assumed the vapor phase side had zero resistance. Interphase mass transfer was calculated from the energy balance.

Turbulence in the liquid phase was modeled using the k-ε model, and the dispersed phase zero equation model was employed for the vapor phase. To reduce the complexity and computation time required for the simulation it was decided to model the impeller via a momentum source term, rather than attempting a full description of the flow around a full model of an impeller. This assumption has previously been shown to be suitable for mixing vessels [4]. We have limited the momentum source to an axial addition only: baffles perpendicular to the crystallizer wall should reasonably effectively remove radial components of the momentum produced in the impeller. It is assumed that approximately 50% of the power of the impeller is transfer into axially directed momentum addition. The internal heat exchanger is modeled as a heat source in the draft tube of the crystallizer.

Full details of the models used in CFX 10.0 are available in the manual for the program [5], and general models required for CFD, not discussed here, can also be found.

3. Crystallizer Geometry and Physical Definitions

The crystallizer used for numerical simulation in this work is a pilot scale 1050 l DTB crystallizer. The crystallizer dimensions, 3D geometry, and meshing are shown in Figures 1 and 2, respectively.

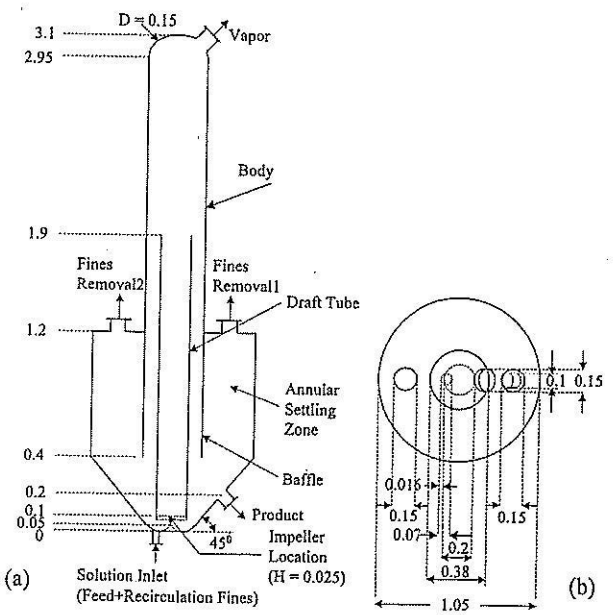

Figure 1. DTB crystallizer geometry and dimensions. Dimensions are given in meters: (a) side view; (b) top view.

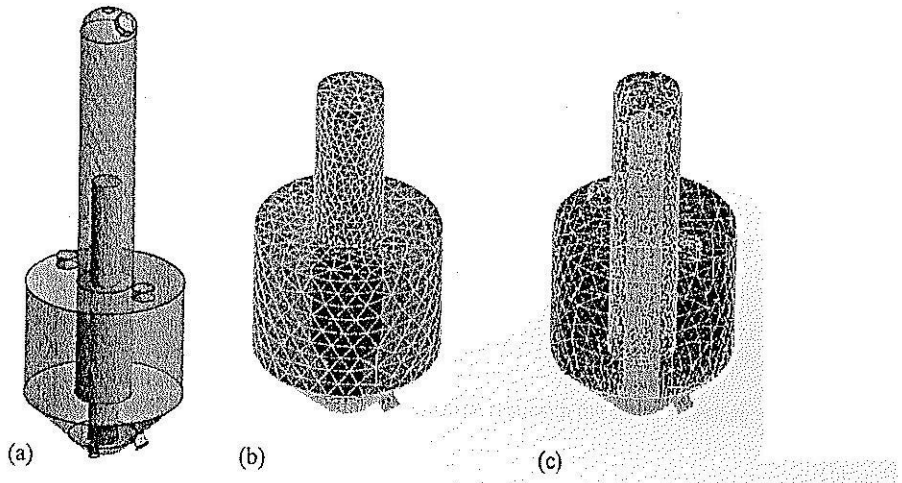

Figure 2. 3D geometry and mesh of the evaporative-DTB crystallizer. (a) crystallizer geometry; (b) mesh before mesh adaptation; (c) mesh after mesh adaptation.

After mesh adaptation during the simulations, used in order to optimize mesh densities in terms of variations in variable values throughout the crystallizer, most runs had in the order of 8×10^4 nodes and 4×10^5 elements. Runs were conducted at a variety of mesh sizes to ensure that the results were mesh size independent.

Fluid properties for the two phases modeled are shown in Table 1.

Table 1. Physical properties of vapor and liquid.

Physical properties (units)	Phase	
	Liquid	Vapor
Density ($kg \cdot m^{-3}$)	1198.00	0.59
Viscosity ($kg \cdot s^{-1} \cdot m^{-1}$)	0.00152	0.0000124
Thermal conductivity ($W \cdot m^{-1} \cdot K^{-1}$)	0.57	0.025
Boiling temperature (K)	380.60	-
Specific heat capacity ($J \cdot kg^{-1} \cdot K^{-1}$)	3336.85	2080.10
Surface tension ($N \cdot m^{-1}$)	0.077	-

4. Results and Discussion

The main variable investigated in the current study is the effect of the heat source strength on the behavior of the crystallizer. Previous studies on an isothermal model of the crystallizer (with an external heat exchanger assumed, which feeds a two-phase mixture at the saturation temperature into the crystallizer) have already investigated the effect of feed flow rate, product flow rate, fines removal flow rate, and power input via the impeller on the performance characteristics and flow fields of the crystallizer [6].

A significant difference between the two studies (apart from the non-isothermal model containing an internal heat exchanger) is that the liquid surface in the isothermal simulation was modeled using a free surface model, but a degassing condition was used in the non-isothermal simulation to aid convergence of the solution. The fluid flow fields in the two models are expected to be slightly different because the vapor is fed to the crystallizer from an external heat exchanger in the isothermal model, but produced by boiling (mostly near the free surface) in the non-isothermal model, however it was expected that the overall liquid flow vectors would not be significantly altered by this change, and this is shown to be true in Figure 3. This indicates that some key conclusions made from the isothermal study will still be valid for the non-isothermal case, particularly the effect of parameters on the velocity in the settling zone, and therefore the predicted fines cut-size [6]: this is because there is very little difference in the flow fields in the settling zone in the two cases. In the non-isothermal simulation the flow field is more uniform near the base of the draft tube, with less influence of the fluid flowing into the crystallizer body under the left hand side of the impeller.

The main result of the non-isothermal simulation is the effect of the heat source on the evaporation rate, which can be used to predict crystallization rates. Other flow field parameters, particular the flow near the free surface where boiling occurs, are also strongly affected by the heat addition rate. In this study, four test cases are performed, using a constant momentum source addition of 10,000 $kg/m^2/s^2$, feed solution flows of 1.18608 kg/s and product suspension flows of 0.1797 kg/s, with the heat source values varying at 11,000,

12,000, 13,000, and 13,500 kW/m^3. Note that the heat source is the heat input per unit volume (with the volume of the sub-domain equal to 0.0007854 m^3) so that the heat input values of these heat source values are 8.64, 9.42, 10.21, and 10.60 kW, respectively.

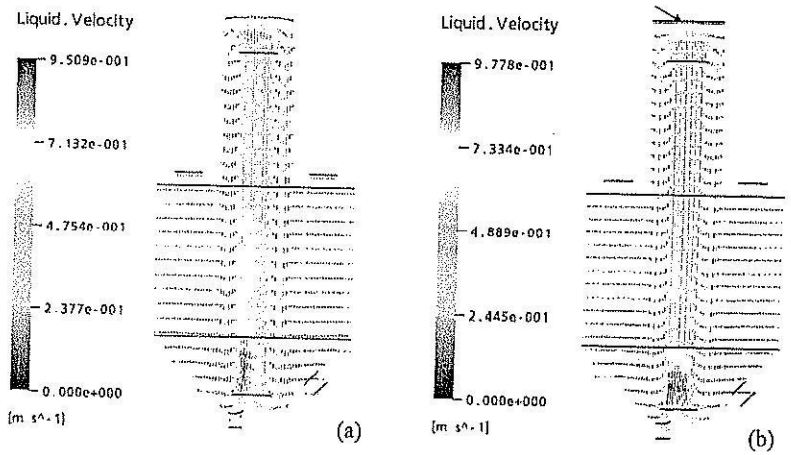

Figure 3. Liquid flow fields in the crystallizer for (a) the isothermal simulation with an external heat exchanger; (b) the non-isothermal simulation with an internal heat exchanger.

The CFD results showed that the vapor formed linearly increases with increasing heat input (Figure 4). This can be shown to be true by the overall energy balance around the crystallizer (neglecting the small heat of crystallization):

$$\dot{m}_F H_F + \dot{Q}_{to} + \dot{W}_{to} = \dot{m}_{Fines} H_{Fines} + \dot{m}_p H_p + \dot{m}_v H^{sat.vap.} \tag{1}$$

In this work, the temperature of the feed solution is 379 K, which is near the boiling point of the solution (380.6 K) and the heat added to the system is used to evaporate a relatively small fraction of the solution to induce crystallization, so that the temperature of the solution at the fines removal outlet and product crystals outlet are constant at the saturation temperature. This enables the energy balance to be simplified to

$$\dot{m}_v = \frac{\dot{W}_{to} + \dot{m}_F\left(H_F - H^{sat.sol.}\right)}{L} + \frac{\dot{Q}_{to}}{L} \tag{2}$$

Substitution of the relevant constants in this equation results in the linear response

$$\dot{m}_v = 0.00045\dot{Q}_{to} - 0.0035 \tag{3}$$

This equation is compared to the vapor production in the crystallizer in Figure 4.

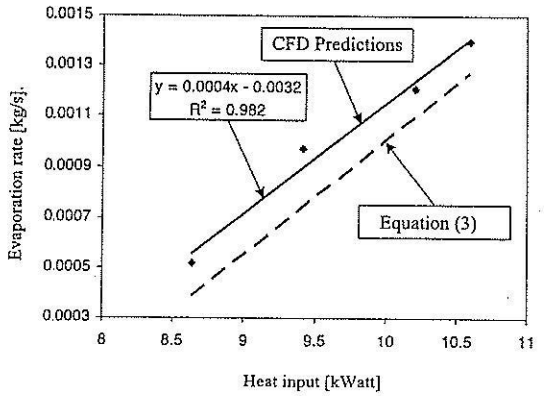

Figure 4. Evaporation rate in the crystallizer as a function of the heat input for both the non-isothermal simulation and the simplified energy balance around the crystallizer.

There are only small temperature gradients noticeable in the solution to the non-isothermal simulation, with the largest gradient being near the feed inlet, as the feed is slightly subcooled. This low temperature fluid is noticeable underneath the left hand side of the draft tube, at the feed inlet, and continues a short distance past the impeller: the fluid being drawn into the right hand side of the impeller is fluid being recirculated from the body of the crystallizer, which is very close to the saturation temperature. Temperature gradients in a real crystallizer might be more than shown here due to heat losses from the body of the crystallizer, which has not been modeled in the current simulations.

Another interesting aspect of the simulation results is the analysis of the vapor volume fraction, as shown in Figure 5. The results show that boiling occurs near the free surface, and also at the top edge of the draft tube: this must be due largely to the pressure variations in the crystallizer since the temperature variation is quite low. The static pressure is the main component of the pressure variation in the crystallizer, and of course this is a minimum near the free surface.

The flow near the free surface of the crystallizer is quite complex, and liquid and vapor have very different flow fields in the area between the top of the draft tube and the free surface. This is illustrated in Figure 6. A significant amount of the vapor is produced near the top edge of the draft tube, and this vapor is carried out towards to wall of the crystallizer and then up to the free surface where it exits due to the degassing condition. The liquid, on the other hand, has a strong recirculation loop, where much of the liquid exiting the draft tube falls over the edge of the draft tube into the annular space, while a smaller portion of the liquid is forced into the region above the draft tube into a recirculation loop.

5. Conclusions

A 1 m^3 DTB crystallizer with fines removal has been modeled with both isothermal and non-isothermal simulations. The simulations have yielded information on liquid and vapor flow fields in the crystallizer, and the effect of several variables on the operating performance.

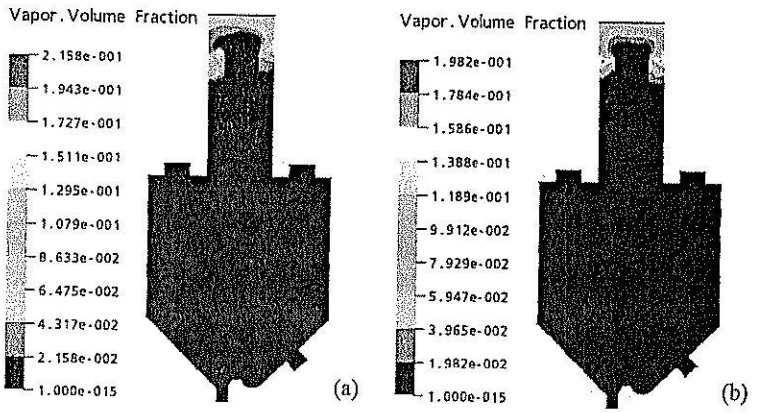

Figure 5. Profiles of the vapor volume fraction in the non-isothermal simulation for heat source additions of (a) 13,000 kW/m^3; (b) 13,500 kW/m^3.

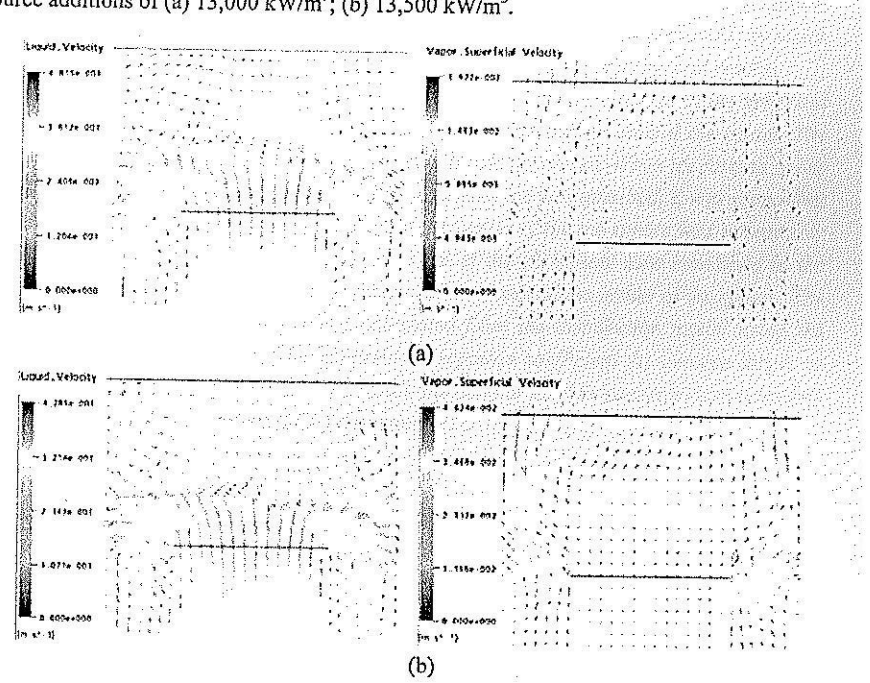

Figure 6. Liquid and vapor velocity vectors at the top of draft tube for heat source additions of (a) 11,000 kW/m^3; (b) 12,000 kW/m^3.

The results could be used to suggest suitable regions for compartments for a compartmental model of the crystallizer, as well as crystallization parameters for each compartment in the model based on the temperature, flow field, and vapor fraction in each compartment. Alternatively the simulation model could be extended to include the crystal phase, including terms for crystal growth and nucleation as functions of the fluid properties.

6. Nomenclature

H	Specific enthalpy (kJ/kg)
L	Latent heat (kJ/kg)
$\dot{m}$	Mass flow (kg/s)
$\dot{Q}_{in}$	Heat input (kW)
$\dot{W}_{in}$	Work addition through an impeller (kW)

Subscripts/Superscripts

F	Feed
Fines	Fines removal
p	Product suspension
Sat. Sol.	Saturated solution
Sat. Vap.	Saturated vapor
v	Vapor removal

7. References

[1] Kramer, H.J.M., Dijkstra, J.W., Neumann, A.M., Ó Meadhra, R., and van Rosmalen, G.M. Modelling of industrial crystallizers, a compartmental approach using a dynamic flow-sheeting tool. *J. Cryst. Growth* **166**(1-4) (1996) 1084-1088.

[2] Neumann, A.M. *Characterizing Industrial Crystallizers of Different Scale and Type*. Ph.D. thesis, Delft University of Technology, The Netherlands, 2001.

[3] Grootscholten, P.A.M. and Jancic, S.J. Industrial Crystallization, from *Handbook of heat and mass transfer operations*, N. P. Cheremissinoff (ed.). Gulf Publ., Houston, USA, 1985.

[4] Pericleous, K.A. and Patel, M.K. The Source-Sink Approach in the Modelling of Stirred Reactors. *PCH* **9**(1/2) (1987) 279-297.

[5] *ANSYS CFX 10.0 User's Manual*. ANSYS Inc., Canonsburg, USA, 2005.

[6] Wantha, W. and Flood, A.E. *Numerical Simulation and Analysis of Flow in a DTB Crystallizer*. Proc. Int. Conference on Modeling in Chemical and Biological Engineering Sciences, Bangkok, Thailand, 2006.

Acknowledgements

The authors thank the SUT Research Fund for funding of the research presented here. Wirapong Wantha was also supported by a Graduate Student scholarship from Suranaree University of Technology.

Freeze Separation of Phosphate from the Aqueous Solutions by the Formation of Spherical Ice

T. Yamaguchi, Y. Taguchi*, N. Sakamoto*
Research & Development Division, Asahi Carbon Co., Ltd.,
2 Kamomejima-machi, Niigata 950-0883, JAPAN
*Department of Chemistry and Chemical Engineering, Niigata University,
8050, Ikarashi 2-nocho, Niigata 950-2181, JAPAN
t.yamaguchi@asahicarbon.co.jp

In this research, after forming spherically shaped ice from an aqueous solution containing potassium dihydrogen phosphate as an inorganic salt and then observing the temperature and concentrations of phosphate in the ice, the relation between the freezing rate of the ice and the concentration ratio was examined. To examine the concentration ratio in relation to the freezing rate of the ice, the equilibrium segregation coefficient was presumed, by which a distribution model of solute in ice was constructed based on the experimental results.
Our results indicated that the phosphate ions were not uniformly included in the spherical ice, with concentrations being lower near the surface and higher around the center. The peak value at the center increased as the ice growth rate decreased. When ice formed under the undercooling temperature of $\Delta T = 1.0$℃ and seed ice was attached, it was found that the concentration ratio of phosphate ions near the center of the ice sphere was remarkably higher, i.e., approximately 68% (at $V_I/V_0 = 0.06$) of the phosphate ions contained in the initial solution were excluded into the unfrozen solution around the center of the sphere. The equilibrium segregation coefficient (k^*) calculated from the distribution model using the experimental results was 0.03. The apparent segregation coefficient (k) became larger as the growth rate of the ice increased; as a result, the ratio of the film concentration boundary layer to the diffusion coefficient (δ/D_L) decreased.

1. Introduction

Many studies of the processes of dephosphorization and denitrogenation from wastewater have been carried out. However, many of these processes have disadvantages such as the generation of sludge, low recovery, high cost, etc. These disadvantages may be largely overcome by a freeze-separation method. During ice formation, the ice crystals naturally exclude impurities into the unfrozen solution. [1], [2]
The freeze-separation method has the following advantages: 1) it is not necessary to add any reagents to the solution, and the operation is simple; 2) the method does not produce any toxic gas because it is not accompanied by combustion or a chemical reaction; 3) it is an energy-saving system because the solidification energy needed for freezing is